

Objective indicators and multivariate data analysis for the characterization of cavitation effects

Christian Koch* / Physikalisch-Technische
Bundesanstalt

Matthias Jüschke / Physikalisch-Technische
Bundesanstalt

*corresponding author: christian.koch@ptb.de

ABSTRACT

For the design and optimization of technical ultrasound applications, empirical methods are applied which rely on experience rather than quantitative measurements or models. This complicates the objective description of important output quantities such as, e. g., the cleaning quality or the sonochemical yield as well as quality management in manufacturing processes.

This paper presents different techniques for obtaining quantitative cavitation indicators based on practical methods and it shows the relations between these indicators. Hydrophone measurements are used to describe the sound field as the driving force of cavitation. The erosive effect of cavitation is investigated by an aluminium foil technique, including a newly developed image processing technique which can distinguish between holes, burrs, and dents in the foil which are combined to a single quantitative erosion parameter. For the description of sonochemical effects, the reduction of iodine is used as a model reaction and finally, sonoluminescence is detected. All quantities are measured with high spatial resolution.

Measurements of all these indicators in ultrasonic cleaners are presented that show that different properties and effects of cavitation can be described. The relations between the parameters are investigated by means of a factor analysis. The loadings of three factors were calculated and the indicators, experimental parameters, and finally the data were depicted in factor space. The factors show relations between the variables and several overlapping indicators and parameters were found. The coordinates of data (data scores) indicate tendencies within the data and the assessment to the factors allows finding of hidden relations.

1. INTRODUCTION

Cavitation is applied in many technical and medical fields where fluids are used for processing, cleaning, or as an imaging medium. A quantitative description of the processes is often required for optimization purposes or, in particular, for quality management. If, for example, a cleaning process step is included in a line production, the quality management system requires a specific description of all important process details for a

potential replacement of the device in the case of malfunctioning. Since many parameters influence cavitation the outcome of such a cavitation-based process varies strongly with the application conditions and often has a random behaviour. Thus, no widely accepted process description methods or even standards have been established hindering the comparability and the reliability of manufacturing.

A possible strategy to find a general methodology for the description of cavitation effects is the determination of experimental indicators or numbers from cavitation induced effects. A variety of methods has been presented for example the generation of holes and dents in an aluminium foil [1 - 3] or the erosion of an Al_2O_3 layer from an aluminium slab for an electrical detection [4]. These techniques rely on the mechanical impact of cavitation but also the chemical effects have been detected by electro-chemical probes [5] or model reactions [6]. Another alternative is to measure the sound field and to calculate particular spectral numbers as the subharmonic or the noise power [7 - 9]. Many of these indicators arise, however, from very specific determination methods and the relation to practical cavitation effects and outcomes is often not yet clear or proven.

It seems that there is no single indicator that could describe a wider spectrum of cavitation applications. In this paper a set of four model processes is applied to an ultrasonic vessel which covers a wider range of cavitation effects. Sound field measurement, an erosion indicator, a chemical indicator and sonochemical luminescence, which are all determined at confined local positions, are combined to form a set of indicators for describing the cavitation field in the cleaning vessel. All these indicators and the experimental parameters (temperature, electrical input power and oxygen content) are set in relation to each other, and correlations, dependences and overlapping are investigated. This is realized in particular with a structure-finding statistical method as part of a multivariate data analysis. A factor analysis is applied which is first used to find relations and overlapping between all variables by finding common factors. In a second step, a method is developed for a general strategy of a description of cavitation processes by a reduced set of measurands.

2. DETERMINATION OF SPATIALLY RESOLVED CAVITATION INDICATORS

2.1 Measurement set-up

All measurements were carried out in a commercially available ultrasonic cleaning vessel (TI-H-5, Elma GmbH, Germany) of 4 L volume. The working frequency was $f_w = 45$ kHz and the transducers were driven by an external amplifier. The excitation signal was a non-modulated sine-wave generated by a synthesizer and fed into the amplifier. The voltage at the transducers was measured via a resistor network and the excitation current into the transducers was detected by a current probe (P6021, Tektronix Inc., USA). The temperature of the de-ionized water in the vessel could be controlled with an accuracy of 1 °C by means of a flow system. The O₂-content was set by starting the measurements with degassed water and waiting a particular time for approaching the next O₂-content value by naturally returning of air into the water. 7 measurement points (see Fig. 1) were chosen in the vessel to obtain results at very active and more passive regions in the vessel.

For clarity of terms, a parameter defines a measurand which is set by the experimenter during the measurement, for example the temperature or the synthesizer voltage. An indicator means a value or number measured or determined during the experiment. Note, that both are used as variables in the factor analysis.

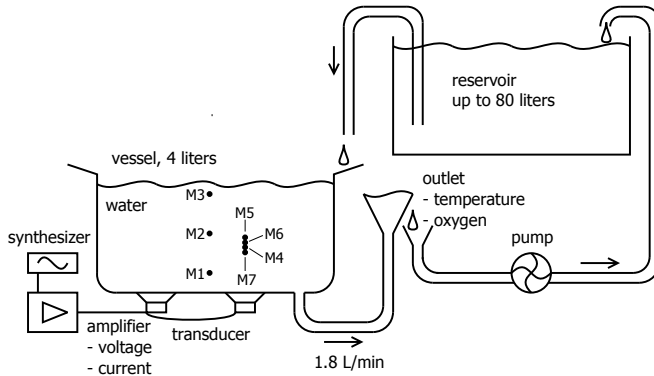


Fig. 1: Experimental set-up with electrical excitation, circular flow of the water and seven measurement positions M1-M7 in the vessel.

2.2 Measurement of sound field data

The sound field was measured using a hydrophone (TC 4013, Reson, Denmark) which was positioned by a three-axis positioning system controlled by computer. From the time-dependent data the spectrum was calculated and several indicators were derived: the amplitudes of the fundamental at f_w , the subharmonic at $f_w/2$, the ultraharmonic at $3f_w/2$, the second harmonic at $2f_w$, and a noise value integrating the noise spectral density in a frequency range from 100 kHz to 200 kHz. In addition, the rms-value of sound pressure was determined from the time-dependent data.

2.3 Determination of erosion indicator

For quantitative determination of erosion an aluminium foil technique was used [3]. A 15 µm thick foil (aluminum alloy 1200, Korff AG, Switzerland) was mounted in a frame and brought in the running cleaner for 20 s. The loaded foil was

imaged using a flatbed scanner and purpose made software detected the dents, the burrs, and the holes in the foil [3]. Counting all cavitation events in a detection area with the size of the hydrophone dimensions and weighting the dents, burrs and holes yields the erosion indicator.

2.4 Determination of sonochemical indicator

The chemical effect of cavitation was concerned with the simple model reaction of oxidation of iodine ions. The test solution was poured into a thin-walled plastic test tube which was brought to the different measurement points in the bath. The local concentration of the test fluid in the tube allowed a spatially resolved measurement. After ultrasound exposure the fluid was analyzed using a ultra-violet transmission spectrometer (SpectroFlex 6600, WTW GmbH, Germany) and the amount of produced I₃⁻ ions was detected. The change in extinction was used as indicator. For comparison with excitation parameters, it was not normalized to the electrical power of the transducers.

2.5 Measurement of sonoluminescence

Sonoluminescence was detected using a luminol solution brought into the vessel. The solution was also poured into a plastic thin-walled test tube for a spatially resolved measurement. The emitted light from the nearly transparent test tube was detected by an EMCCD-camera (iXon 885, Andor Technology, Northern Ireland) and the background luminescence from the surrounding was compensated. The light intensity was averaged over the volume of the test tube. The shutter time was chosen in a way assuring the dynamic range of the detector being used in the full range.

2.6 Course of measurement cycles

Measurements were carried out with different parameter settings to cover a wide range of application conditions. The parameters set during the experiments (temperature T , driving voltage U , O₂-content c_{O_2}) were varied within a certain range (10 °C – 35 °C, 1.75 V – 2.75 V, 2.5 mg/l – 7 mg/l). The measurements were made within subsequent sub-cycles by increasing the temperature step by step from the starting value 10 °C at fixed O₂-content or rising the O₂-content from 2.5 mg/l at a fixed temperature. For practical reasons the T and c_{O_2} setting courses were not mixed. It was also not possible to measure all indicators at the same time because exchanging the sensors needed a while in which the O₂-content significantly changed. Therefore, different measurement courses had to be combined and as criteria for finding similar measurements minimal deviations of parameters were used.

3. MEASUREMENT RESULTS

In a first step, the spectral components of the sound field were measured to get an overview of the behavior of the cavitation in the vessel since sound field parameters can easily be determined in an ultrasonic cleaner.

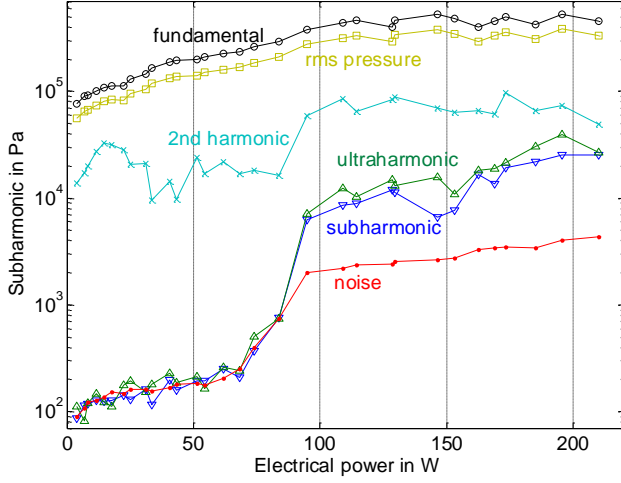


Fig. 1: Sound field components as a function of electrical input power measured at position M4.

Fig. 1 shows the dependence of the spectral sound field components on the electrical input power P_{el} , the parameter which is most important to control the cavitation effect. The measurements are obtained at position M4 (see Fig. 1).

The fundamental and the rms pressure increase monotonically with increasing electrical input power. For nearly all measurement points and amplitudes, about 80% of the signal power is concentrated in the fundamental. So, taking the factor of $\sqrt{2}$ between the amplitude of a sine wave and its rms value into account, the fundamental and the rms pressure differ only by a power-independent factor of 1.2 to 1.4 showing the power concentration in the fundamental.

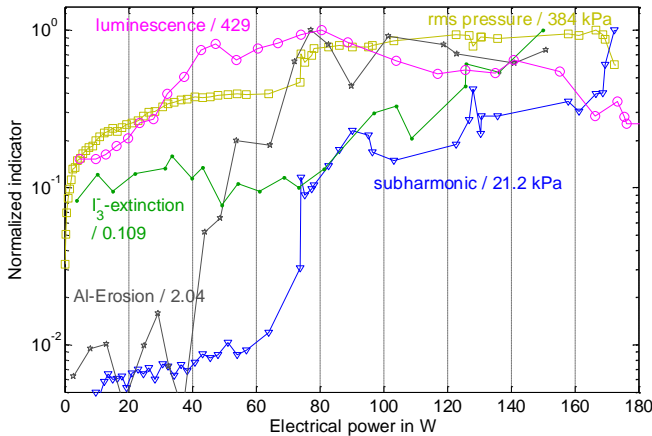


Fig. 3: Normalized cavitation indicators depicted versus the electrical input power of the transducers at M4. The normalizing factors are given in the trace captions.

The other indicators show a threshold behavior at about $P_{el} = 90$ W. The amplitudes of the subharmonic and the ultraharmonic show quite similar power dependence and the

second harmonic has also a threshold but much less pronounced. The threshold behaviour is a typical cavitation indicating property.

As demonstrated for the sound field indicators as a function of P_{el} , threshold behavior also occurred for the other indicators introduced in section 2. Fig. 3 shows selected indicators in dependence on the electrical power and normalized to their maximum values. The normalizing factors are given in the legend. The temperature was set to 21 °C and the O_2 concentration was kept at 100%. All indicators were measured at position M4.

The electrical power values where the indicators exceed a threshold level differ. The luminescence has the lowest threshold at about 30 W. At an input power of about 80 W the luminescence, however, starts decreasing which is in agreement with other studies [10, 11]. Saturation of sound field pressure could be the reason for this effect. The threshold for the aluminum foil erosion indicator amounts to 45 W. The subharmonic and the fundamental have a threshold at 75 W and the triiodide extinction threshold is 90 W. The different thresholds for luminescence and extinction are remarkable, since the activating chemical reaction has a similar starting point, which is the generation of hydroxide radicals.

4. MULTIVARIATE ANALYSIS

4.1 Method

Multivariate data analysis is a powerful tool to investigate large data sets. It includes structure finding methods for data where no relations can be assumed a priori and structure proving methods when a hypothesis is already known. Since the cavitation data obtained from the experiments do not imply a structure a priori, a factor analysis was applied for analyzing and arranging the data. For numerical implementation the routine of the statistical toolbox of Matlab[®] was used.

For a factor analysis the input data, i.e. all parameters and indicators, have to be arranged as variables. The data matrix $\mathbf{X} = x_{i,k}$ contains V variables in V columns ($1 \leq k \leq V$) of length N which is the number of measurements ($1 \leq i \leq N$). In the case of cavitation data, for example, in the first column the driving voltages of every measurement were set, in the second the temperature values and so on. For all calculations the data were normalized within each column by

$$\mathbf{Z} = z_{i,k} = \frac{x_{i,k} - \bar{x}_k}{\sigma_k(x_{i,k})} \quad (1)$$

where $\sigma_k(x_{i,k})$ denotes the standard deviation and \bar{x}_k the average of the k -th column. The analysis tries to find overlapping of variables and calculates F common factors that represent joint properties of the variables. The number of factors F has to be chosen in advance (see below). Often a common factor indicates a causal relation between variables giving deeper insight in the basics of the process. The factors span a new coordinate system (factor space) and both, the variables and the data can be depicted in this new system. The coordinates of the variables in the factor space are called loadings in a matrix $\mathbf{A} = a_{k,j}$ where

$1 \leq j \leq F$ and the coordinates of the experimental (original) data are the scores $\mathbf{P} = p_{ij}$. The scores were calculated from the fundamental lemma of factor analysis

$$\mathbf{Z} = \mathbf{P}\mathbf{A}' \quad (2)$$

where the dash means the transpose of the matrix.

For each variable $z_{i,k}$ a specific variance is calculated which describes the component due to independent random variability. A small specific variance indicates that most of the behavior of the variable is explained by the common factors. The variances depend on the number of factors which can be chosen at the beginning of modeling. There are no clear rules for setting the number of factors. Summing up all specific variances yields a measure to assess the percentage of the total variability not explained by all factors; the number of factors was chosen in such a way, that the explained part was at least 90%. In nearly all calculations this was achieved by a number of three factors.

The results of the calculation can beneficially be visualized in an F -dimensional plot of factor space for a better overview. The variables were depicted as lines and the data as points. Variables which are close together have a high similarity because they were described by the same factor combination and a causal relation can be assumed.

All data points, i. e. measurement results can also be visualized in the factor space. They can be assigned to the factors and for example changes of parameters can be observed by moving the data points in the factor space. This technique can be used to find general tendencies.

4.2 Application of factor analysis to cavitation data

A factor analysis was applied to experimental data from the measurement cycles. Fig. 4 shows an example of the factor space plot for a measurement of cycle at one point M4 with varying temperature in gas-saturated water. Depicted are the data as points and all variables as vectors which lengths correspond to the specific variances given in the figure caption. The O_2 -content and the temperature are close to factor 2 but in opposite direction which means that they have opposite influence on the data set. This conclusion is highly relevant because the specific variances of both variables are small. Sonoluminescence is close to the chemical indicator as it could be expected, also the subharmonic and the electrical power can be found in this range. The fundamental has a difference to the measured electrical power which was found in many data sets.

Not only the variables can be analyzed in the factor space plot. In Fig. 4 the data structure was of such a kind that with increasing measurement number the temperature was increased subsequently and the measurement was carried out at low, medium and high power in gas-saturated water. These cycles can be identified by three clusters at different positions. The low-power values lie in the lower half space, the medium power values in the centre and the high-power values in the upper half space. They "move" in direction of factor three which is mainly represented by the fundamental. Within the cluster the arrow shows in the direction of increasing temperature. It points mainly along the axis of factor 2 which is indeed represented by the temperature. This can lead to the conclusion that high-power

and high-temperature systems are mainly determined by temperature and fundamental pressure.

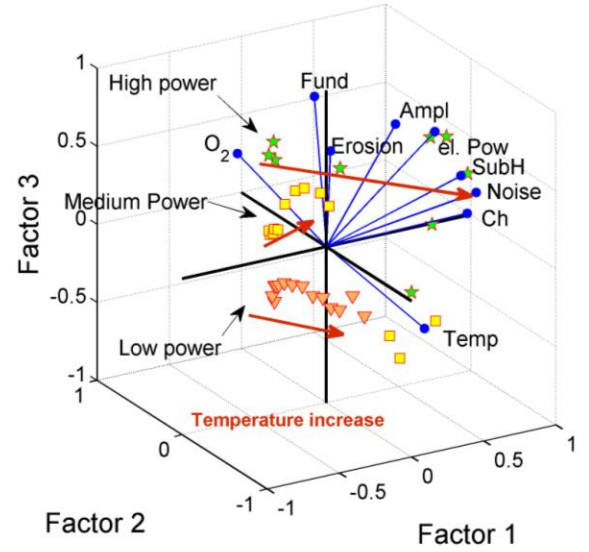


Fig. 4: Factor analysis at measurement point M4 with varying T , solid points at the end of lines: variables, squares: data points, Triangles: low power, squares: medium power, stars: high power; Variables (with specific variances in brackets): Ampl: driving voltage (0.293), el. Pow: electrical power (0.063), Temp: temperature (0.032), O_2 : O_2 -content (0.005), Fund: fundamental (0.19), SubH: subharmonic (0.076), Noise: noise power (0.005), Ch: chemical indicator (0.186), Erosion: erosion indicator (0.676).

4.3 Description of processes

For a quantitative description, the cavitation outcome or its indicators are to be expressed by measurands or parameters obtained from an investigating analysis. The most obvious approach is to use a fitting procedure of experimental data but it is not known in advance which indicator or parameter is best suited for a description of another one. Factor analysis can help to identify useful describing measurands and parameters and to reduce the number of necessary measurements because only matching variables need to be determined.

An indicator can successfully be described by another one if they have similar causality or a close internal relation. Since factor analysis searches for common structures, variables, i. e. indicators or parameters with high similarity (small angle between the vectors in the factor space) have a high potential for mutual expression. Fig. 5 shows an example for the measurement which factor analysis given in Fig. 4. Two variables, the subharmonic and the erosion indicator were depicted in dependence on the noise power which is an easily achievable parameter. To assess the quality of the description, a polynomial fit of order 1, 2, or 3 was applied where the software took the best one by optimizing the r^2 -parameter, which is calculated from the sum of the squares of the distances of the points from the best-fit curve. In the case of similar variables the subharmonic can be fitted with $r^2 = 0.94$ but the more distant

erosion only very poorly with $r^2 = 0.09$ as immediately expected from the factor analysis.

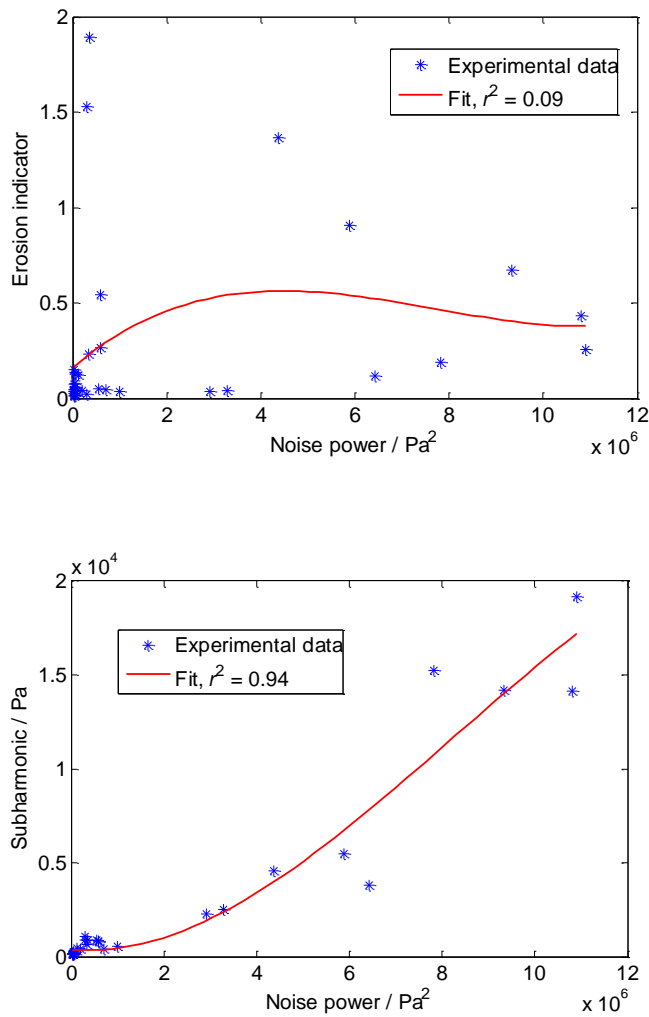


Fig. 5: Dependence of two typical indicators from the noise power for the analysis of Fig. 4.

5. CONCLUSIONS

In this paper, four measurement methods were presented to determine indicators of cavitation for the description of applications. The sensing methods were chosen to serve as model processes which represent different aspects of cavitation effects. It could be shown that important process properties and conditions can be identified. For this purpose, the properties of the indicators and their relations to each other and to the measurement parameters such as the dependence on the electrical input power, the temperature and the O_2 concentration of the water were investigated.

The relations between the parameters were investigated by means of a factor analysis. The loadings of three factors were calculated and the indicators, experimental parameters, and

finally the data were depicted in factor space. The common factors showed relations between the variables and several overlapping indicators and parameters were found. The coordinates of data (data scores) indicated tendencies within the data and the assessment to the factors allowed finding of hidden relations. By the factor analysis representing indicators or parameters specific to the application case were identified which can be used for a complete description of the process. This characterization method can favourably be applied, for example, in quality management systems in industry.

6. ACKNOWLEDGMENTS

This work was supported by the DECHEMA as a member of the AiF in the program “Industrielle Gemeinschaftsforschung” (IGF).

7. REFERENCES

[1]	B.N. Poddubnyi, “Improvement of erosion-test methods based on aluminium foil damage and on sample weight loss”, <i>Sov. Phys. Acoust.</i> 22, 1976, 325-327
[2]	P. Diodati, F. Marchesoni, “Time-evolving statistics of cavitation damage on metallic surfaces”, <i>Ultras. Sonochem.</i> 9, 2002, 325-329
[3]	K.-V. Jenderka, Ch. Koch, “Investigation of spatial distribution of sound field parameters in ultrasound cleaning baths under the influence of cavitation”, <i>Ultrasonics</i> 44, 2006, e401-e406
[4]	P.R. Birkin, D.G. Offin, T. G. Leighton, “The study of surface processes under electrochemical control in the presence of inertial cavitation”, <i>Wear</i> 258, 2005 623-628
[5]	E. Maisonhaute, P.C. White, R.G. Compton, “Surface acoustic cavitation understood via nanosecond electrochemistry”, <i>J. Phys. Chem. B</i> 105, 2001, 12087-12091
[6]	S. Koda, T. Kimura, T. Kondo, H. Mitome, “A standard method to calibrate sonochemical efficiency of an individual reaction system”, <i>Ultras. Sonochem.</i> 10, 2003, 149-156
[7]	M. Hodnett, B. Zeqiri, “Toward a reference ultrasonic cavitation vessel: Part 2 – investigating the spatial variation and acoustic pressure threshold of inertial cavitation in a 25 kHz ultrasound field”, <i>IEEE Trans. UFFC</i> 55, 2008, 1809-1822
[8]	N. Segebarth, O. Enlaerts, J. Reisse, L.A. Crum, T.J. Matula, “Correlation between acoustic cavitation noise, bubble population, and sonochemistry”, <i>J. Phys. Chem. B</i> 106, 2002, 9181-9190
[9]	M. Ashokkumar, M. Hodnett, B. Zeqiri, F. Grieser, G.J. Price, “Acoustic emission spectra from 515 kHz cavitation in aqueous solutions containing surface-active solutes”, <i>J. Am. Chem. Soc.</i> 129, 2007, 2250-2258

[10]	K. Negishi, "Experimental Studies on Sonoluminescence and Ultrasonic Cavitation", J. Phys. Soc. Jpn. 16 (1961) 1450-1465
[11]	A. Henglein, R. Ulrich, J. Lilie, "Luminescence and chemical action by pulsed ultrasound", J. Am. Chem. Soc. 111 (1989) 1974-1979

Detection of damaging cavitation states by means of ultrasonic signal parameter patterns

Peter Gruber*
Rittmeyer Ltd, Baar Switzerland
HSLU T&A, Lucerne, Switzerland

David Roos
HSLU T&A, Lucerne, Switzerland

Thomas Staubli
HSLU T&A, Lucerne, Switzerland

Christian Müller
KWO Kraftwerke Oberhasli
Innertkirchen, Switzerland

peter.gruber@rittmeyer.com

ABSTRACT

The effect of air and cavitation bubbles on ultrasonic signal parameters has been studied. Experiments have been carried out with a sphere submerged in water flow in a circular pipe. 1Mhz pulsed signals have been sent through the region where cavitation bubbles occur dependent on the flow and pressure conditions. The signals recorded at a fast rate, have been analyzed in order to find signal parameter patterns that can be used for a characterization of different water states: pure water, water/air bubble mixtures, and water/cavitation bubble mixtures. By looking in a statistical way at important signal parameters in the time and frequency domain, it was possible to distinguish the different water states for the experiments carried out with the sphere. As the results were promising, further experiments will be done with more realistic profiles.

INTRODUCTION

Pumps and turbines used in hydro power plants and water distribution systems may be exposed to cavitation especially for high flow rates if the suction pressure decreases. Low pressure regions build up in the water, which enable the generation of water vapor bubbles.

Slow time varying signals

Necessary conditions for the presence of regions where cavitation can occur, are derived from operating conditions specified by pressure, temperature, suction head, power, control values and local velocities ([1], Avellan). These measured values are operating point dependent and normally slowly time-varying leading to slow time-varying recorded signals (stv-signals).

Fast time varying signals

Beside these operating parameters other quantities have also a decisive influence on the generation of damaging cavitation in the water: these quantities describe the water conditions (turbulence, nuclei concentration, viscosity) and bubble conditions (bubble size, growth and decay, pressure waves, bubble concentration) and are of a fast time varying nature, called ftv-signals. Physical models of different complexity exist that

describe the effect of the above quantities on the recorded ftv-signals ([2], Leighton). Some of the physical relations are well established, others are less clear.

The scattering for instance of the acoustic pulses at bubbles and clouds of bubbles is known ([3], Brennen). To describe the overall behaviour of acoustic pulses in the presence of multiple bubbles statistical methods must be used.

The formation of vapor bubbles in cavitation in hydraulic machine is not a major problem in itself but it can cause detrimental effects to the operation of hydraulic machines in two ways ([4], Agrawal) :

Collapse of small bubbles: The collapse of these bubbles generates pressure waves, which can be of very high frequencies, causing damage to the machinery. Damage is caused by: 1) The bubbles collapsing near the machine surface are more damaging and cause erosion on the surfaces called as cavitation erosion. 2) The collapses of smaller bubbles create higher frequency waves with more potential for damage than larger bubbles. So, smaller bubbles are more detrimental to hydraulic machines and their efficiency.

Generation of large bubbles: Smaller bubbles may be more detrimental to the hydraulic machine body but they do not cause any significant reduction in the efficiency of the machine. With further decrease in static pressure a higher number of bubbles is formed and their size also increases. These bubbles merge with each other to form larger bubbles and eventually pockets of vapor. This disturbs the liquid flow and causes flow separation which reduces the machine performance sharply. Cavitation is an important factor to be considered while designing hydraulic turbines.

To avoid cavitation while operating hydraulic turbines parameters should be set such that at any point of flow static pressure may not fall below the vapor pressure of the liquid. These parameters to control cavitation are pressure head, flow rate and exit pressure of the liquid. The control parameters for cavitation free operation of hydraulic turbines may be obtained by conducting tests on model of the turbine under consideration.

The parameters beyond which cavitation starts and turbine efficiency falls significantly should be avoided while operation of hydraulic turbines.

As stated above, the implosions of vapor bubbles under rising pressure can cause erosion of material if this occurs close to the surfaces of the runner or other non-moving parts of the machine. In long terms the erosion leads to a decrease of the efficiency and/or the total loss of these parts. As cavitation is always accompanied by noise and vibrations the monitoring systems of today use this information by hydrophone and vibrational measurements beside the operating point information and if possible optical inspection for detecting bubbles ([5], Egusquiza). A problem with such measurement methods is the obtained patterns often provide only necessary but not sufficient conditions for the occurrence of damaging cavitation. Thus too many states are detected which results in a too conservative diagnosis. The goal of a monitoring system is to avoid operation of pump and turbines in critical operating points (damaging cavitation) and only in these points, not in all operating points where cavitation occurs.

MAIN BODY

Acoustic transit time discharge measurement

The well-established ultrasonic flow measurement by transit time method allows to determine averaged path flow velocities \bar{v}_a and averaged sound velocities \bar{c} per path:

$$t_{12} = \frac{L}{\bar{c} - \bar{v}_a \cdot \cos(\varphi)}$$

$$t_{21} = \frac{L}{\bar{c} + \bar{v}_a \cdot \cos(\varphi)}$$

$$\begin{aligned} \bar{v}_a &= \frac{L}{2 \cdot \cos(\varphi)} \cdot \left(\frac{1}{t_{21}} - \frac{1}{t_{12}} \right) \\ &= \frac{L}{2 \cdot \cos(\varphi)} \cdot \left(\frac{\Delta t}{t_{21} \cdot t_{12}} \right) \end{aligned}$$

$$\bar{c} = \frac{L}{2} \cdot \left(\frac{1}{t_{21}} + \frac{1}{t_{12}} \right)$$

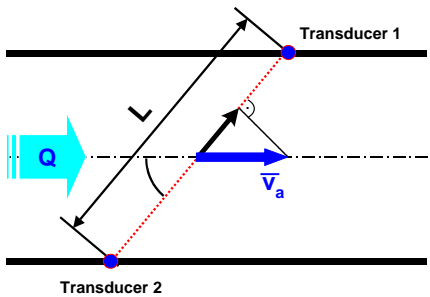


Fig. 1: Transit time measurement method

The method is usually applied in multipath configurations and delivers flow velocities and flows in hydraulic turbine to a high accuracy (< 1%). A precondition for an accurate measurement is however that the water conditions are good. That means low

particle and bubble concentration and reasonable hydraulic conditions. The hydraulic conditions are estimated by expertise and CFD simulations, while particle concentration is normally measured by probes or turbidity measurements. The effect of particles in the water on the forward scattered acoustic pulses used for the transit time method, has been studied by Gruber & al. [6]. The aim of this study was to examine the effect of particle size, concentration, material and shape on the amplitude and the water /particle suspension sound speed. As particle concentration is typically low (<10%), the effect on the suspension sound speed is negligible, whereas the amplitude shows a good dependency on the particle concentration and particle size. As the acoustic signals are recorded at a rate of approximately one hundred times per second, amplitude variations can be evaluated at a high rate. By averaging the amplitude information over a certain period of time it is therefore possible to estimate the particle concentration if the average particle diameter is known. In this way the flow meter can be used as a particle concentration monitoring device, allowing to detect particle concentrations which are unfavourable for the proper operation of the turbine.

The functionality of the ultrasonic method of a flow meter can further be enhanced if it would be possible to monitor by several additional acoustic paths the existence of air bubbles and/or vapour bubble caused by the cavitation effect. Especially the monitoring of the potentially damaging collapse of small vapour bubbles close to the machine surface would be of importance.

Beside the forward scattering signals (direct path) exploited in the transit time method, the reflected signals (reflected path) from the bubbles or surfaces can be analysed. This allows to study the effect of bubbles more from a different point of view. There are two arguments in favour of such a measurement method:

- 1) As the ultrasonic pulses can be directed close to the regions where damaging cavitation occurs, the effects of the bubbles and of the pressure waves on the pulses itself can directly be measured.
- 2) As many measurements are available per second, statistical signal parameters can be used for the characterisation of the different water conditions.

Experimental setup

In the hydraulic laboratory at the HSLU in Lucerne an experimental set up with a fully submerged sphere in a pipe was used. The dimension of the pipe was 9.2cm and the diameter of the sphere 4.9cm. In order to operate the flow under various cavitating conditions, the pump speed n and the flow Q could be varied. The flow Q is regulated by manipulating a plate slide at the end of pipe.

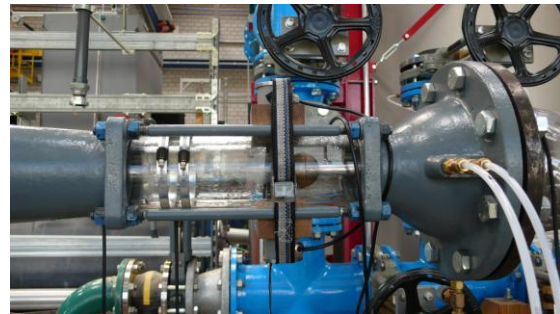


Fig. 2: cavitation test rig

Fig. 2 shows the cavitation test rig. In order to generate cavitating states the pressure in certain regions of the water has to reach the evaporating pressure of the water for the given water temperature. These regions are located there where the difference between pipe and sphere is minimal, that means on a vertical circle of the sphere. As the velocity v is maximal at these locations the static pressure must be minimal. This pressure is measured at one point on the vertical circle (top). Additional pressure sensors are located at the downstream centre position of the sphere and the entrance of the water in the pipe. The pump speed was varied between providing a flow rate between 40 and 55 l/s. generating velocities between 6 and 8m/s. The low speed operating points were chosen such that clearly no cavitation could be observed. From 900 revolutions per minute upwards several states of cavitation could be observed. The cavitation number σ varied between 0.8 and 0.45. In order to study the difference between cavitation bubbles and pure air bubbles in some measurement series air bubbles have been additionally injected. The size of these bubbles was however not controlled and its concentration only measured qualitatively by inspection.

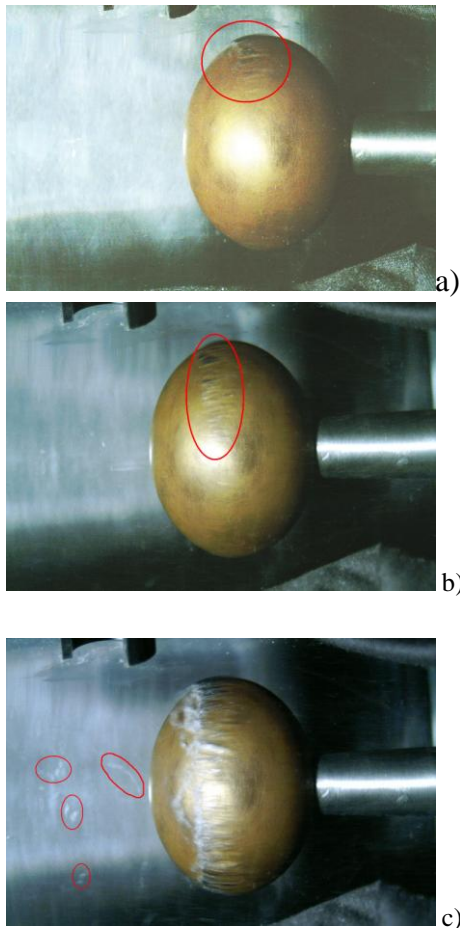


Fig. 3: a) weak cavitation, b) intermediate c) strong cavitation

Ultrasonic measurement configurations

The acoustic path arrangements were chosen such, that the paths are directed right through the regions where the cavitation occurs. The sensor frequency was 1MHz in a pulsed mode with an emitted pulse duration of a few cycles of the sensor frequency. The repetition rate of the signal was 100Hz. The sensors have a relatively small bandwidth and a narrow opening angle. The sensors are mounted such that the sensor pills are wetted by the water. Three different configurations were installed:

One sensor in reflecting mode

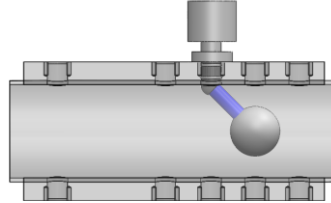


Fig. 4: reflecting mode with one sensor

The path is directed to the interesting sphere surface. The acoustic signal is reflected at the surface and is received by the same sensor that emitted the pulse. For pure water conditions no reflections occur during the travelling phase of the pulse.

Two sensors in reflecting mode

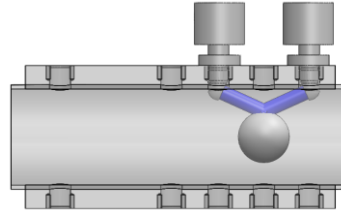


Fig. 5: Reflecting mode with two sensors

The two paths are arranged such that acoustic signal is reflected at a certain angle at one position of the critical surface of the sphere. One sensor acts as transmitter, the other one as receiver. An alternating mode where the sensors are switching between transmitter and receiver is an option too. Bubbles will influence the travelling phase of the pulse.

Two sensors in direct mode

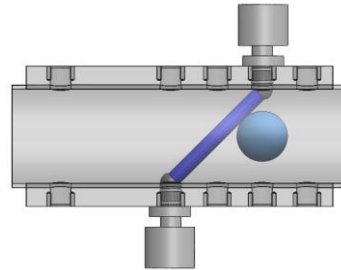


Fig. 6: Direct mode

In this configuration the two sensors are arranged as in the usual flow measurement method based on transit time determination. No reflecting signals from bubbles or surfaces are processed in this mode, except for forward reflected signals to the opposite sensor which might be present.

Another variation with the sensor configuration exists if the sensors are mounted in a clamp-on fashion from the outside without the necessity of drilling holes. The advantage of this mounting procedure is its flexibility and easiness of installation, its drawback the signal loss and additional angles of refraction. The total number of examined configurations is shown in Fig. 7.

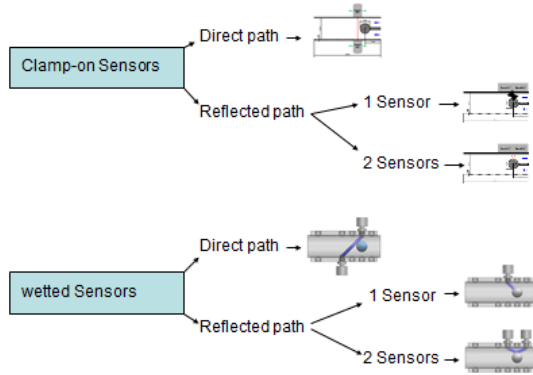


Fig. 7: Different path and sensor configurations

Each test consists of 100 consecutive signals sampled at 25MHz which are then analysed off-line.

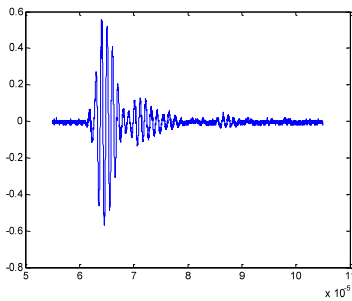


Fig. 8: Receiving Signal for a wetted 2 sensor reflected arrangement, pure water regime

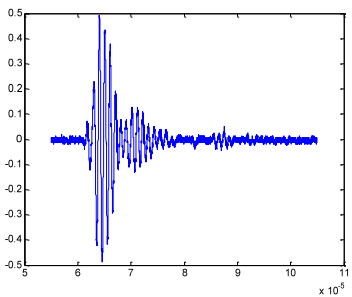


Fig. 9: Receiving Signal for a wetted 2 sensor reflected arrangement, air bubble regime

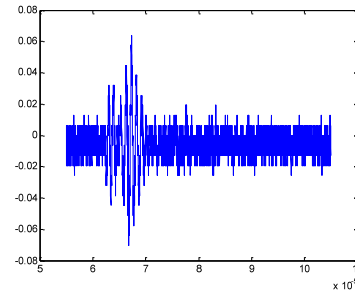


Fig. 10: Receiving Signal for a wetted 2 sensor reflected arrangement, cavitating regime

The experiments have been carried out by Müller [8] and Roos [9]. Approximately 100 test series have been carried out.

Analysed characteristic parameters of acoustic signal

In a first analysis only fundamental statistical signal parameters have been examined. These are:

Time domain:

Maximum of Amplitude

mean value μ

standard deviation σ

histogram

Time index of occurrence of maximum of amplitude, not scaled (transit time)

mean value μ

standard deviation σ

histogram

Frequency domain:

averaged amplitude spectrum (not scaled) $A(f)$

standard deviation of amplitude spectrum (not scaled) $\sigma_{A(f)}$

sum of $A(f)$ in 0-2.5MHz frequency band (power)

sum of $\sigma_{A(f)}$ of amplitude spectrum

shape of averaged amplitude spectrum

shape of standard deviation of amplitude spectrum

center of mass of frequency content

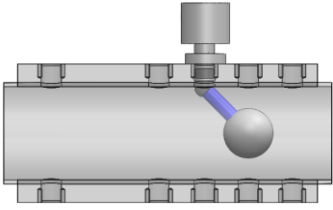
3 local maxima of averaged amplitude spectrum

3 local maxima of standard deviation of amplitude spectrum

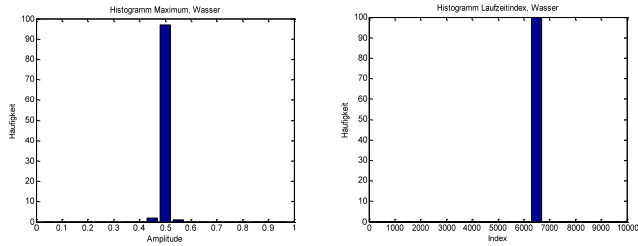
Results

Results are only shown for wetted sensor arrangements. Care has to be taken if one has to interpret the figures because of the different scaling in the y-direction.

One sensor arrangement in reflecting mode

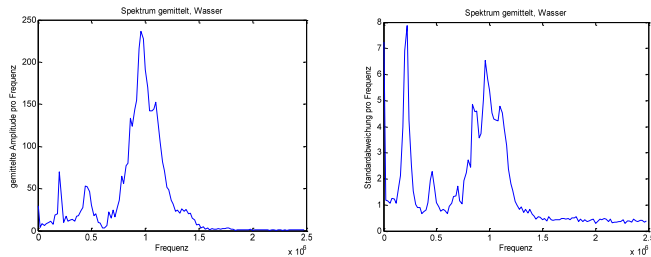


water only



Histogram of amplitude maxima

Histogram of time of occurrence (index) of amplitude maxima

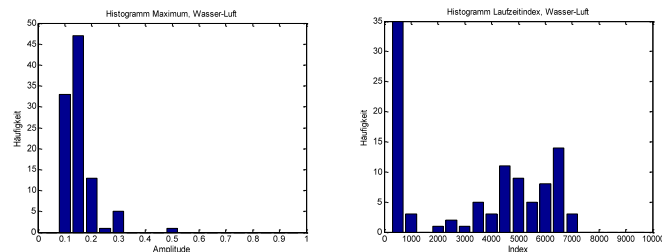


Averaged spectrum (0-2.5MHz)

Standard deviation of spectrum (0-2.5MHz)

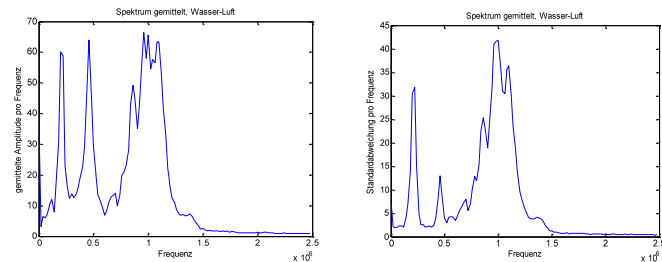
Fig. 11a-11d: statistical properties of water state for one sensor in reflecting mode

air bubbles



Histogram of amplitude maxima

Histogram of time of occurrence (index) of amplitude maxima

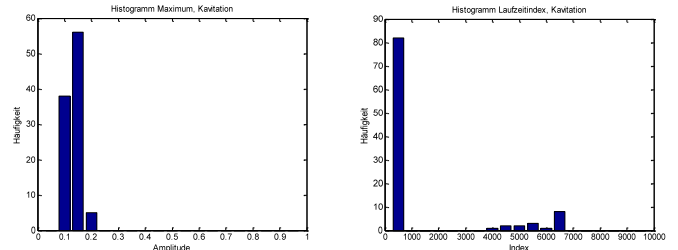


Averaged spectrum (0-2.5MHz)

Standard deviation of spectrum (0-2.5MHz)

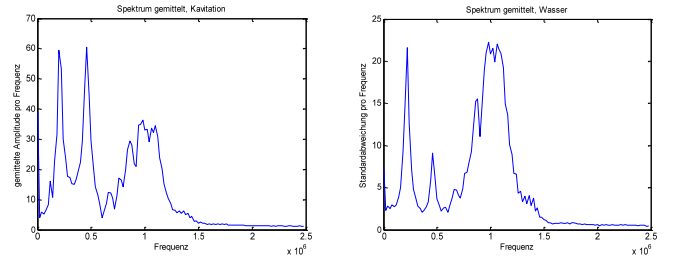
Fig. 12a-12d: statistical properties of air bubble state for one sensor in reflecting mode

cavitation bubbles



Histogram of amplitude maxima

Histogram of time of occurrence (index) of amplitude maxima



Averaged spectrum (0-2.5MHz)

Standard deviation of spectrum (0-2.5MHz)

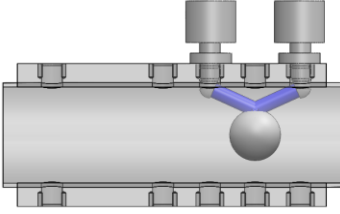
Fig. 13a-13d: statistical properties of cavitation bubble state for one sensor in reflecting mode

In the following table the characteristic statistical parameters are summarized for four series of measurements series of the one sensor reflecting mode configuration: one water only, one water/air bubble and two water/cavitation bubble measurement series (different pump speed).

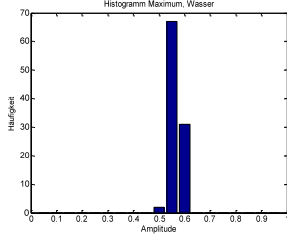
	water 1 Sensor reflect	air 1 Sensor reflect	Cav (950) 1 Sensor reflect	Cav (1000) 1 Sensor reflect
μ Max	0.50	0.15	0.18	0.13
σ Max	0.0013	0.034	0.076	0.006
μ time index	6434	3298	3085	1042
σ time index	3.63	2613	3234	2155
Frequency Center of mass kHz	920.409	788.747	808.270	725.699
power	4088	1941	2001	1533
σ power	194	915	1013	626
Histogram Amp	narrow symm.	broad asymm.	broad asymm.	narrow asymm
Hist Zeit	very narrow	very narrow	2 bumps Symm.	2 bumps Asymm.
Max f1	70	60	61	60
Max f2	53	64	62	60.5
Max f3	236	66	73	36
σ f1	7.8	32	20	22
σ f2	2.3	13	8.5	9
σ f3	6.5	42	62	22

Table 1: Characteristic statistical parameters for 1 sensor in reflection mode

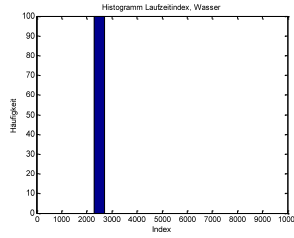
Two sensor arrangement in reflecting mode



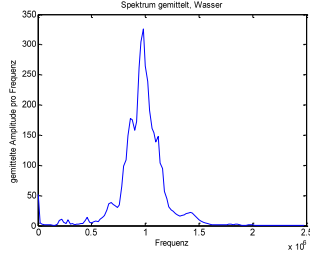
water only



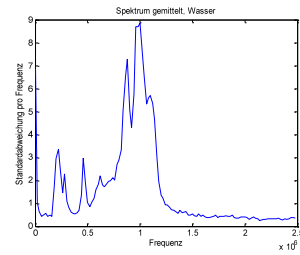
Histogram of amplitude maxima



Histogram of time of occurrence (index) of amplitude maxima



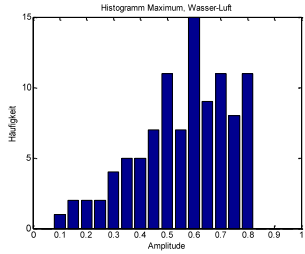
Averaged spectrum (0-2.5MHz)



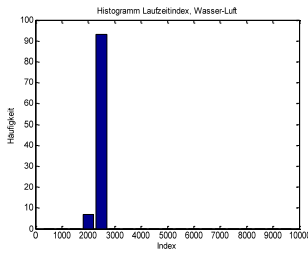
Standard deviation of spectrum (0-2.5MHz)

Fig. 14a-14d: statistical properties of water state for two sensor in reflecting mode

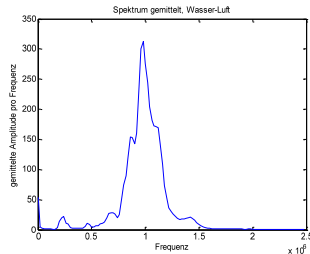
air bubbles



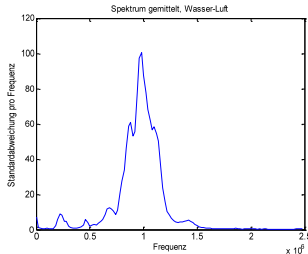
Histogram of amplitude maxima



Histogram of time of occurrence (index) of amplitude maxima



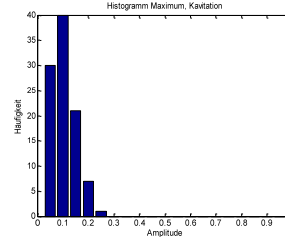
Averaged spectrum (0-2.5MHz)



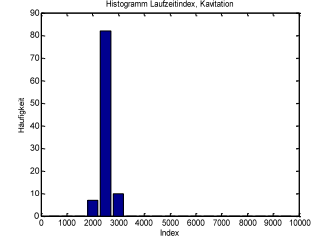
Standard deviation of spectrum (0-2.5MHz)

Fig. 15a-15d: statistical properties of air bubble state for two sensor in reflecting mode

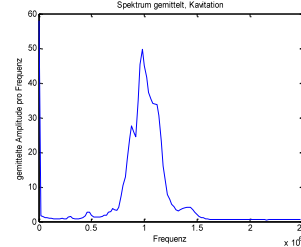
cavitation bubbles



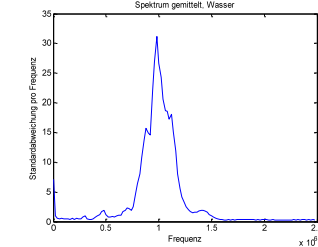
Histogram of amplitude maxima



Histogram of time of occurrence (index) of amplitude maxima



Averaged spectrum (0-2.5MHz)



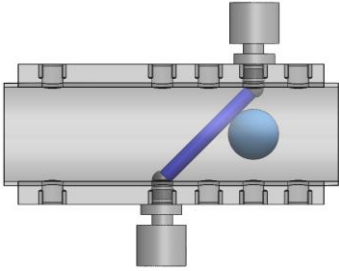
Standard deviation of spectrum (0-2.5MHz)

Fig. 16a-16d: statistical properties of cavitation state for two sensor in reflecting mode

	water 2 Sensor reflect	air 2 Sensor reflect	Cav (950) 2 Sensor reflect	Cav (1000) 2 Sensor reflect
μ Max	0.56	0.56	0.25	0.11
σ Max	0.003	0.3	0.13	0.02
μ time index	2272	2302	2454	2532
σ time index	3.7	81	135	205
Frequency Center of mass kHz	969.173	977.149	967.017	956.742
power	4412	4380	1860	833
σ power	205	1490	913	442
Histogram Amp	narrow asymm.	v. broad asymm.	broad asymm.	narrow asymm
Hist Zeit	very narrow	very narrow	very narrow.	very narrow.
Max f1	11	22	2	1.5
Max f2	13	11	5	3
Max f3	326	313	135	50
σ f1	3.5	9	1.5	1
σ f2	3	6	3	2
σ f3	9	100	66	31

Table 2: Characteristic statistical parameters for 2 sensor in reflection mode

Two sensor arrangement in direct mode



water only

Wasser (2 Sensoren, 45°) n=600

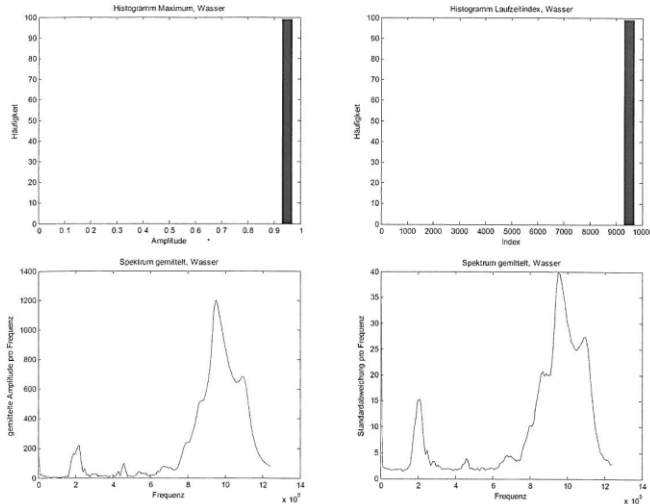


Fig. 17a-17d: statistical properties of water state for two sensors in direct mode

air bubble

Viel Luft (2 Sensoren, 45°) n=600

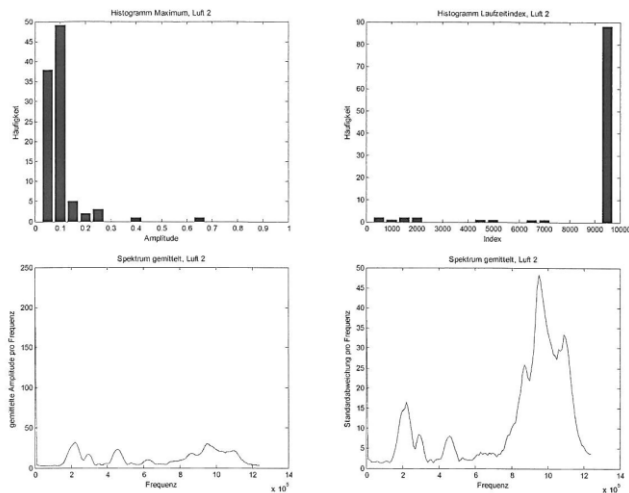


Fig. 17a-17d: statistical properties of water state for two sensors in direct mode

- a Histogram of amplitude maxima b Histogram of time of occurrence (index) of amplitude maxima
c Averaged spectrum (0-2.5MHz) d Standard deviation of spectrum (0-2.5MHz)

cavitation bubbles

Kavitation (2 Sensoren, 45°)

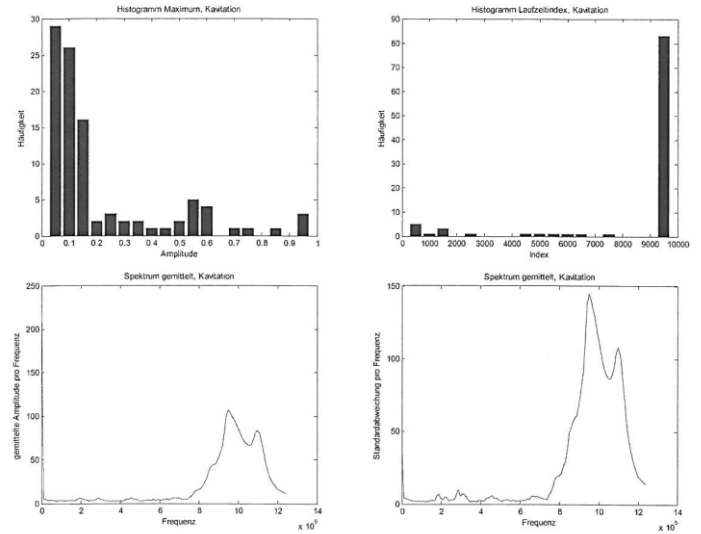


Fig. 18a-18d: statistical properties of cavitation state for two sensors in direct mode

- a Histogram of amplitude maxima b Histogram of time of occurrence (index) of amplitude maxima
c Averaged spectrum (0-2.5MHz) d Standard deviation of spectrum (0-2.5MHz)

The histograms of the time index distribution for the cases air bubbles and cavitation bubbles is not correct. The time of occurrence is prone by the fact, that if bubbles block the signal path too much, then the maximal amplitude of the received signal is obtained randomly and is of a very low value and may occur at small indices. In the case of air bubbles 11 time indices are wrong (too low), in the case of cavitating bubbles 16 time indices are wrong (too low). Therefore they are omitted.

	water 2 Sensor direct	air 2 Sensor direct	cavitation 2 Sensor direct
μ Max	0.95	0.1	0.21
σ Max	0.038	0.054	0.558
μ time index	9500	~9500	~9500
σ time index	-	-	-
Frequency Center of mass kHz	921.875	602.121	870.657
power	28512	1651	3021
σ power	1204	1454	3558
Histogram Amp	very narrow	asymm.	broad asymm.
Hist Zeit	very narrow	very narrow	narrow.
Max f1	219	32	6.5
Max f2	100	23	6
Max f3	1201	30	107
σ f1	15	16.5	10
σ f2	3.9	8	5.8
σ f3	40	48	145

Table 3: Characteristic statistical parameters for 2 sensors in direct mode

Interpretation of the results

The results obtained lead to the following conclusions:

- As expected all averaged spectra show a dominant peak at the sensor frequency.
- Specific subharmonic components are visible in all cases.
- The wateronly state can always be easily detected in the time and frequency domain.
- The distinction between the air bubble state and cavitation bubble state is more subtle..
- 1 sensor in reflected mode: differences can be found in the histograms of the time indices and in the standard deviation of the subharmonic components.
- 2 sensors in reflected mode: differences can be found for the standard deviation σ_{Max} , $\sigma_{time-index}$, the power and in the values of the subharmonic components.
- 2 sensors in direct mode: differences can be found for the standard deviation σ_{Max} , and σ_{power} .

For these characteristic parameters it would be possible to define thresholds that would be capable to distinguish the three water states:

- Water only
- Water and air bubbles
- Water and cavitation bubbles

In reality there exists often a mixture between air and cavitation bubbles, so distinction between these two states will not be easy with the introduced statistical parameters. A similar inspection of some of the above parameters allows the distinction between the above water states and a water state where water is loaded by silt particles.

Detection unit

As the results were promising with the sphere experiments further measurements will be undertaken with more realistic objects in the cavitation test rig at the LMH laboratory at the ETH Lausanne. Different profiles with different setting angles of the blade will be examined with different path configurations and sensor frequencies. The next idea is to develop a monitoring and detection system for the different water states in a turbine or pump as is proposed in Fig.19. Another possibility is to include not only ultrasonic measurements but also measurements from vibrations sensors, hydrophones and optical methods. This combination of different signals would require an additional detection block.

Outlook

The obtained results were gained by experiments only by exploiting statistical parameters describing the influence of air and cavitation bubbles. Many questions are still unanswered. Therefore the next steps in applying this method are:

- Develop a physical foundation for the observed dependencies.
- Application of other time frequency analysis tools as Wavelets
Empirical mode decomposition (EMD)
Fractional Fourier transform
Hilbert transform
Cepstrum and others

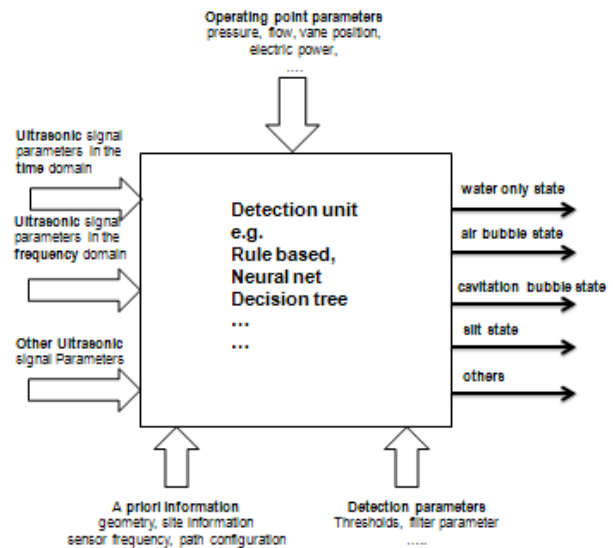


Fig. 19: Water state detection unit based on ultrasonic signal analysis

- Use of sensors with different frequencies (100kHz – 2MHz) and wider bandwidth (600-800 kHz)
- Use of multipath information
- Measurements at model turbines or pumps
- Study the effect of the ultrasonic pulses on the bubbles
- Study the effect of damaging bubble collapses up- and downstream of the location of occurrence for the case where it is impossible to install acoustic paths at this location

There is strong evidence that by combining ultrasonic measurement information with other measurements (hydrophone, vibration, optical,...), the monitoring of the dangerous cavitation states can be improved.

ACKNOWLEDGMENTS

The authors like to thank for the support obtained by the HSLU internal research fund for carrying out these measurements.

REFERENCES

- [1] F. Avellan: Introduction to cavitation in hydraulic machinery, HMH 2004, Timisoara, Romania,
- [2] T. D. Leighton: The acoustic bubble, 1994 Academic Press
- [3] C. E. Brennan: Cavitation and bubble dynamics, 1995 Oxford University Press
- [4] N. Agrawal: Cavitation in hydraulic turbines: Causes and Effects, 2007
- [5] E. Egusquiza: Remote monitoring of cavitation in Francis turbines, 2nd WIMRC Cavitation Forum 2008
- [6] P. Gruber, B. Lüscher: Silt monitoring via ultrasonic signal analysis, IGHEM 2010, Roorkee, India
- [7] H. Shamsborhan, O. Cloutier-Delgosha, G. Caignaert: Measurement of the speed of sound in Two-phase Flows with high void fraction, 2nd WIMRC Cavitation Forum 2008
- [8] C. Müller: Untersuchung der Kavitation mit Ultraschall an zwei Prüfstrecken, Diploma thesis, 2008, HTA Lucerne
- [9] D. Roos: Kavitationsmonitoring mittels Ultraschall, Industrieprojekt 2008, HTA Lucerne

Effect of acoustic cavitation on saturated nucleate pool boiling

Sreenath Krishnan/Department of Mechanical
Engineering, IIT Madras, Chennai 600036, India

Sarit K Das/Department of Mechanical
Engineering, IIT Madras, Chennai 600036, India

Dhiman Chatterjee*/Department of Mechanical
Engineering, IIT Madras, Chennai 600036, India

Email: dhiman@iitm.ac.in

ABSTRACT

Saturated nucleate pool boiling over a horizontal circular heater surface in the presence of acoustic field has been studied and it was found that acoustic field influences the heat transfer characteristics depending on the amplitude and frequency of the acoustic field and the heat flux applied. There was a slight deterioration of heat transfer at lower pressure amplitudes followed by an initiation zone where the enhancement sets in, at both 47 and 140 kHz. The enhancements were increasing with heat flux. Photographic studies that were conducted reveal the changes in bubble density near the heater surface in the presence of acoustic field and the extent of acoustic streaming present. It has been found that bubble density slightly increases near the heater surface but streaming phenomenon is absent. A simple model is put forward to explain the results. The predictions of the model are in good agreement with the results obtained

R_a	Arithmetic average of absolute values of roughness
P_c	Critical Pressure amplitude
NSD	Nucleation site density
Pr	Prandtl number
CHF	Critical heat flux
NSD_{max}	Maximum possible NSD
$NSD_{available}$	Available NSD
D_b	Bubble departure diameter from heater surface
β	Contact angle
g	Acceleration due to gravity
N_{max}	Maximum number of bubbles that can be present on the heater surface
A_s	Surface area of heater
P_e	Pressure amplitude at which NSD tends to NSD_{max}
f	Bubble departure frequency

NOMENCLATURE

Symbol	Definition
PZT	Lead zirconate titanate
D	Diameter of heater surface
h	Heat transfer coefficient
q	Heat Flux
ΔT	Wall superheat
E	Percentage enhancement in heat transfer coefficient
h_a	Heat transfer coefficient in the presence of acoustic field
ΔP	Pressure difference
σ	Surface Tension
r	Radius of cavity
P_a	Acoustic pressure amplitude
h_{fg}	Latent heat of vapourization
T_s	Saturation temperature
ϑ_l	Specific volume of liquid water
ϑ_v	Specific volume of water vapour
ρ_l	Density of liquid water
ρ_v	Density of water vapour

1. INTRODUCTION

The development in the technology has elevated the demand for the miniaturized cooling of ultra-high heat flux devices to very high proportions. Air based cooling systems, water cooling and cooling with refrigerants that are used to solve these thermal challenges have been proved unsatisfactory at high heat fluxes because of their poor reliability, poor cooling characteristics and toxic nature, which is hazardous to environment, respectively. This has turned the researches towards two-phase coolants because of the higher heat transfer coefficients they can generate. Two-phase cooling in the form of boiling utilizes the constant temperature heat absorption by a fluid undergoing a liquid-to-gas phase change to remove additional heat from the cooled hardware. In addition, the process of vapour bubbles forming on the hot surface and then moving into the bulk liquid results in fluid movement which further increases convection. However, boiling heat transfer is limited by the critical heat flux. Research into enhanced boiling seeks to improve the heat transfer from a surface at a given surface temperature or extend the critical heat flux limit. Acoustic cavitation could potentially bring out enhanced boiling, primarily due to the influence it would have on nucleation process and bubble dynamics.

Pool boiling takes place for a liquid initially at stagnant state and the heated surface on which boiling occurs is submerged into it. Once the wall superheat is sufficiently high to overcome the surface energy associated with a vapour-liquid interface (Wang and Dhir[1]), small bubbles begin to form, grow, and depart from the nucleation sites on the surface. Nucleation sites are small cracks or cavities on the surface where air or vapour is trapped. This is known as nucleate boiling.

Enhanced boiling methods can be either active or passive. Passive methods require no external power input and often involve surface modifications. Active methods require an external power input and often involve removal of vapour bubbles from the boiling surface to increase the heat transfer.

Since bubbles play pivotal role in both boiling and cavitation, the simultaneous presence of these phenomena is expected to bring out interesting physics. The effect of acoustic waves on nucleate pool boiling was first investigated by Isakoff [2]. He did not observe any shift in the boiling curve, but found an improvement in the critical heat flux. Wong and Chon [3] studied the effect of ultrasonic vibrations on both natural convection and pool boiling using ultrasound between 20.6 kHz to 306 kHz and showed that below a critical sound pressure the effects on heat transfer are negligible. Natural convection was significantly increased above this critical pressure. But nucleate boiling was unaffected. Park and Bergles [4] found that there is a deterioration of saturated pool boiling, but saw an improvement of around 5-10% for subcooled boiling in the presence of ultrasonic field.

However, in the recent investigations, researchers have reported enhancement of boiling in the presence of acoustic field. Kim et al [5] found enhancement in natural convection and at the onset of boiling. The enhancement was relatively higher at lower heat flux and was more for subcooled boiling. They also found that the behaviour of cavitation bubbles strongly affect the heat transfer enhancement in natural convection and subcooled boiling. However in saturated boiling, acoustic streaming and reduction of bubble departure diameter are the major factors. Zhou et al [6] studied subcooled boiling heat transfer in an acoustic field and reported that boiling is remarkably enhanced.

It is clear from above that there is a controversy regarding the effect of ultrasonic field on pool boiling. A reason could be that all parameters related to ultrasonic field was not properly controlled. This work is an attempt to give a clear picture of the effect of acoustic field on saturated pool boiling by systematically varying acoustic parameters like pressure amplitude and frequency.

2. EXPERIMENTAL SETUP AND METHOD

The pool boiling experimental setup (Figure 1) consists of a boiling vessel, a condenser with cooling water circulation and an auto-transformer regulated power supply. The boiling vessel is made of double-walled high temperature toughened

glass with stainless steel supports at four corners. Foam insulation was applied to the exterior of these four stainless steel supports to prevent heat loss. A stainless steel plate of 3mm thickness was fixed to the bottom of the glass vessel, which holds the main heater. Two secondary heaters, sufficiently away from the main heater, were fixed to the bottom plate at two corners diagonally opposite to each other. These heaters are used for preheating the boiling liquid, degasification, and to ensure saturated boiling.

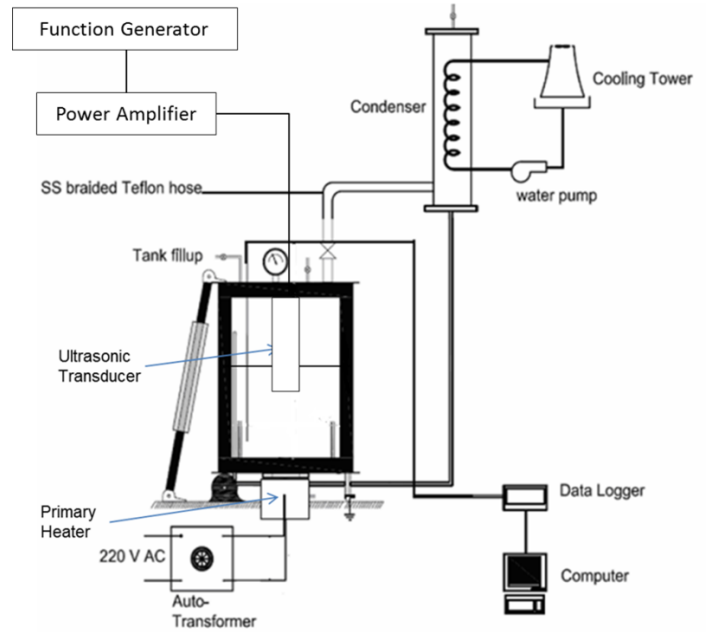


Figure 1: Schematic of pool boiling experimental setup

In order to maintain atmospheric pressure while boiling, a valve at the top of the setup is kept partially open to the atmosphere. The main heater (Figure 2) is a flat plate copper heater with diameter of heater surface around 2 cm. It consists of aluminium cylindrical heater in which heat is generated, circular copper taper block, which is tapered with the initial diameter of 5 cm for 1.6 cm height and the rest of the height of 4 cm length with 3.5 cm diameter, through which heat is conducted to the top polished copper heating block of 1 cm height, which has a diameter of 3.5cm for initial 0.4cm height and rest 0.6cm with 2.5cm diameter, whose top flat surface is in contact with the boiling liquid. Both heater and copper block are confined tightly inside the Teflon block casing which also acts as good insulation. Insulation is done also with the glass wool between the Teflon block and the inside heater to make sure that heat transfer is unidirectional. The contact resistances, if any, between the copper block and aluminum heater is reduced by applying Anabond 652 thermal paste between them. The heater is confined tightly inside the Teflon block casing which also acts as good insulation. To find the surface wall temperature of the main heater a series of 5 thermocouples are fixed into the copper block at different depths. To prevent any nucleate boiling from the clearance between Teflon block and heater surface, the clearance is closed by applying layer of paste of M-seal and araldite on it along the circumference. This will decrease the

effective diameter of heater surface. A thermocouple is inserted from the top to monitor bulk water temperature.

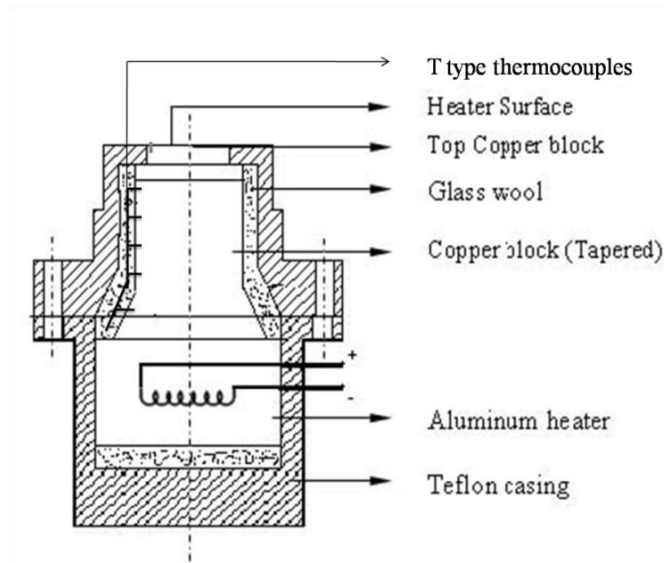


Figure 2: Main heater

The ultrasonic transducer produces the required acoustic field. The outer body of the transducer is made up of nylon block which can withstand temperatures up to 180°C. A PZT-4 piezoelectric crystal of diameter 50mm is used to produce acoustic waves. The waves are focused using a suitably designed parabolic graphite block. The transducer is well calibrated within the operating range. It is driven by a function generator and the signals are suitably amplified by power amplifier. Figure 3 shows the frequency response of the ultrasonic transducer. The transducer was driven at constant voltage and the current passing through it is measured using a current probe. The phase difference between the current and voltage is measured and the power is calculated. Figure 4 shows the variation of pressure amplitude at resonance with distance along the axis of the transducer at a particular driving voltage. The radial variation of pressure amplitude closely follows a Bessel function.

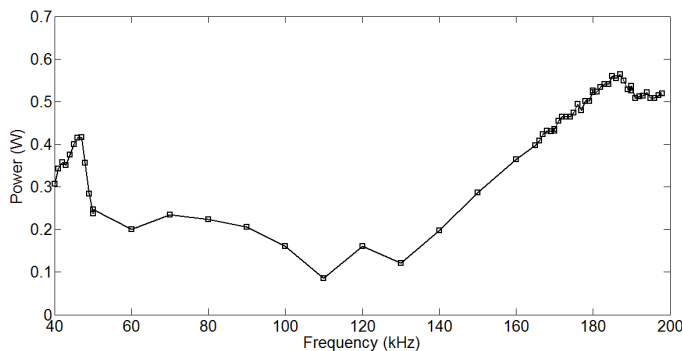


Figure 3: Frequency Response of the Ultrasonic Transducer

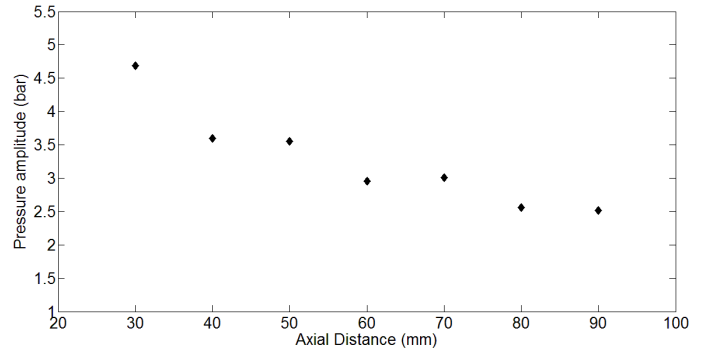


Figure 4: Variation of pressure amplitude along ultrasonic transducer axis at 47 kHz, 4V peak to peak, 31 dB

The experimental procedure is as follows. First, the liquid is heated to the boiling point by two secondary heaters. Once the boiling point is reached, the liquid is allowed to boil (by secondary heaters) for about 1 hour so as to remove the dissolved gases. When the whole liquid being boiled by the secondary heaters is at steady state, main heater is switched on and the power is slowly increased in steps to the maximum heat flux. For each heat flux, thermocouple readings are monitored to see if the steady state is achieved. Once steady state is reached, the ultrasonic transducer is switched on. The temperature is allowed to settle once more. After achieving steady state the ultrasonic transducer is set to a different desired voltage. Readings are scanned over an interval of 2 seconds. When the steady state at maximum heat flux is reached, the power supply is slowly decreased in steps to zero. The same sets of procedures are carried out for each heat flux as above as in the case while increasing heat flux. The uncertainty for the measurement of diameter (D) is $\pm 0.05\text{mm}$ which makes the uncertainty in the area (A) up to $\pm 0.5\%$. Likewise, the uncertainty for the heat flux is $\pm 0.6\%$. The uncertainty for temperature measurement can be due to uncertainty with measuring instrument, which is $\pm 0.10^\circ\text{C}$. The uncertainty for the boiling heat transfer coefficient is about $\pm 0.75\%$.

3. RESULTS AND DISCUSSION

Pool boiling experiments were conducted with de-ionized water in the absence of ultrasonic transducer. The results were in good agreement with Rohsenow correlation [7], which validates the reliability of experimental setup (Figure 5). The values are recorded while decreasing the heat flux. The nucleation sites that are activated as we increase the heat fluxes from lower to higher values fail to get deactivated when we are decreasing the heat flux from higher to lower values. Kenning [8] ascertained that experiments for laboratory purposes should be conducted with decreasing heat fluxes and hence in the present work, heat flux in the decreasing direction is considered for analysis. In order to ensure that geometric disturbance due to the presence of ultrasonic transducer does not affect the boiling heat transfer; the experiments were repeated with passive transducer. The results matched with those in the absence of transducer (Figure 5), thus confirming that the introduction of transducer does not affect bubble field.

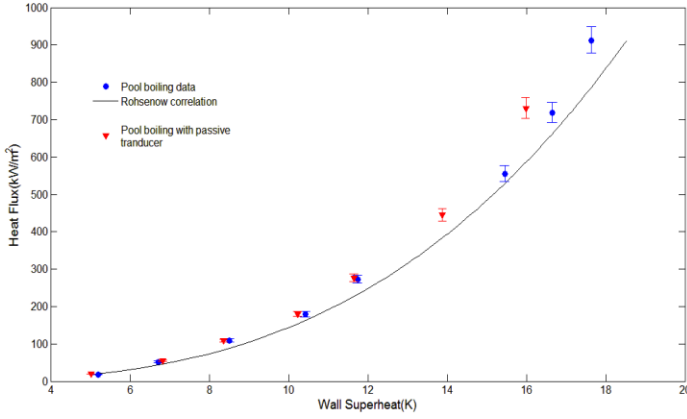


Figure 5: Comparison of pool boiling data with Rohsenow correlation

Pool boiling heat transfer coefficient is defined as:

$$h = \frac{q}{\Delta T} \quad (1)$$

The percentage change in heat transfer coefficient is defined as:

$$E = \frac{h_a - h}{h} \times 100 \quad (2)$$

Figure 6 shows the percentage change in pool boiling heat transfer coefficient in the presence of acoustic field of frequency 47 kHz at various pressure amplitudes and heat fluxes. The pressure values in the figure are the peak acoustic pressure amplitudes at the surface of the heater. The distance from the heater to the ultrasonic transducer was kept fixed at 55 cm. It is clear that the acoustic field significantly influences pool boiling. At lower pressure amplitudes (< 1 bar) there is a slight deterioration of pool boiling particularly at lower heat fluxes. There exists a critical pressure amplitude (around 1.1 bar) after which the enhancement in heat transfer coefficient becomes notable. The rate of enhancement with pressure amplitude falls down later.

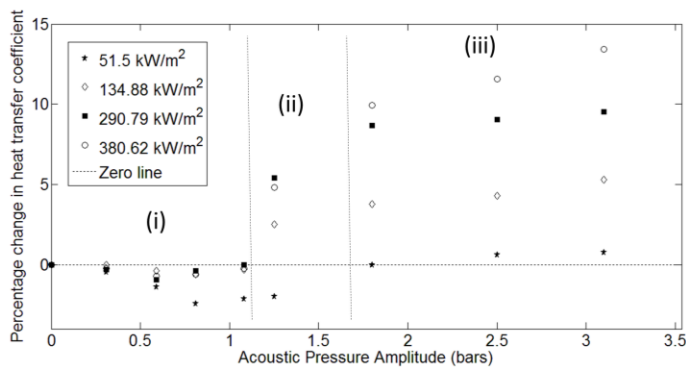


Figure 6: Change in heat transfer coefficient at 47 kHz acoustic field

The whole graph can be divided into three regions: (i) the deterioration zone, (ii) the enhancement initiation zone and

(iii) the enhancement flattening zone. It is also evident that the enhancement is a function of heat flux as well. Below the critical pressure amplitude, heat flux does not play any role. However there is a linear variation of enhancement with heat flux at higher pressure amplitudes. The maximum enhancement observed was about 13.5 %.

Photographic study of the phenomenon is carried using Canon EOS 1000D DSLR camera. It was also observed by photographic study that the bubble activity slightly increases at higher heat flux when acoustic field is applied. In Figure 7, photographs of the heater surface at heat flux of 390 kW/m² are shown. The first picture (Figure 7, left) shows the bubble activity in the absence of acoustic field, while the second one (Figure 7, right) shows the same in the presence of acoustic field with amplitude 3.1 bar and frequency 47 kHz, at the heater surface. It is evident that bubble population has increased and the bubbles are more distorted. This means that the acoustic field activates additional nuclei which are otherwise not activated. This could explain the reduction in wall superheat since heat transfer is enhanced as the nucleation sites increases. The acoustic field also sets up surface waves on the bubble surface, resulting in deformed shape.

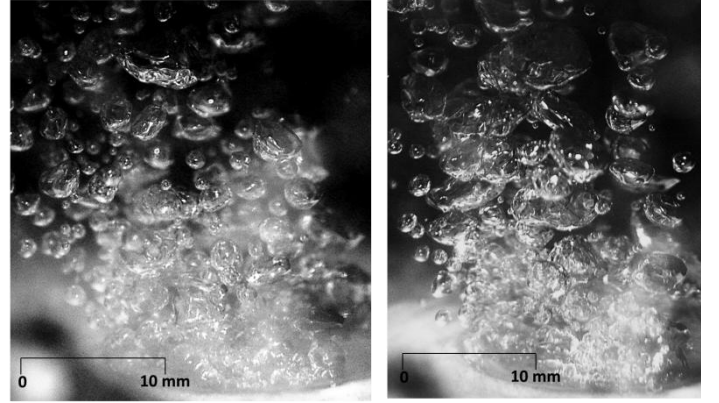


Figure 7: Comparison of bubble activity near the heater surface in normal pool boiling (left) and pool boiling in acoustic field 3.1 bar 47 kHz, 390 kW/m²

Figure 8 shows the percentage change in pool boiling heat transfer coefficient in the presence of acoustic field of frequency 140 kHz at various pressure amplitudes and heat fluxes. Similar to the behaviour at 47 kHz, at lower pressure amplitudes (< 1 bar) there is a slight deterioration of pool boiling. There exists a critical pressure amplitude (around 1.1 bar) after which the enhancement in heat transfer coefficient becomes notable. The data is available only till pressure amplitude of 1.5 bar due to the restriction of power amplifier. Hence only two zones are evident in the graph: (i) the deterioration zone and (ii) the enhancement initiation zone. There is significant overlap between these two zones at both 47 kHz and 140 kHz.

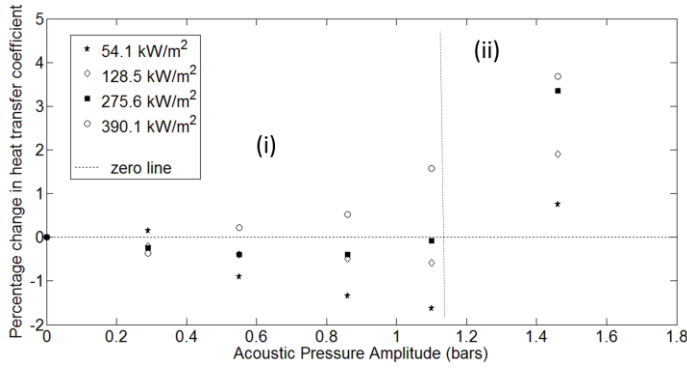


Figure 8: Change in heat transfer coefficient at 140 kHz acoustic field

It could be concluded that these zones are primarily functions of pressure amplitude and the enhancement initiation is clearly related to additional nuclei activation, which depends largely on pressure amplitude. Even though the characteristics of the plots at both frequencies are similar, the magnitudes of enhancements are different. Hence frequency also plays a role in the heat transfer process. The effect of heat flux is also similar to that at 47 kHz. A linear variation of enhancement with heat flux is found after the critical pressure amplitude.

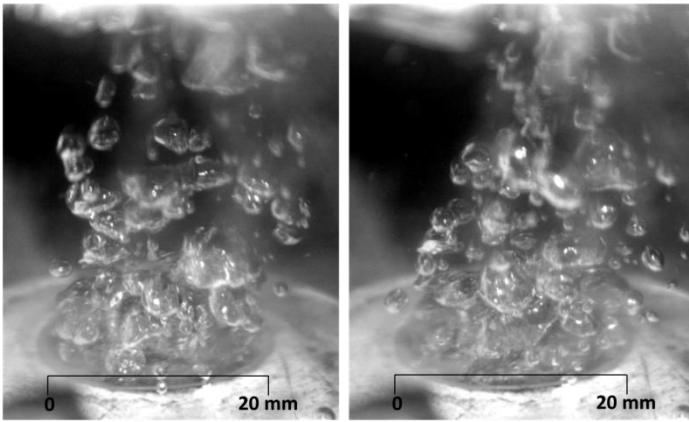


Figure 9: Bubble activity in the vicinity of the heater in the absence of acoustic field (left) and in the presence of acoustic field (right), 1.46 bar 140 kHz, 275 kW/m²

Photographic study of the bubble activity near the heater surface has the same trends to convey as in 47 kHz. The bubble density slightly increases at higher heat flux when acoustic field is applied. In Figure 9, photographs of the heater surface at heat flux of about 275 kW/m² are shown. The first picture (Figure 9, left) shows the bubble activity in the absence of acoustic field, while the second one (Figure 9, right) shows the same in the presence of acoustic field with amplitude 1.46 bar and frequency 140 kHz, at the heater surface. It is evident that bubble population has increased and the bubbles are more distorted as in the previous case.

Acoustic field can primarily cause two effects: cavitation and streaming. It is very difficult to visualize cavitation process. However acoustic streaming is relatively easy to visualize. Acoustic streaming is a steady current in a

fluid driven by the absorption of high amplitude acoustic oscillations. This phenomenon can be observed near sound emitters, or in the standing waves within a Kundt's tube. Acoustic streaming would result in enhancement of convection near the heater surface thereby enhancing boiling. Hence it is necessary to study the streaming characteristics of the acoustic field generated by the transducer.

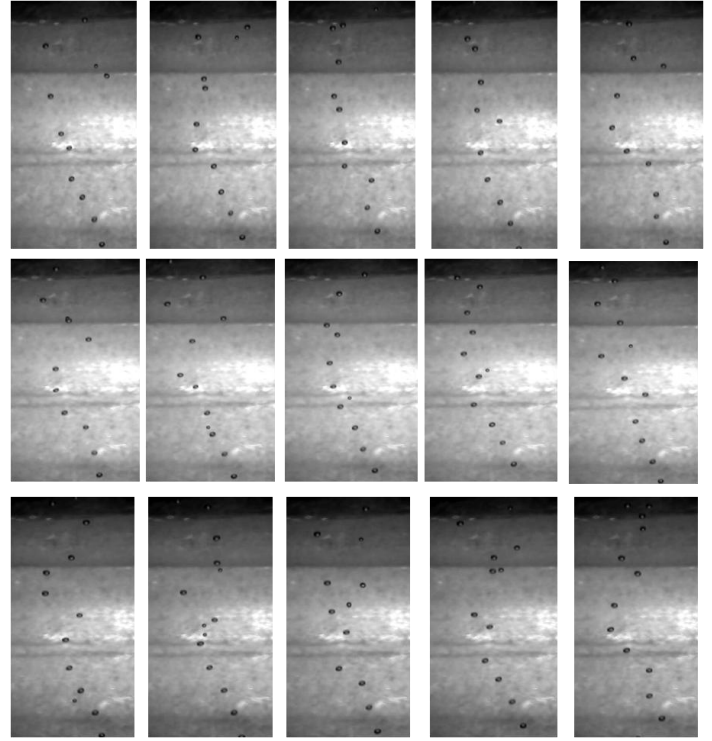


Figure 10: Visualization of absence of Acoustic streaming visualization with low bubble density (i) Row 1: No acoustic field (ii) Row 2: 47 kHz acoustic field (iii) Row 3: 140 kHz acoustic field

In order to study the extent of streaming, bubbles are generated at the base of a tank by using a porous structure found typically in aquariums. The air was blown into the structure by aquarium air pump, which has limited flow control. The ultrasonic transducer was introduced from the top of the tank and the acoustic field is set in the tank. The bubble motion was captured in the presence of acoustic field and compared with that in the absence of it. Since acoustic streaming involves bulk motion of fluid, there will be a visible difference in the bubble motion in the presence of acoustic field if streaming is in action. The experiment is done for both low bubble density and high bubble density. It is clear from Figure 10 that there is no difference in the bubble motion. Hence it can be concluded that acoustic streaming is absent at the frequencies of interest of this work.

The following discussion explains the features of the simplified model developed to explain the trends of the results. It is seen that enhancement initiates at pressure amplitude of around 1 bar. This can be explained as follows. Consider a cavity of radius 'r', the force balance yields,

$$\Delta P = \frac{2\sigma}{r} \quad (3)$$

where ΔP is the difference between pressure inside the cavity and liquid pressure. On applying acoustic field, considering equilibrium at the lowest acoustic amplitude ($-P_a$), the above equation becomes,

$$\Delta P = \frac{2\sigma}{r} - P_a \quad (4)$$

If we assume thermal equilibrium exists at the interface, it can be concluded that the liquid around is in superheated state. The amount of superheat can be obtained from Clausius - Clapeyron equation as,

$$\frac{dP}{dT} = \frac{h_{fg}}{T_s (\vartheta_v - \vartheta_l)} \quad (5)$$

$$\text{Hence } \frac{\Delta P}{\Delta T} \approx \frac{h_{fg} \rho_v}{T_s} \quad (6)$$

$$\therefore \Delta T = \frac{T_s}{h_{fg} \rho_v} \left(\frac{2\sigma}{r} - P_a \right) \quad (7)$$

The above equation gives the minimum ΔT required to activate a nuclei of size r . It is assumed that ' r ' is of the order of roughness of the surface (R_a). The surface roughness of the heater is measured to be $R_a = 0.89 \mu m$. The available ΔT at any point is the wall superheat. It is clear that acoustic field reduces the required superheat of activation, thereby implying more nucleation sites will be activated. This explains the trend in the photographs taken close to the heater surface.

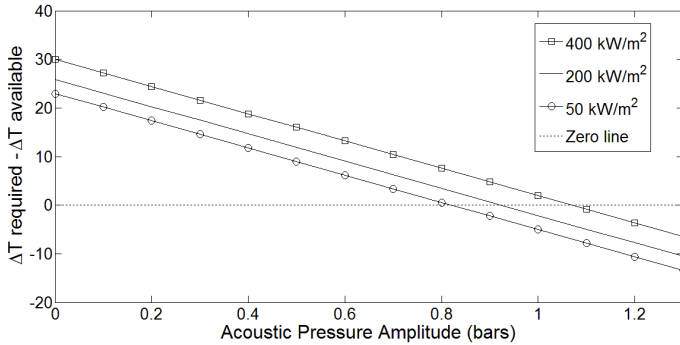


Figure 11: Superheat requirement reduction with acoustic pressure amplitude at different heat fluxes

The enhancement initiation zone can be explained from Figure 11, where the difference between required and available ΔT is plotted as a function of pressure amplitude at different heat fluxes. The required ΔT is calculated from Equation (7) and the available ΔT is calculated from Rohsenow correlation [7]. It can be assumed that once the difference is less than zero, nuclei of the size of the order of R_a will get activated. The difference goes below zero in the range 0.8 - 1 bar, which is very close to the initiation zone found in the experiments. This criterion can

be used to define critical pressure amplitude (P_c), above which sufficient ΔT is available for activation of nuclei.

It seems logical to assume that once the critical pressure amplitude is reached enhancement (E) increases with pressure amplitude.

$$i.e. \frac{dE}{dP_a} \sim (P_a - P_c), \text{ for } P_a > P_c \quad (8)$$

However one need to consider the fact that nucleation site density cannot grow indefinitely. Hence the available 'resource' for enhancement is constrained. In order to illustrate this point, consider the following calculations.

From Benjamin and Balakrishnan [9], nucleation site density (NSD) for boiling water is related to wall superheat as:

$$NSD = 218.8 P r^{1.63} \theta^{-0.4} \Delta T^3 \quad (9)$$

$$\text{where, } \theta = 14.5 - 4.5 \frac{R_a P}{\sigma} + 0.4 \left(\frac{R_a P}{\sigma} \right)^2 \quad (10)$$

On substituting the property values and using Rohsenow correlation [7], equation (9) becomes:

$$NSD = 1455.26 q \quad (11)$$

This linear variation of NSD with heat flux also offers insight as to why at pressure amplitudes more than critical pressure amplitude, enhancement varies linearly with q . At a given pressure amplitude, it is easier to activate a nucleation site at higher heat flux. Hence it is just an added effect due to increasing NSD.

In order to show the constrained available resources for enhancement, one needs to find the maximum possible nucleation site density. The maximum value of NSD can be evaluated in two ways: (i) by substituting critical heat flux (CHF) in place of q or (ii) by evaluating it geometrically. The value of CHF can be evaluated using standard correlation [10].

$$CHF = 1.26 \text{ MW/m}^2 \quad (12)$$

Using this value in equation (11), we have

$$NSD_{max,1} = 1819069 \text{ m}^{-2} \quad (13)$$

Geometrical evaluation is done as follows. The departure diameter of the bubbles is:

$$D_b = 0.0208 \beta \sqrt{\frac{\sigma}{g \rho_l}} = 1.04 \text{ mm} \quad (14)$$

If the surface area of the heater is A_s , maximum number of bubbles that can exist at the surface of the heater at any instant of time is,

$$N_{max} = \frac{4A_s}{\pi D_b^2} \quad (15)$$

$$\text{Hence } NSD_{max,2} = \frac{N_{max}}{A_s} = \frac{4}{\pi D_b^2} = 1091598 \text{ m}^{-2} \quad (16)$$

$$\therefore NSD_{max} = \min(NSD_{max,1}, NSD_{max,2}) = 1091598 \text{ m}^{-2} \quad (17)$$

From equation (11) and equation (17), it is clear that at heat fluxes of the order of 400 kW/m², close to 50% of the available nucleation sites are used even in the absence of acoustic field. Hence the restriction of NSD should be taken into account while modelling. We assume that the NSD increases linearly with pressure amplitude above the critical pressure.

$$NSD(P_a) = NSD(P_a = 0) + A(P_a - P_c), \text{ for } P_a > P_c \quad (18)$$

where the multiplier A will be a function of heat flux and frequency. Let P_e be the pressure where NSD becomes NSD_{max} , then,

$$NSD_{available}(P_a) = NSD_{max} - NSD(P_a) = A(P_e - P_a) \quad (19)$$

It is further assumed that

$$\frac{dE}{dP_a} \sim (P_a - P_c) NSD_{available}, \text{ for } P_a > P_c \text{ \& } P_a < P_e \quad (20)$$

$$\therefore \frac{dE}{dP_a} = \begin{cases} B(P_a - P_c)(P_e - P_a), & \text{for } P_a > P_c \text{ \& } P_a < P_e \\ 0, & \text{otherwise} \end{cases} \quad (21)$$

Equation (21) can be integrated to find the expression for enhancement as:

$$\therefore E = \begin{cases} B \left[P_e P_c (P_a - P_c) + \frac{(P_e - P_c)(P_a^2 - P_c^2)}{2} - \frac{(P_a^3 - P_c^3)}{3} \right] & \text{for } P_a < P_c \\ B \left[P_e P_c (P_e - P_c) + \frac{(P_e - P_c)(P_e^2 - P_c^2)}{2} - \frac{(P_e^3 - P_c^3)}{3} \right] & \text{for } P_a > P_c \text{ \& } P_a < P_e \\ B \left[P_e P_c (P_e - P_c) + \frac{(P_e - P_c)(P_e^2 - P_c^2)}{2} - \frac{(P_e^3 - P_c^3)}{3} \right] & \text{for } P_a > P_e \end{cases} \quad (22)$$

Table 1: Model variables

Variable	47 kHz		140 kHz	
P_c	1.092 bar		1.054 bar	
P_e	1.616 bar		1.572 bar	
B	Heat Flux (kW/m ²)	Value	Heat Flux (kW/m ²)	Value
	134.88	13.91	128.5	6.04
	290.79	28.47	275.6	11.15
	380.62	35.49	390.1	13.20

The above model variables are evaluated by minimising the RMS error of observations. The above table (Table 1) summarises the result. It is clear from the table that P_c and P_e are independent of frequency and P_c is very close to the value estimated using Clausius - Clapeyron equation. The linear variation of B with heat flux is shown in Figure 12.

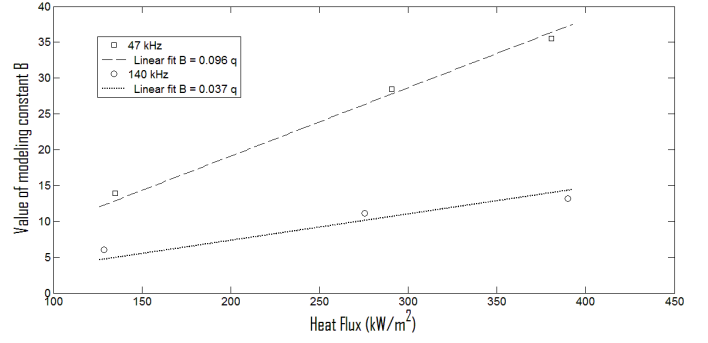


Figure 12: Variation of Modelling constant B with heat flux at two frequencies

The variation of B with frequency can be explained by considering the time scales of boiling. The departure frequency of the bubble is correlated with departure diameter as follows:

$$f = \frac{w}{\pi D_b} \left(1 + \frac{q}{\rho_v h_{fg} w} \right) \quad (23)$$

$$\text{where } w = \sqrt{\frac{D_b g}{2} + \frac{2\sigma}{D_b \rho_l g}} \quad (24)$$

Even at the highest heat flux of interest (400kW/m²), the departure frequency is about 130 Hz (from equation (23)). This means that the acoustic frequency is about three orders of magnitude bigger compared to bubble departure frequency. Hence it can be confirmed that there will be no direct interaction between time scales of boiling and acoustic field. It can also be assumed that since about 1000 acoustic pressure cycles happen, the majority of mass transfer across the interface would occur when the radius of the bubble is of the order of equilibrium radius corresponding to the pressure amplitude and frequency. It could be argued that an equilibrium radius close to departure diameter would be ideal for heat transfer as the bubble would depart easily.

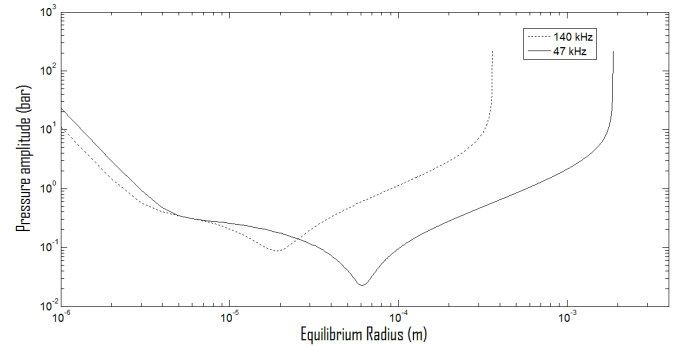


Figure 13 : Variation of equilibrium radius with pressure amplitude at 47 kHz and 140 kHz

The variation of equilibrium radius is calculated from Y. Hao and A. Prosperetti [11] and is plotted in Figure 13. The radius to the left of the minima in the curve is an unstable one and hence the values to the right of minima are considered for explanation. The second equilibrium radius (R_e) for 47 kHz is about 0.6 mm at 1 bar, which is close to departure radius (~0.5

mm). However the equilibrium radius is about 0.1 mm at 140 kHz. These values would explain why enhancement is frequency dependent. However the change in B cannot be correlated with R_e/D_b since data at only two frequencies are available.

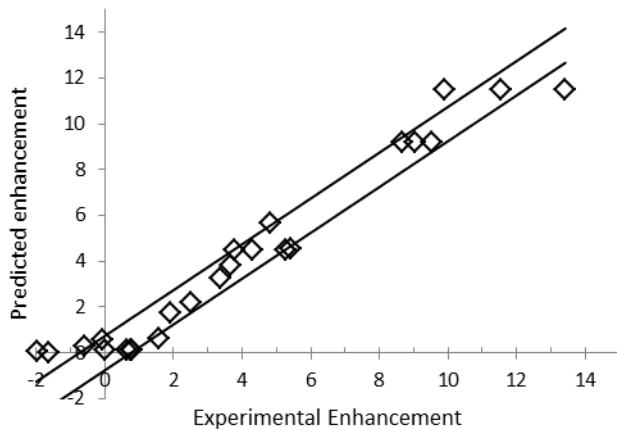


Figure 14: Comparison of experimental data and predicted data

Figure 14 compares the experimental data and the model data after critical pressure. The two lines are the experimental uncertainty limits. It is clear that the simple model is a very good approximation of the trends observed. However this model cannot explain the deterioration observed before the critical pressure amplitude.

4. CONCLUSION

This paper has investigated the effect of acoustic field on saturated nucleate boiling of water. Unlike previous works, we have systematically studied the influence of pressure amplitude and frequency and brought out the relevant trends within the scope of our studies. We have observed regimes in which acoustic field has very little influence (low amplitude, low heat flux), has a deteriorating influence (moderate pressure amplitude, low heat flux) and also where boiling is enhanced (high pressure amplitude, high heat flux). Hence it can be argued that the mixed observations regarding the effect of acoustic field on boiling in literature is primarily due to the different regimes in which the experiments are conducted by various research groups. It is also clear that the results needs to be classified based on pressure amplitude, frequency and heat flux. This was missing in all previous works. We have also revealed a possible mechanism by which the results can be explained and modelled the phenomenon using this hypothesis with empirical constants. The model fits very well with the experimental data proving the validity of our hypothesis. As an extension of this work, it is necessary to study the effect over a wider range of frequencies and at higher heat flux. In addition to nucleate boiling, the effect on critical heat flux can also be investigated systematically.

REFERENCES

- 1 Wang, C. H. and V. K. Dhir (1993). "On the Gas Entrapment and Nucleation Site Density during Pool Boiling of Saturated

Water." *Journal of Heat Transfer, Transactions ASME* 115(3): 670-679.

- 2 Isakoff, S. E., 1956. Effect of an Ultrasonic Field on Boiling Heat Transfer - Exploratory Investigation. Stanford, CA, Heat Transfer and Fluid Mechanics Institute. Stanford University Press, pp 15-28.
- 3 Wong, S.W. and Chon, W.Y., 1969. Effects of Ultrasonic Vibrations on Heat Transfer to Liquids by Natural Convection and by Boiling, *AIChE J.* vol. 15, pp. 281-288.
- 4 Park, K. A. and Bergles, A. E., 1988. "Ultrasonic Enhancement of Saturated and Subcooled Pool Boiling." *International Journal of Heat and Mass Transfer* 31(3), pp 664-667.
- 5 Kim, H-Y, Kim, Y. G., and Kang. B.H., 2004. "Enhancement of Natural Convection and Pool Boiling Heat Transfer via Ultrasonic Vibration." *International Journal of Heat and Mass Transfer* 47, vol(12-13), pp 2831-2840.
- 6 Zhou, D.W., Liu, D.Y., Hu, X.G. and Ma, C.F., 2002. Effect of acoustic cavitation on boiling heat transfer, *Experimental Thermal and Fluid Science*, vol. 26(8), pp 931-938.
- 7 Rohsenow W.M, (1952). A method of correlating heat transfer data for surface boiling liquids, *Trans. ASME* 74: 969-979.
- 8 Kenning, D. B. R., (1999). IMechE Conference Transactions 6th UK National Heat Transfer Conference, Edinburgh 15-16 September 1999.143-167
- 9 Benjamin R. J., A. R. Balakrishnan, (1997). Nucleation Site Density in Pool Boiling of saturated pure liquids. *Experimental thermal and fluid sciences*.15:32-42
- 10 Lienhard J.H, Dhir V.K, Riherd D.M (1973), Peak pool boiling heat flux measurements on finite horizontal flat plates, *J. Heat Transfer*, 95, 477
- 11 Hao. Y and A. Prosperetti (1999) 'The dynamics of vapor bubbles in acoustic pressure fields', *Physics of Fluids*, 11(8),

Thermodynamic Effects on Subcooled Liquid Oxygen Cavitaing Flow

Mamoru Oike*

Ishinomaki Senshu University

1 Shinmito, Minamisakai, Ishinomaki

Miyagi 986-8580, Japan

Tetu Goto

Ishinomaki Senshu University

1 Shinmito, Minamisakai, Ishinomaki

Miyagi 986-8580, Japan

Masataka Kikuchi

Japan Aerospace Exploration Agency

1 Koganesawa, Kimikaya, Kakuda

Miyagi 981-1525, Japan

Satoshi Takada

Japan Aerospace Exploration Agency

1 Koganesawa, Kimikaya, Kakuda

Miyagi 981-1525, Japan

Makoto Yoshida

Japan Aerospace Exploration Agency

1 Koganesawa, Kimikaya, Kakuda

Miyagi 981-1525, Japan

* E-mail: oike@isenshu-u.ac.jp

ABSTRACT

An experimental investigation of cavitating flows passing through an orifice was carried out in order to clarify the characteristics of cavitation in subcooled liquid oxygen. Comparison between influences of the orifice diameter, d_o , and the pressurized gas, which pressurized the liquid oxygen in the tank to supply it to the test section, based on the thermodynamic parameter Σ^* , showed that Stepanoff's factor B (dimensionless temperature depression) in the downstream of the orifice depends strongly on the pressurized gas (O_2 , N_2 and He) as well as the orifice diameter. In order to clarify the thermodynamic effect on cavitation, the void fraction, α_o , at the orifice outlet was estimated from the speed of sound in the two-phase flow calculated by the equation proposed by Brennen, and the other void fraction, α_2 , in the downstream of the orifice was obtained from the Stepanoff's factor B based on the experimental results and the visual images. It was confirmed that the ratio of α_2 to α_o monotonically decreases with increasing thermodynamic parameter Σ^* in the subcooled liquid oxygen cavitating flow. Therefore, the thermodynamic effects of cavitation can be considered to be effective even in subcooled liquid oxygen cavitating flow.

NOMENCLATURE

T : temperature [K]

P : pressure [MPa]

P_f : pressure fluctuation [MPa]

Q : volumetric flow rate [m^3/s]

C_d : orifice discharge coefficient

B : Stepanoff's factor

U_{th} : flow velocity at the orifice throat [m/s]

L : evaporative latent heat [kJ/kg]

C_p : specific heat at constant pressure [kJ/kg]

c : speed of sound [m/s]

d_o : orifice diameter [m]

f, g : thermodynamic parameter

h : enthalpy [kJ/kg]

Σ^* : dimensionless thermodynamic parameter

α : void fraction

α_L : thermal diffusivity [m^2/s]

ε : volumetric ratio of thermal layer

ρ : density [kg/m^3]

σ : cavitation number

[Subscript]

L : liquid

V : Vapor

S : adiabatic process

E : isothermal process

o : at the orifice throat

I : upstream

2 : downstream

1. INTRODUCTION

Cryogenic rocket propellants such as liquid hydrogen and liquid oxygen can be easily densified by subcooling, i.e., a reduction in fluid temperature below the normal boiling point. For example, the density of liquid hydrogen increases by 7% to 76 kg/m³ as the temperature is reduced from 20 K (normal boiling point) to 15 K. A reduction of the total weight of a reusable rocket system by densification of the rocket propellants has been estimated to be 17% [1].

However, cavitation in densified propellants can vary greatly from that in normal propellants because of the strong dependence of thermophysical properties on the fluid temperature, which can cause various problems in the propellant supply system of the rocket. For example, the degree of the thermodynamic effects is reduced. Therefore, once cavitation occurs, it grows dramatically and the instabilities are amplified. Furthermore, the speed of sound in bubbly flow drastically decreases with the occurrence of cavitation. Thus, when cavitation occurs in a flow through a throat, the flow easily chokes there, resulting in the generation and amplification of oscillations [2]. Although many researches [3] on the development of densification systems of rocket propellants have been carried out, characteristics on cavitation in densified rocket propellants have not yet been clarified.

An experimental investigation of cavitating flows passing through an orifice nozzle was carried out in order to clarify the characteristics of cavitation in subcooled liquid oxygen. Comparison between influences of the orifice diameter, d_o , and the pressurize gas, which pressurized the liquid oxygen in the tank to supply it to the test section, based on the thermodynamic parameter Σ^* [4-5], showed that the Stepanoff's factor B [6] (dimensionless temperature depression) in the downstream of the orifice depends strongly on the pressurize gas (O_2 , N_2 and He) as well as the orifice diameter. In order to clarify the thermodynamic effect on cavitation, the void fraction, α_o , at the orifice outlet was estimated from the speed of sound in the oxygen bubbly flow calculated by the equation proposed by Brennen [7], and the other void fraction, α_2 , in the downstream of the orifice was obtained from Stepanoff's factor B based on the experimental results and the visual images. It was confirmed that the ratio of void fraction α_2/α_o monotonically decreases with increasing thermodynamic parameter Σ^* in the subcooled liquid oxygen cavitating flow.

2. EXPERIMENTAL PROCEDURE

Figure 1 shows a schematic diagram of the experimental apparatus which consists of a liquid oxygen run tank, a liquid nitrogen run tank, a heat-exchanger, a test section and a vent line to the atmosphere. The pressure of liquid oxygen in the run tank was controlled by a gas regulator with external gas. Pressurized liquid oxygen was cooled by liquid nitrogen through the heat-exchanger, and was supplied to the test section. The flow rate was controlled by the pressure in the run tank. When liquid oxygen flowed from the run tank to the atmosphere, cavitation was occurred at the orifice throat in the test section.

The fluid temperature, pressure and pressure fluctuation were measured a 125-mm upstream and a 37-mm downstream of the orifice, respectively. The volumetric flow rate was measured upstream of the orifice. These measured values were

recorded by the digital acquisition system. Table 1 shows the experimental conditions. Three different orifice diameters, d_o , and three different pressurize gas, O_2 , N_2 , He, were used to examine their influences on subcooled liquid oxygen cavitating flows.

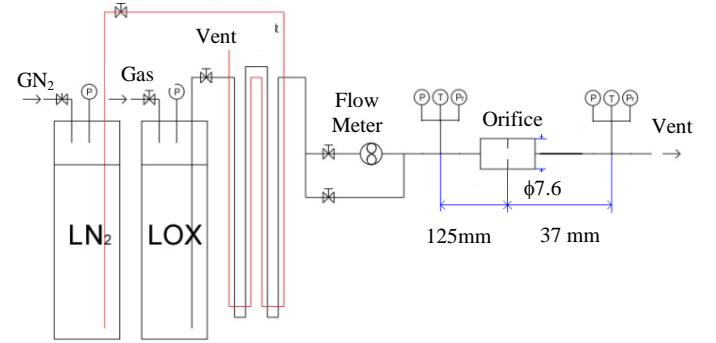


Fig. 1 Schematic diagram of the experimental apparatus

Table 1 Flow experiment conditions

Orifice diameter, d_o [mm]	1.8, 2.2, 3.4
Orifice length, L_o [mm]	1.5
Orifice area ratio	0.056 – 0.200
Pressurize gas	O_2 , N_2 , He
Upstream temperature T_1 [K]	86 – 106
Pressure difference, ΔP_o [MPa]	0.2 – 1.3

The discharge coefficients, C_d , and Stepanoff's factor B were obtained for various values of the cavitation number, σ , and the dimensionless thermodynamic parameter, Σ^* , in order to investigate the influences of the orifice diameter and the pressurize gas. These values are defined by following equations,

$$\sigma = \frac{P_1 - P_v}{P_1 - P_2} \quad (1)$$

$$\Sigma^* = \frac{L^2}{C_{p,L} T_1 \sqrt{\alpha_L}} \left(\frac{\rho_v}{\rho_L} \right)^2 \sqrt{\frac{d_o}{U_{th}^3}} \quad (2)$$

$$C_d = U_{th} \sqrt{\frac{\rho_L}{2\Delta P_o}} = \frac{4Q}{\pi d_o^2} \sqrt{\frac{\rho_L}{2(P_1 - P_2)}} \quad (3)$$

$$B = \frac{\alpha}{1 - \alpha} = \frac{\Delta T}{T^*} = (T_1 - T_2) \frac{\rho_L C_{p,L}}{\rho_v L} \quad (4)$$

Assuming a quasi-static process, the void fraction, α , in the downstream of the orifice can be obtained from Stepanoff's factor B by using Eq. (4). However, there was considered to be relatively high-speed flow condition in the downstream of the orifice during the experiment. Therefore, visualization experiments were conducted to confirm the value of α evaluated from Stepanoff's factor B . The visualization test section shown in Fig. 2 instead of the test section was installed in the experimental apparatus. The fluid temperature was measured a 50-mm upstream and a 25-mm downstream of the orifice, respectively. The photographs were pictured at 15,000 frames per second. The orifice and cavitation which occurred there were

illuminated by backlighting. The experimental conditions are summarized in Table 2.

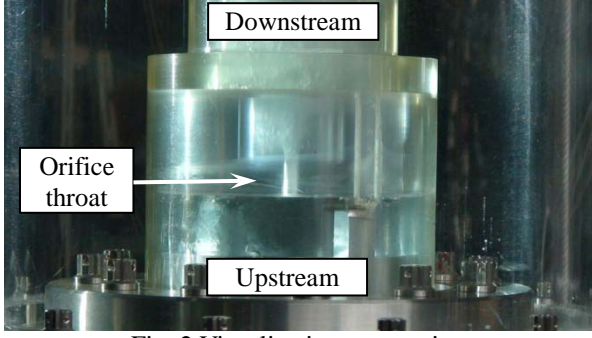


Fig. 2 Visualization test section

Table 2 Visualization experiment conditions

Orifice diameter, d_o [mm]	3.0
Orifice length, L_o [mm]	10
Inlet, outlet orifice area ratio	0.002, 0.040
Pressurize gas	O ₂ , He
Upstream temperature T_1 [K]	88 – 110
Pressure difference, ΔP_o [MPa]	0.15 – 0.80

3. EXPERIMENTAL RESULTS

3.1 Flow experiment

Figure 3 shows the relationship between the cavitation number σ and Stepanoff's factor B obtained for $d_o=1.8$ mm and the pressurize gas of N₂. According to Eq. (4), the factor B represents a mass ratio of vapor phase to liquid phase at which the downstream temperature, T_2 , was measured. When the upstream temperature of liquid oxygen, T_1 , decreased for constant upstream pressure, P_1 , the ratio of vapor phase in a 37-mm downstream of the orifice decreased rapidly. In the subcooled condition, the vapor phase ratio was initially increased by increasing P_1 . After closing the gas regulator of the liquid oxygen run tank, the cavitation number σ increased with decreasing P_1 , and consequently the factor B became smaller. When the cavitation number became larger than 1.05, the factor B was completely a minus value, which indicates that T_2 became higher than T_1 . Therefore, the minus value of the factor B is considered to be that the temperature depression due to the evaporation latent heat was compensated with the condensation latent heat due to the collapse of the cavity bubbles.

In the subcooled condition the value of T_2 rapidly decreased by a few K, and kept constant temperature for a several minutes then T_2 gradually increased. In the below we focus on the duration when T_2 kept constant temperature in the subcooled condition, in order to clarify the influences of the orifice diameter and the pressurize gas on subcooled liquid oxygen cavitating flow. In this situation the cavitation number was about 1.0 independent of the experimental condition.

Figure 4 shows the relationship between the thermodynamic parameter Σ^* and the Stepanoff's factor B obtained for the pressurize gas of N₂. As the value of Σ^* increased with the increase of the orifice diameter, d_o , the factor B tended to decrease with the increase in d_o . Figure 5 shows the relationship between the thermodynamic parameter Σ^* and the discharge

coefficient C_d obtained for the same experiments as shown in Fig. 4. It is found that an average of C_d for each value of d_o approximate linearly increased with the increase of d_o .

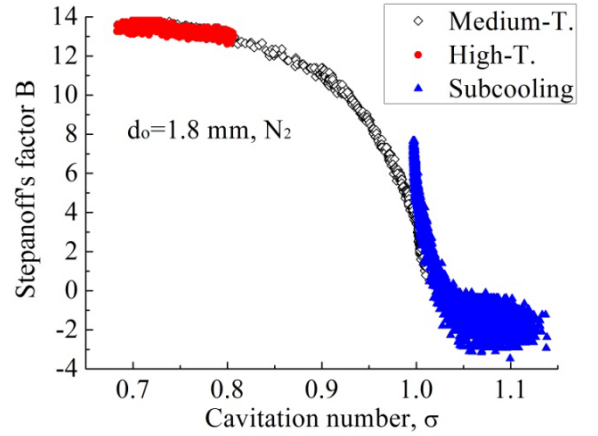


Fig. 3 The relationship between the cavitation number σ and Stepanoff's factor B obtained for $d_o=1.8$ mm and the pressurize gas of N₂.

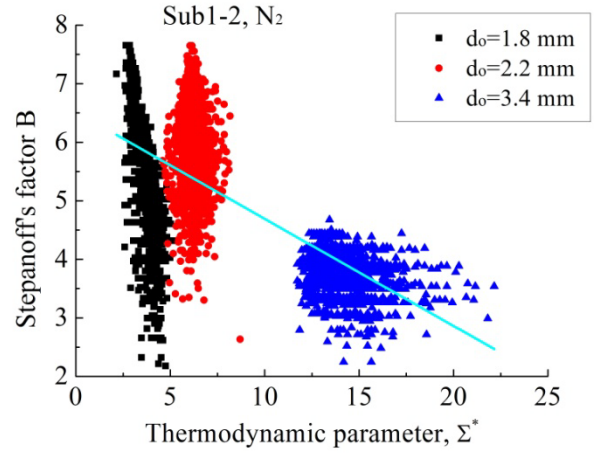


Fig. 4 Influence of the orifice diameter d_o on the Stepanoff's factor B obtained for the pressurize gas of N₂.

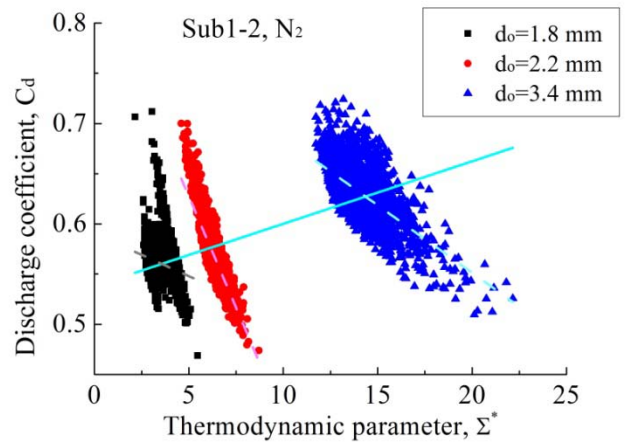


Fig. 5 Influence of the orifice diameter d_o on the discharge coefficient C_d obtained for the pressurize gas of N₂.

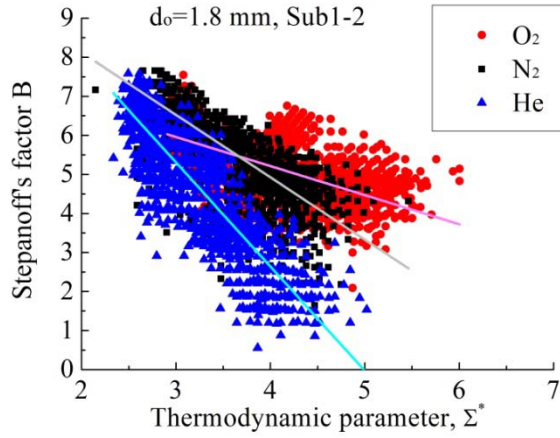


Fig. 6 Influence of the pressurize gas on the Stepanoff's factor B obtained for $d_o=1.8$ mm and the pressurize gases of O_2 , N_2 and He.

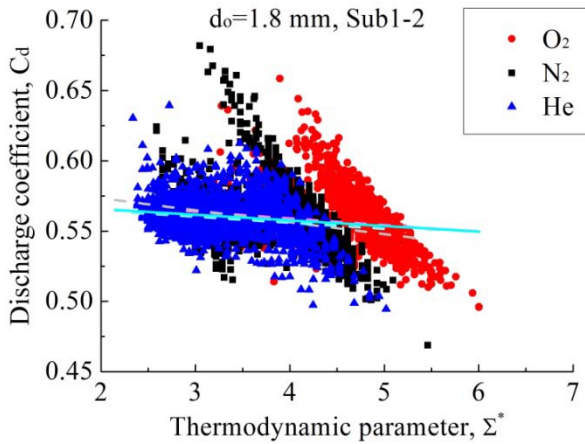


Fig. 7 Influence of the pressurize gas on the discharge coefficient C_d obtained for $d_o=1.8$ mm and the pressurize gases of O_2 , N_2 and He.

Figure 6 shows the relationship between the cavitation number σ and the Stepanoff's factor B obtained for $d_o=1.8$ mm and the pressurize gases of O_2 , N_2 and He. Comparison of the experiments for the same gas shows that the factor B decreased with increasing Σ^* . It is considered that the vapor phase ratio was suppressed by the thermodynamic effects on cavitation. Furthermore, it is found that the thermodynamic effects were influenced by the pressurize gas, and that the reduction rate for He showed the maximum value. Figure 7 shows the relationship between the thermodynamic parameter Σ^* and the discharge coefficient C_d obtained for the same experiments as shown in Fig. 6. The value of C_d slightly decreased with increase of Σ^* in spite of the three different pressurize gases. As shown in Fig 5, it is found that the value of C_d basically decreased with increase of Σ^* for each orifice diameter. Therefore, this tendency of the discharge coefficient is considered to be a fundamental feature for constant orifice diameter.

3.2 Visualization flow experiment

Figure 8 shows a typical aspect of cavitation taken at 15,000 frames per second by a high-speed video camera. A bubble cloud is shown as a black shadow jetting out the orifice throat in the picture. Figure 9 shows the relationship between the cavitation number σ and Stepanoff's factor B obtained for $d_o=3.0$ mm and the pressurize gas of O_2 . When the upstream temperature of liquid oxygen began to reduce, the factor B at a 25-mm downstream of the orifice decreased rapidly with the increase of the cavitation number. The factor B was completely a minus value when the cavitation number became larger than 1.14. Comparison between the visualization image and the value of the factor B shows that (a) the factor B was a positive quantity when the downstream temperature sensor was inside the bubble cloud, (b) the factor B was a negative quantity when the sensor was outside the bubble cloud and (c) the positive quantity of the factor B strongly depended on the darkness of the bubble cloud. From these facts it can be considered that the void fraction α estimated from the positive quantity of the factor B is compatible with the aspect of the bubble cloud in spite of the flow field.

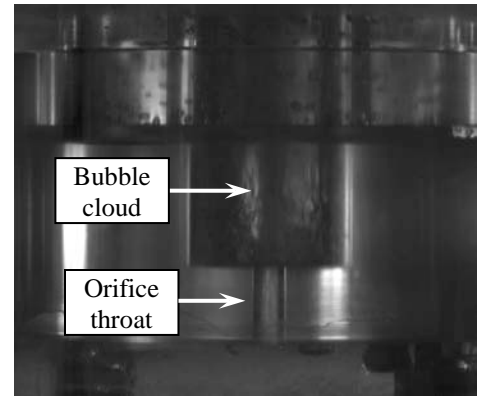


Fig. 8 Typical aspect of cavitation taken by a high-speed video camera, where the bubble cloud is shown as a black shadow.

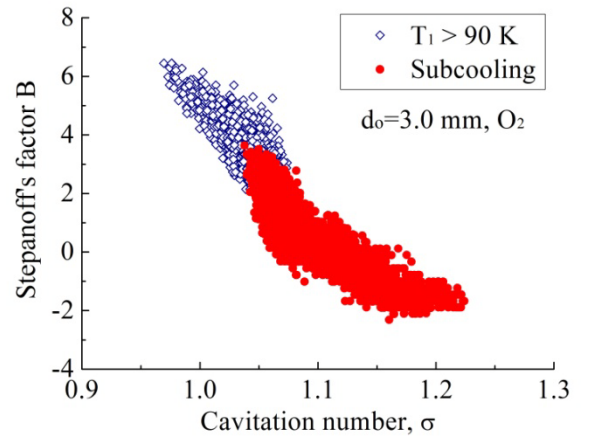


Fig. 9 The relationship between the cavitation number σ and Stepanoff's factor B obtained for $d_o=3.0$ mm and the pressurize gas of O_2 in the visualization flow experiment.

As mentioned above, we focus on the duration where T_2 kept nearly constant temperature in the subcooled condition in order to clarify the influences of the orifice diameter and the pressurize gas on the cavitating flow. The cavitation number was about 1.07 in this duration of the visualization flow experiment independent of the pressurize gas.

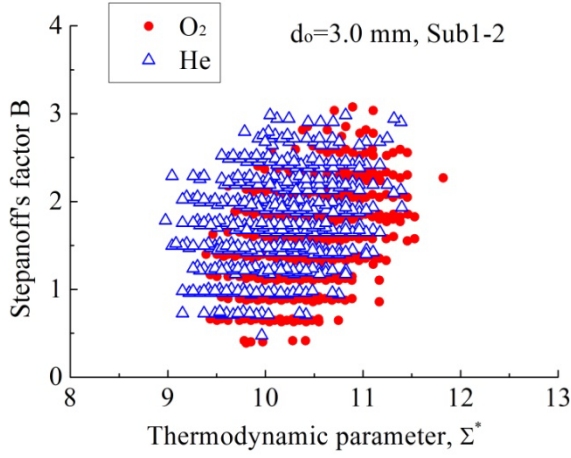


Fig. 10 Influence of the pressurize gas on the Stepanoff's factor B obtained for $d_o=1.8$ mm and the pressurize gases of O_2 and He in the visualization experiment.

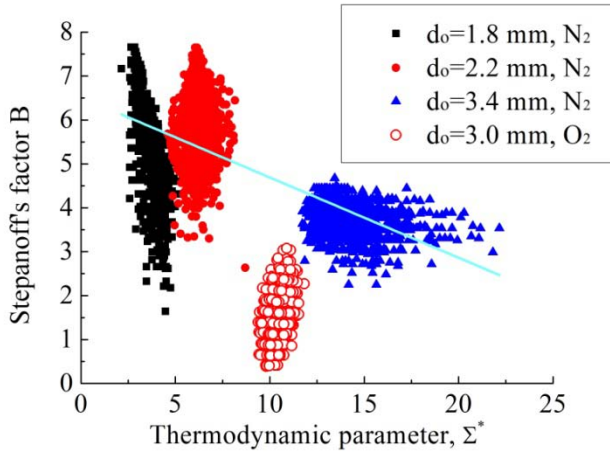


Fig. 11 Influence of the orifice diameter d_o on the Stepanoff's factor B obtained in both the flow experiments.

Figure 10 shows the relationship between the thermodynamic parameter Σ^* and the Stepanoff's factor B obtained for $d_o=3.0$ mm and the pressurize gases of O_2 and He. The influence of the pressurize gas was not as clear as that shown in Fig. 6. In order to compare exactly with the flow experiment results, the visualization experiment results obtained for the pressurize gas of O_2 are plotted in Fig. 4 and presented in Fig. 11. It is difficult to make an exact comparison between them because they were different in the orifice area ratio and the location where the downstream temperature T_2 was measured. However, Fig. 11 indicates that there is an overall tendency for the factor B to decrease with increases of the thermodynamic parameter Σ^* as the orifice diameter d_o increases.

The influence of the pressurize gas on the discharge coefficient C_d is depicted in Fig. 12. Although the difference of the pressurize gas between O_2 and He is not so clear because of the small change of the thermodynamic parameter Σ^* , it is found that the value of C_d decreased with increase of Σ^* independent of the pressurize gas. As mentioned above, this tendency of C_d is also found in the results obtained in the flow experiments shown in Figs. 5 and 7. In order to compare exactly with the flow experiments, the visualization experiment results obtained for the pressurize gas of O_2 are plotted in Fig. 5 and is presented in Fig. 13. Figure 13 indicates that the values of C_d obtained in the visualization experiments are precisely compatible with those of the flow experiments.

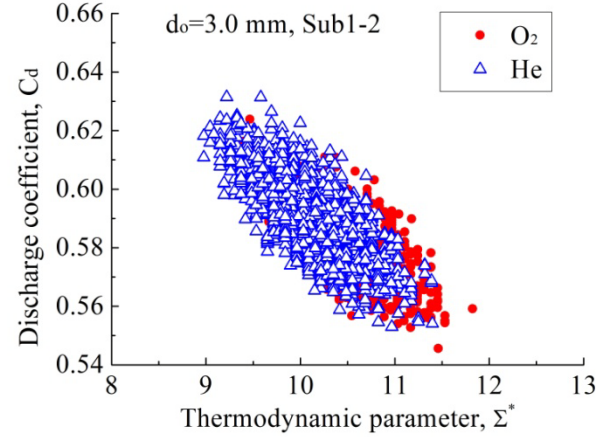


Fig. 12 Influence of the pressurize gas on the discharge coefficient C_d obtained for $d_o=3.0$ mm and the pressurize gases of O_2 and He in the visualization experiment.

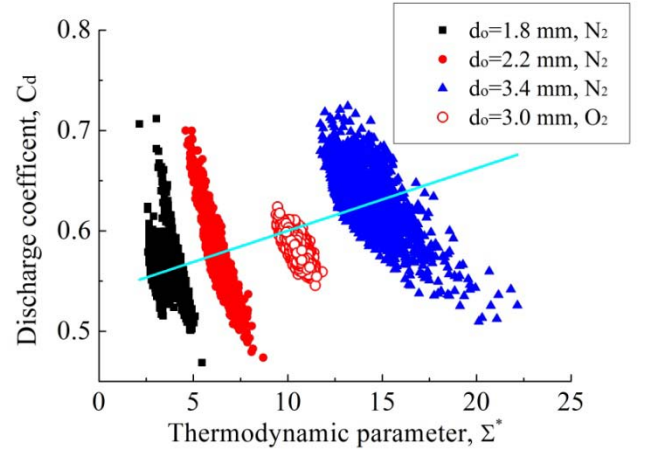


Fig. 13 Influence of the orifice diameter d_o on the discharge coefficient C_d obtained in both the flow experiments.

4. DISCUSSION

Comparison between the influences of the orifice diameter d_o and the pressurize gas (O_2 , N_2 or He) based on the thermodynamic parameter Σ^* demonstrated that the Stepanoff's factor B and the discharge coefficient C_d depend on the pressurize gas as well as the orifice diameter. Furthermore, the

results obtained in the visualization flow experiments were compatible with those of the flow experiments in spite of the large difference in the orifice configuration. Therefore, it can be considered that these results are not inherent in the experimental apparatus.

Meanwhile, the visualization experiments confirmed that the void fraction α_2 which is estimated from the positive quantity of the factor B by Eq. (4) is compatible with the aspect of the bubble cloud in spite of the flow field. Therefore, the void fraction α_2 at which the downstream temperature T_2 is measured may be obtained from the factor B based on the experimental results. The thermodynamic effects on cavitation can be explained as follows.

- (1) As cavity bubbles grow, evaporative latent heat is taken from the surrounding fluid of liquid/vapor boundary.
 - (2) The temperature of the surrounding fluid decreases and then saturated vapor pressure becomes lower.
 - (3) Development of cavity bubbles is suppressed.
- Therefore, a ratio of the void fraction in the downstream to that at the orifice outlet, α_2/α_o , is a fundamental indicator for evaluation of thermodynamic effects on cavitation in the flow passing through the orifice.

Figure 14 shows the variation of the speed of sound in relation to the void fraction at several temperatures. The speed of sound in the oxygen bubbly flow is calculated by Eq. (5) [10].

$$\frac{1}{\rho c^2} = \frac{1-\alpha}{P} \{ (1-\varepsilon_L) f_L + \varepsilon_L g_L \} + \frac{\alpha}{P} \{ (1-\varepsilon_V) f_V + \varepsilon_V g_V \}$$

$$f_L = \left(\frac{\partial \rho_L}{\partial P} \right)_s, \quad f_V = \left(\frac{\partial \rho_V}{\partial P} \right)_s$$

$$g_L = \left(\frac{\partial \rho_L}{\partial P} \right)_E + \left(\frac{\rho_L}{\rho_V} - 1 \right) \left(\frac{h_L}{L} \frac{\partial \ln h_L}{\partial \ln P} - \frac{P}{L \rho_L} \right)_E \quad (5)$$

$$g_V = \left(\frac{\partial \rho_V}{\partial P} \right)_E + \left(1 - \frac{\rho_V}{\rho_L} \right) \left(\frac{h_L}{L} \frac{\partial \ln h_L}{\partial \ln P} + \frac{\partial \ln L}{\partial \ln P} - \frac{P}{L \rho_V} \right)_E$$

As shown in Fig. 14, the speed of sound in a bubbly flow is drastically depressed by a small increase in the void fraction and reaches a minimum value at about a 28 % void fraction at any temperature in this case. The sound of speed also decreases with decreasing fluid temperature. Therefore, it can be considered that the flow easily chokes at the orifice outlet in the subcooled liquid oxygen cavitating flow. When the flow is chokes at the orifice outlet by the occurrence of cavitation, a continue equation is basically expressed by Eq. (6).

$$\rho_{1,L} Q = \{ \alpha_o \rho_V + (1-\alpha_o) \rho_L \} \frac{\pi d_o^2}{4} c_o \quad (6)$$

The speed of sound, c_o , and void fraction, α_o , at the orifice outlet can be approximately obtained from measured values of Q and T_1 by solving simultaneous equations (5) and (6). Figure 15 shows the relationship between the thermodynamic parameter Σ^* and the speed of sound c_o obtained for all experimental results. It is found that the value of c_o monotonically decreases with increasing Σ^* .

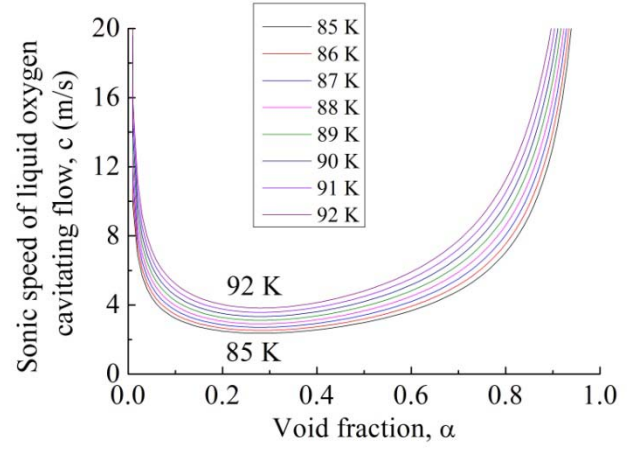


Fig. 14 Variation of the sonic speed of liquid oxygen cavitating flow in relation to the void fraction at the several temperatures.

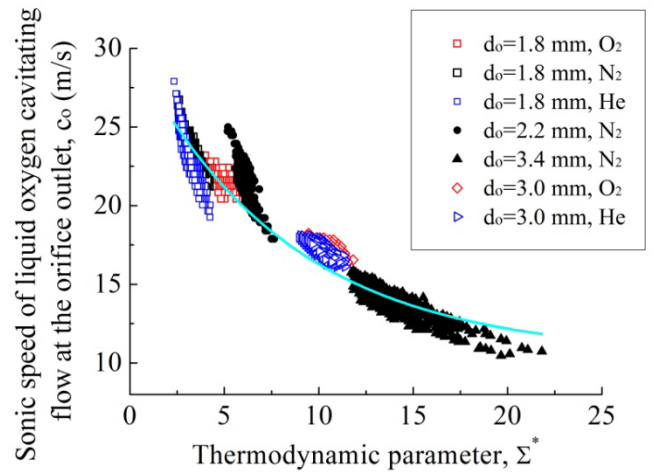


Fig. 15 The relationship between the thermodynamic parameter Σ^* and the speed of sound c_o at the orifice outlet obtained for all experimental results.

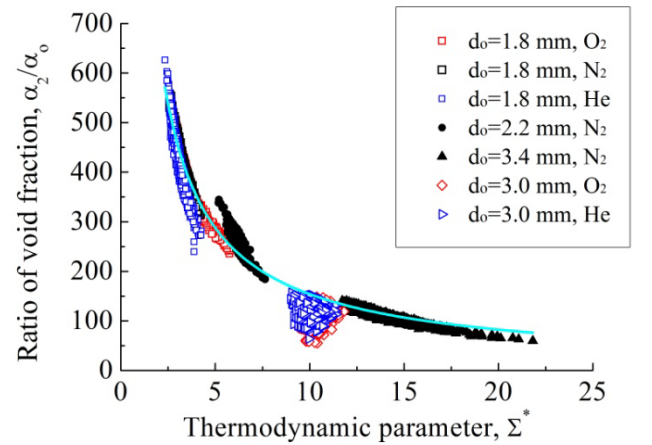


Fig. 16 Influences of the orifice diameter d_o and the pressurize gas on thermodynamic effects on cavitation in the subcooled liquid oxygen cavitating flow.

As the flow chokes at the orifice outlet, the discharge coefficient C_d and the thermodynamic parameter Σ^* are expressed as follows.

$$C_d \cong c_o \sqrt{\frac{\rho_L}{2(P_1 - P_2)}} \quad (7)$$

$$\Sigma^* = \frac{L^2}{C_{p,L} T_1 \sqrt{\alpha_L}} \left(\frac{\rho_V}{\rho_L} \right)^2 \sqrt{\frac{d_o}{c_o^3}} \quad (8)$$

These equations show that Σ^* increases with decreasing c_o and then C_d decreases with increasing Σ^* when T_1 and d_o keep constant. Therefore, the value of C_d for constant d_o can be considered to decrease with increasing Σ^* when T_1 keeps about constant, as shown in Fig. 13. Meanwhile, Fig. 13 also shows that an average of C_d for each value of d_o tends to increase with the increase of Σ^* , although the speed of sound c_o decreases with the increase of d_o as shown in Fig. 15. More detail study will be needed to explain this fact in the near future.

The ratio of void fraction, α_2/α_o , is plotted as a function of the thermodynamic parameter Σ^* in Fig. 16. Figure 16 shows that the values of α_2/α_o obtained for all experimental results monotonically decrease with increasing Σ^* . This fact demonstrates that the thermodynamic effects on cavitation are effective even in subcooled liquid oxygen cavitating flow. Furthermore, it should be note that the thermodynamic effects on cavitation are strongly suppressed even in a few K subcooled condition, which has a possibility to induce terrible flow instability.

2. CONCLUDING REMARKS

An experimental investigation of cavitating flows passing through an orifice was carried out in order to clarify the characteristics of cavitation in subcooled liquid oxygen.

Comparison between influences of the orifice diameter and the pressurized gas based on the thermodynamic parameter Σ^* , showed that the Stepanoff's factor B in the downstream of the orifice depends on the pressurize gas (O_2 , N_2 and He) as well as the orifice diameter.

The void fraction α_o at the orifice outlet was estimated from the sound speed in the oxygen bubbly flow calculated by the equation proposed by Brennen, and the other void fraction α_2 in the downstream of the orifice was obtained from the Stepanoff's factor B. It can be confirmed that the ratio of void fraction α_2/α_o monotonically decreases with increasing thermodynamic parameter Σ^* in the subcooled liquid oxygen cavitating flow. Therefore, the thermodynamic effects on cavitation can be considered to be effective even in subcooled liquid oxygen cavitating flow.

ACKNOWLEDGMENTS

This work was supported by the Japan Society for the Promotion of Science under a Grant-in-Aids for Scientific Research (C) 21560185.

REFERENCES

- [1] Lak, T., Lozano, M., and Tomisk, T., 1996, "Advancement in Cryogenic Propulsion System Performance Through Propellant Densification", ASME, SAE, and ASEE, Joint Propulsion Conference and Exhibit, 32nd, AIAA-1996-3132, Lake Buena Vista, FL, July 1-3.
- [2] Niiyama, K., Oike, M., Ohira, K., and Yoshida, Y., "Instability Phenomenon Induced by Cavitation Choke in Nozzl Flows of Subcooled Liquid Nitrogen", 2008, WIMRC FORUM 2008, Warwick University, UK, July 7-9.
- [3] Habersbusch, M. S., Stochl, R. J., and Culler, A. J., 2004, "Thermally Optimized Zero Boil-off Densified Cryogen Storage System for Space", Cryogenics, 44 (6-8), pp.485-491.
- [4] Franc, J. P., Rebattet, C., and Coulon, A., 2004, "An Experimental Investigation of Thermal Effects in a Cavitation Inducer", Trans. ASME J Fluids Eng., 126, pp.716-723.
- [5] Watanabe, S., Hideaki, T., Horiguchi, H., Furukawa, A., and Tujimoto, Y., 2007, "Steady Analysis of the Thermodynamic Effect of Partial Cavitation Using the Singularity Method", Trans. ASME J Fluids Eng., 129 (2), pp.7121-127.
- [6] Stepanoff, A. J., 1964, "Cavitation Properties of Liquids" J. Eng. Power, 80, pp.195-200.
- [7] Brennen, C.E., 1995, Cavitation and Bubble Dynamics. Oxford University Press, New York.

Acoustic Emission (AE) of single bubble inception at nozzle underwater and burst at free surface

Shuib Husin*/Universiti Kuala Lumpur

Abdulmajid Addali/Cranfield University

David Mba/Cranfield University

s.husin@cranfield.ac.uk

ABSTRACT

An experiment of the application of Acoustic Emission (AE) technology to detect and measure AE energy of a single bubble has been performed. High frequency range up to 1000 kHz is used for this particular acoustic emission investigation. A correlation between AE parameters and bubble size at inception and burst at free surface was found. The findings show the sensitivity and applicability of the AE technology, to be further explored for measurement and process monitoring in a two phase flow system. This paper discusses details of investigations into the feasibility of the passive method to size bubbles of unknown radius.

NOMENCLATURE

- ν_r = Bubble oscillation frequency
- R_o = Euilibrium bubble radius
- K = Polytrophic index of the gas inside the bubble
- P_o = Hydrostatic pressure and
- P = Density of the fluid
- V = Voltage
- R = Resistance of the system circuit

1. INTRODUCTION

The AE from bubbles' activities in a fluid at its inception when pinched off from nozzle, oscillation during rising up, and burst at free surface provides a useful method for sizing them acoustically. The application of AE technology is attempted to be explored as a new method for bubble sizing intrusive and non-intrusively. This investigation explains that the AE technology is a passive technique based on the sound scattered upon a bubble's activities which can be detected by a sensitive AE transducer. Typically, AE covers the frequency range of between 100 kHz and 1000 kHz. In this particular investigation, acoustic emission techniques detect transient acoustic waves generated by a sudden change in the local stress field in a medium [1-2] thus the magnitude of energy released is a function of bubble characteristics and the medium property.

Bubbles and cavitations are common phenomena in two-phase gas liquid and multi-phase systems in industry. Two-

phase gas-liquid flow can be seen in various applications such as industrial boilers, nuclear reactors, chemical processing plants, petro-chemical and medical applications [3]. Knowledge of bubble size and number provides monitoring of the coolant in nuclear reactors [4].

The bubble formation at the nozzle and burst at free surface are potential sources for AE. These events generate transient pressure pulses that are broadband in nature which, as expected, can be detected by an AE piezoelectric sensor. The energy of bubble collapse must be a function of bubble size and liquid properties. This manifests a method of measuring the bubble radius with the measured sound emitted by collapsing the bubble using an AE sensor of high frequency.

The techniques of photography and ultrasound have been used to determine the bubble size. However, these techniques have disadvantages such as limitation over the bubble size range (micro bubbles) and are limited only to the local size or static measurement. In addition, the analysis of photographs is quite tedious, impractical in certain cases for preparation, expensive with high speed cameras and it is arguable on accuracy. Obviously, the photography technique cannot be used in opaque conditions, e.g. metal pipe and opaque liquid such as crude oil [5]. The application of acoustic techniques to measure bubble size and detect bubble activities in a fluid system exhibit much greater results compared to the photography methods. Measurement using the acoustic technique is accurate compared to the photography method [5].

The application of acoustic technique to measure a bubble radius was scientifically started in 1933 when Minneart (1933) [6] who first investigated sound generated by air bubbles as they form at a nozzle underwater. Minneart showed that bubble oscillation frequency was associated with volume pulsation of the bubble, see Equation 1. He assumed that surface tension and viscosity terms are negligible, and that the bubble wall undergoes simple harmonic motion. For low amplitude excitation from the bubble wall when distorted where a ripple generated on its wall, then bubble oscillation is said to have

occurred. Bubble oscillation possesses a defined acoustic resonance of frequency which derived by Minneart:

$$f_0 = \frac{1}{\pi d} \sqrt{\frac{3\gamma P_0}{\rho}} \quad \text{(Equation-1)}$$

Where d is the equilibrium bubble diameter, k is the polytrophic index of the gas inside the bubble, P_0 is the hydrostatic pressure and ρ is the density of the fluid medium. To date much research is undertaken employing hydrophones to measure sound underwater or sound emitted from bubble oscillation in water [7-17].

The acoustic technique to measure cavitation of bubbles in a liquid using high frequency Acoustic Emission (AE) technology started with hydrophones and microphones, and only recently it started gaining researchers' attention by exploring the AE technology in a two phase system. In 1985, Al-Maskari [18] employed AE technology to detect cavitation in a centrifugal pump where he successfully detected developed cavitation. Later, in 1997, Neill et al., [19] performed an experiment and demonstrated that AE was capable of detecting incipient cavitation. Al-Fayez and Mba (2005) [20] confirmed that the AE technology was capable of detecting incipient cavitation in a centrifugal pump. Later study, in 2002 Yen and Lu [21] demonstrated that the AE detection system combined with artificial neural network technology successfully recognized four major flow patterns; bubbly, slug, churn and annular in an air-water vertical two-phase flow column. Very recently, Al-Lababidi et al (2009) [22] and Addali (2010) [23] successfully correlated AE with gas void fraction (GVF) in two phase gas-liquid flow and a horizontal pipeline.

In this study, the high frequency AE technology was employed to measure and detect bubble activities: formation at nozzle and burst at free surface. The application of AE technology has an advantage over other acoustic techniques in terms of robustness, simple set-up and greater signal to noise ratio (SNR). AE technology is a passive technique and could be applied using either intrusive or non-intrusive techniques. It is very sensitive and can detect the sound of a high range of frequency up to 1 MHz. Convincing results from this experiment on AE detection and measurement technique would embark the application of AE technology for bubble sizing in future research.

2. EXPERIMENT APPARATUS AND PROCEDURES

The apparatus used for AE detection for bubble inception and burst at free surface is shown in Figures 1 and 2. A water column made of 50 mm thickness aluminium filled with water. A manifold pipe was fixed to the column with the nozzle at the bottom, see Fig 1. A single bubble was produced with a controlled valve from an air compressed cylinder.

A single bubble was released at the nozzle and it has been detected by Sensors 1 and 2 where they were mounted onto the column intrusively and non-intrusively as shown in Fig 1. The

same sensor layout has been mounted onto the top of the column rig for bubble burst detection at free surface, see Fig 2; Sensor 3 has been mounted intrusively and Sensor 4 has been mounted non-intrusively. Broadband AE transducers (Physical Acoustic Corporation type Wideband Differential, WD) with an operating frequency range of 100-750 kHz and a pre-amplification of 40 dB were applied. The sampling rate for acquisition of AE waveforms was set at 2 MHz. A threshold level of 24 dB was set above the background noise of the acquisition system.

Four sizes of nozzle were used in this investigation; 1.4, 2.8, 5.6 and 8.4 mm internal hole- diameter. It was assumed that the bubble created using these nozzles is equivalent to the nozzle internal hole-diameter.

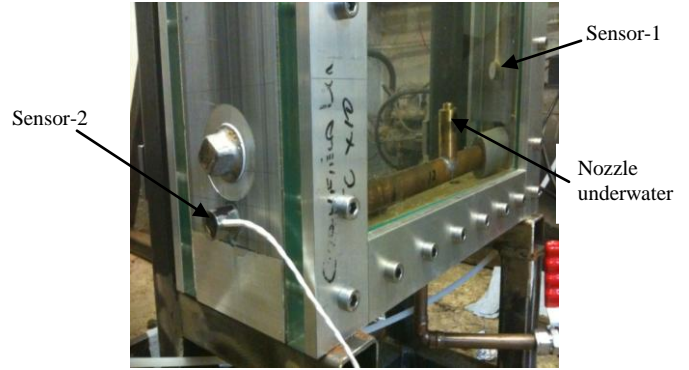


Fig 1: Apparatus layout for acoustic bubble inception detection

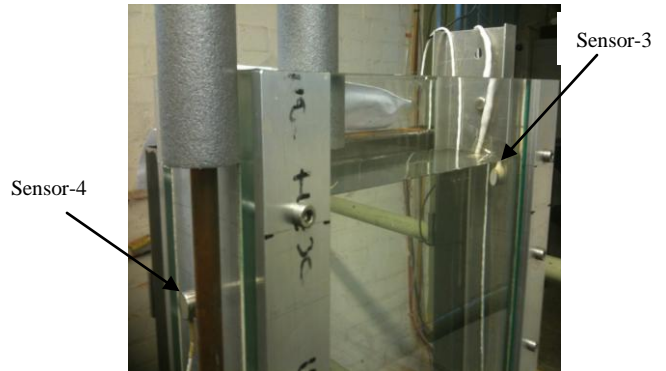


Fig 2: Apparatus layout for acoustic bubble burst detection at free surface

AE energy was determined by calculating the area within the AE burst duration at the waveform and dividing by the reference resistance (10 k-ohm). The AE burst duration at waveform had been determined before the calculation of AE energy; it is obtained by the determination of the duration from the point at which the AE response was higher than the underlying threshold level to the point at which it returned to the underlying threshold level (see Figure 3). The threshold set for this calculation procedure was 0.6103 mV. Figure 3 illustrates the method of the determination of the AE duration which was used later on for the AE energy calculation. The formula for AE energy is shown in Equation-2; it is the electrical energy (U) present in a transient event; V is volts and R is resistance of the system circuit. It is the true energy of the AE hit. The energy

was calculated using the trapezoidal numerical integration with Matlab.

$$U = \frac{1}{R} \int_0^{\alpha} V^2(t) dt \quad (\text{Eq-2})$$

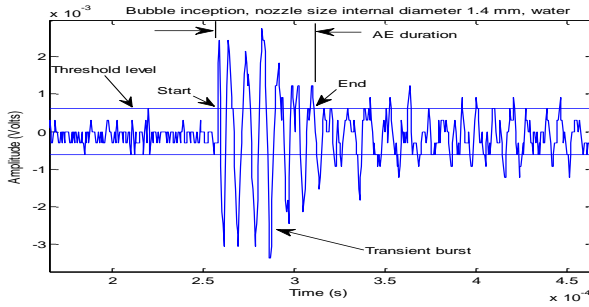


Fig 3: Methodology used for determination of AE duration at the waveform

3. EXPERIMENT RESULTS AND DISCUSSION

3.1 Signals detected from bubble inception and burst

The waveform from the data captured by an AE sensors upon bubble inception and burst are presented in Figure 4 (intrusive method- bubble inception), Figure 6 (non-intrusive method- bubble inception) and Figure 8 (intrusive method- bubble burst). Both intrusive and non-intrusive sensors detected the signal from bubble inception. However, Sensor 4 which was non-intrusively mounted at the top of column did not detect any signal from bubble burst at free surface. This might be affected by the signal strength released from bubble burst and the effect of column's wall thickness.

The amplitude of the waveform from each activity was found to increase with the rise of bubble/nozzle size. Spectrogram analysis using Matlab was performed to see the signal intensity. It was found that the signal intensity was higher at the start of event. Fig 5, 7 and 9 show the results of average FFT from 10 test samples for each size. This frequency domain analysis show that primary (main) frequency of bubble inception and burst event is at 120 kHz. Peak amplitude at main frequency components can be used as a method to bubble sizing.

The findings from this experimental investigation indicate the potential of AE technology to be used as a non-intrusive tool for bubble sizing once calibration using consideration of type of material, thickness and distance from AE source has been established. On-set monitoring using AE technology can be performed by looking at the AE amplitude of bubble activities; inception and burst. Beside FFT analysis (frequency spectrum), the amplitude versus time plot, fig (a) in Figs 4, 6 and 8 can be used as a guide for bubble sizing. This is because AE amplitude is the best indicator for bubble detection and it can be obtained on-line from the AE system.

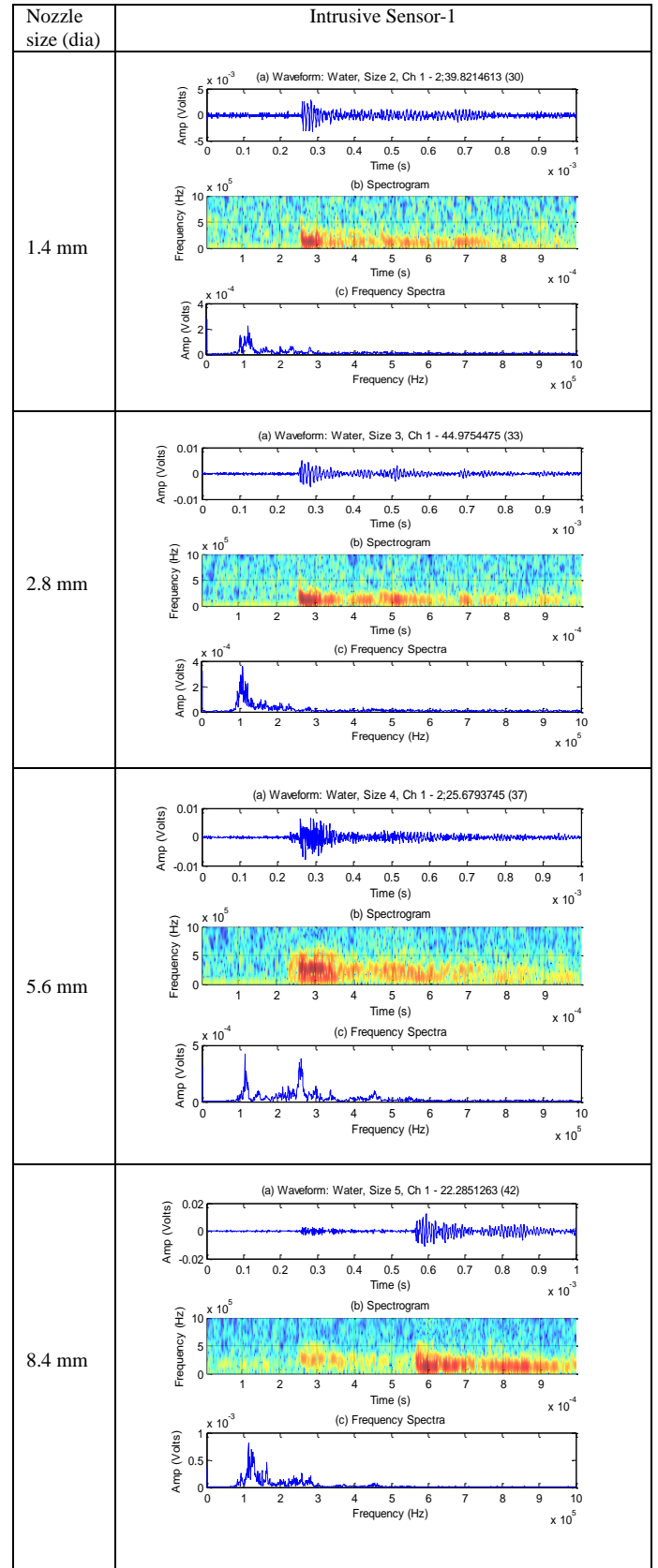


Figure 4: Plots of analysis of waveform data from bubble inception acquired by intrusive Sensor-1

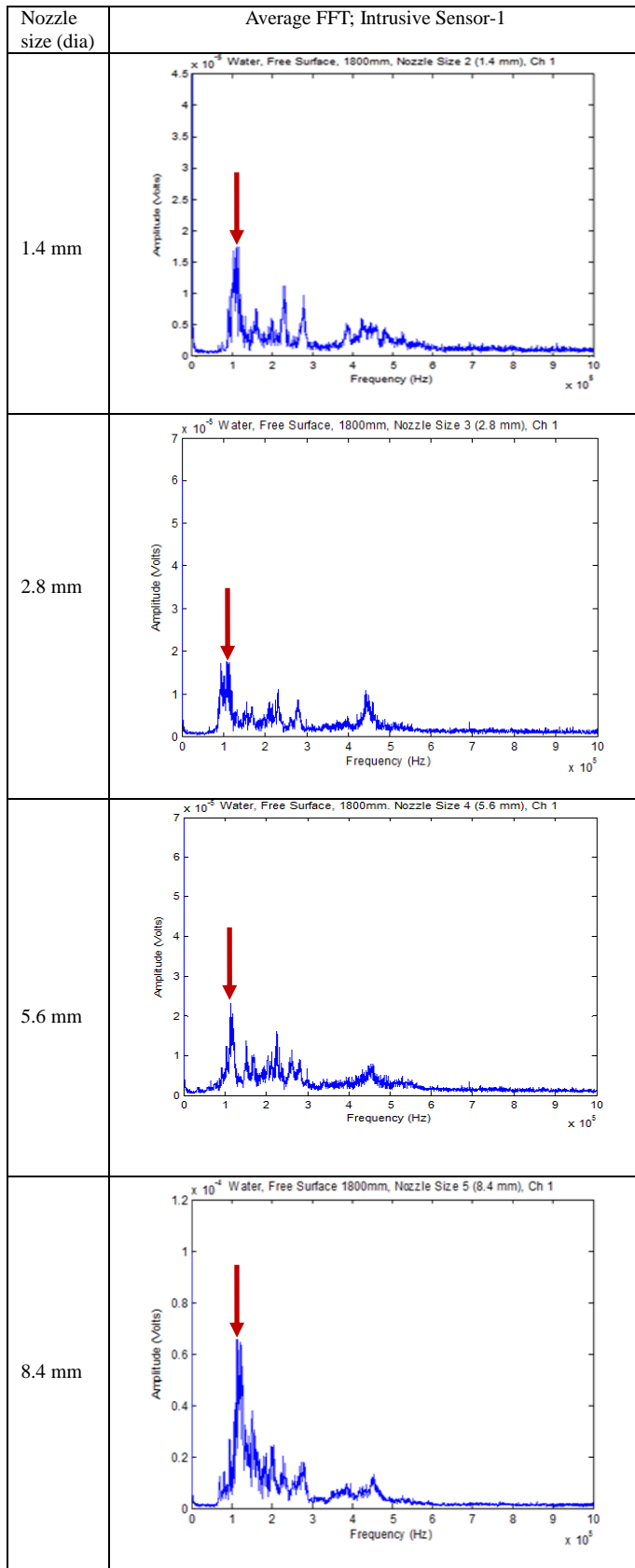


Figure 5: Average FFT from bubble inception acquired by intrusive Sensor-1

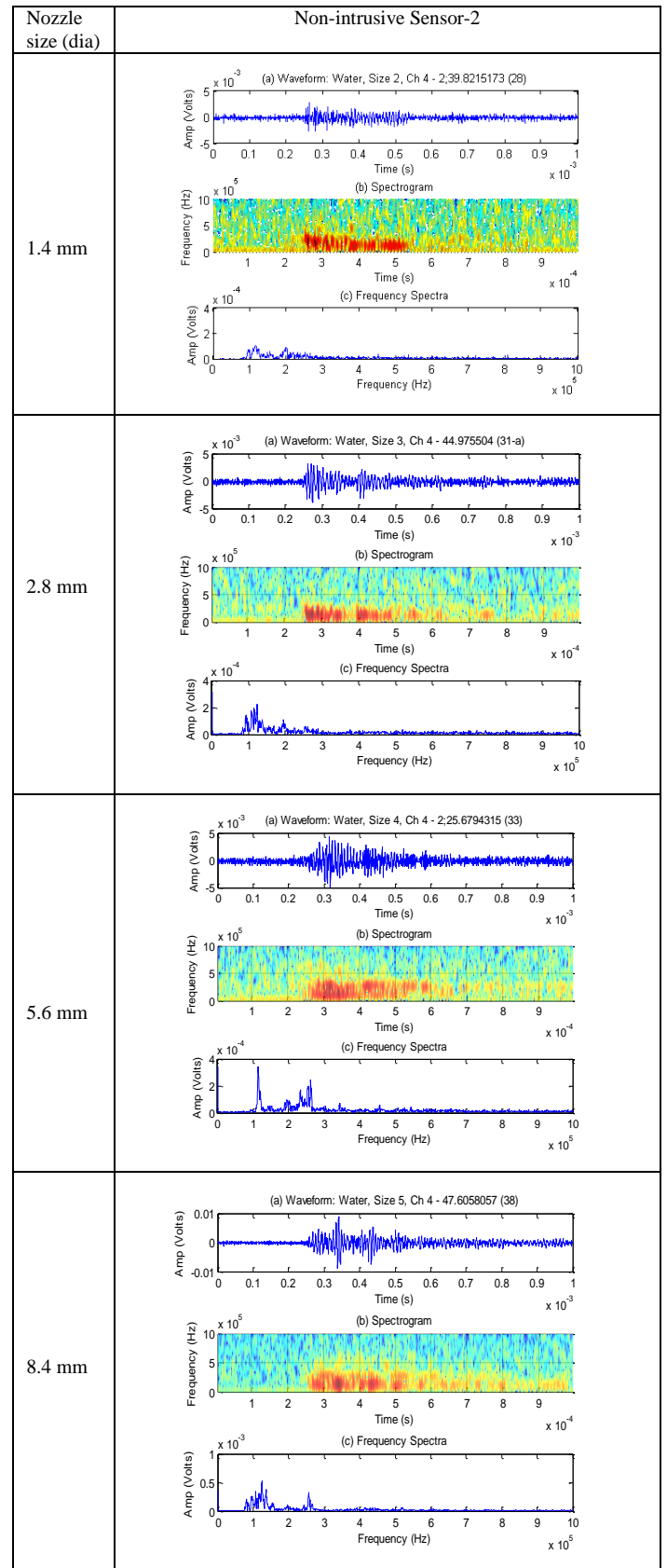


Figure 6: Plots of analysis of waveform data from bubble inception acquired by non-intrusive Sensor-2

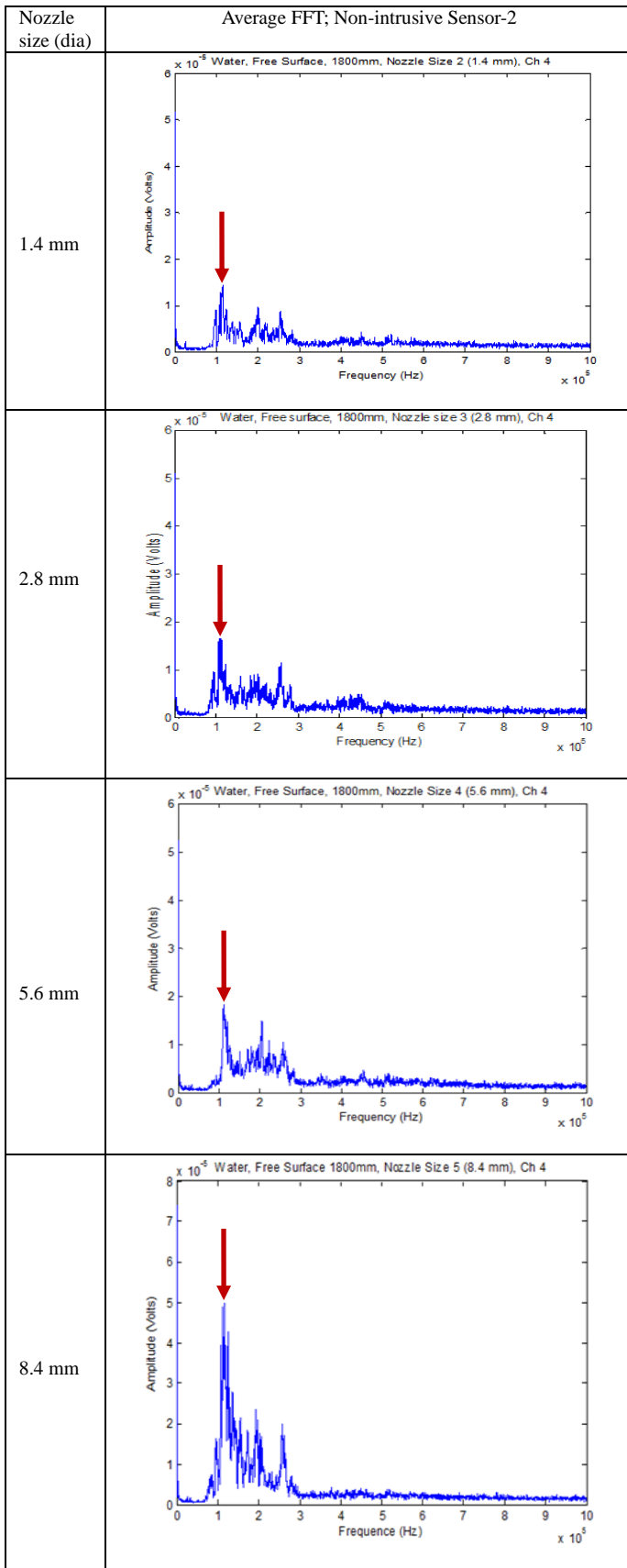


Figure 7: Average FFT from bubble inception acquired by non-intrusive Sensor-2

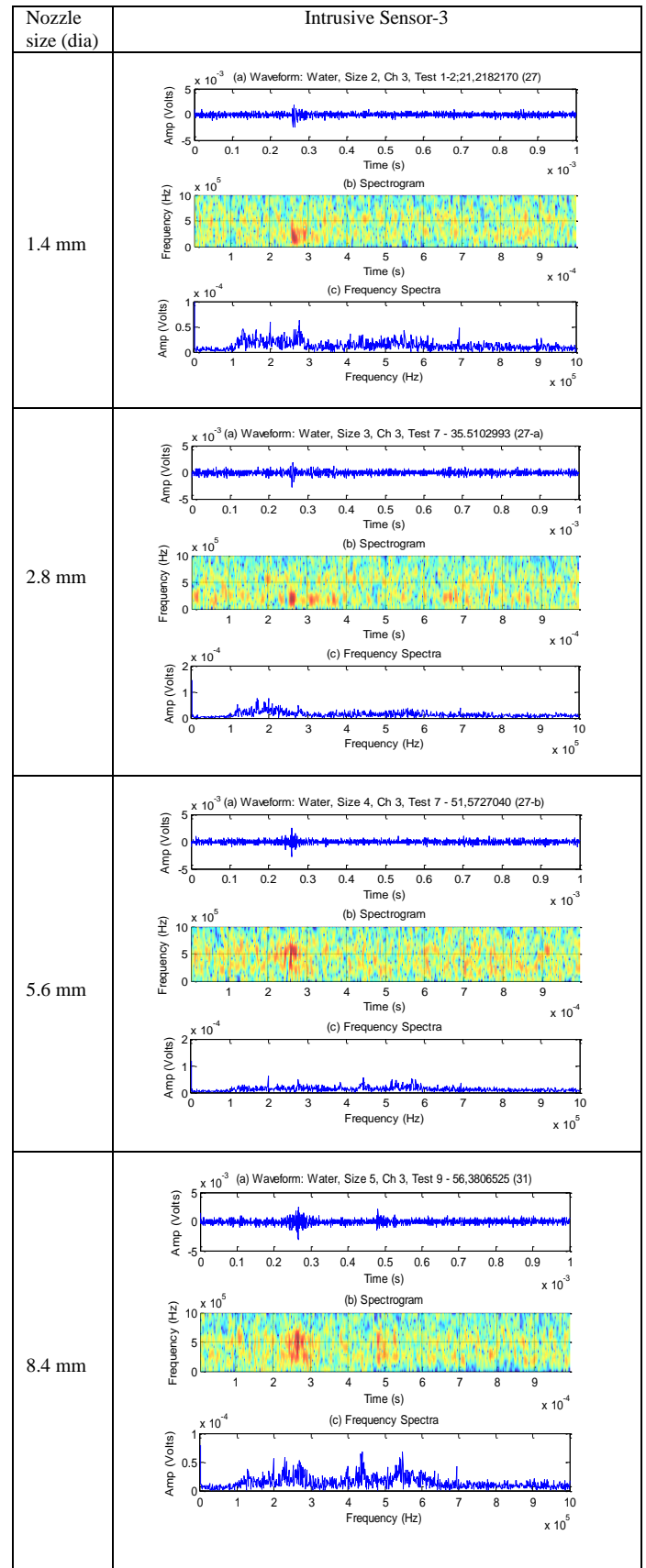


Figure 8: Plots of analysis of waveform data from bubble burst acquired by intrusive Sensor-3

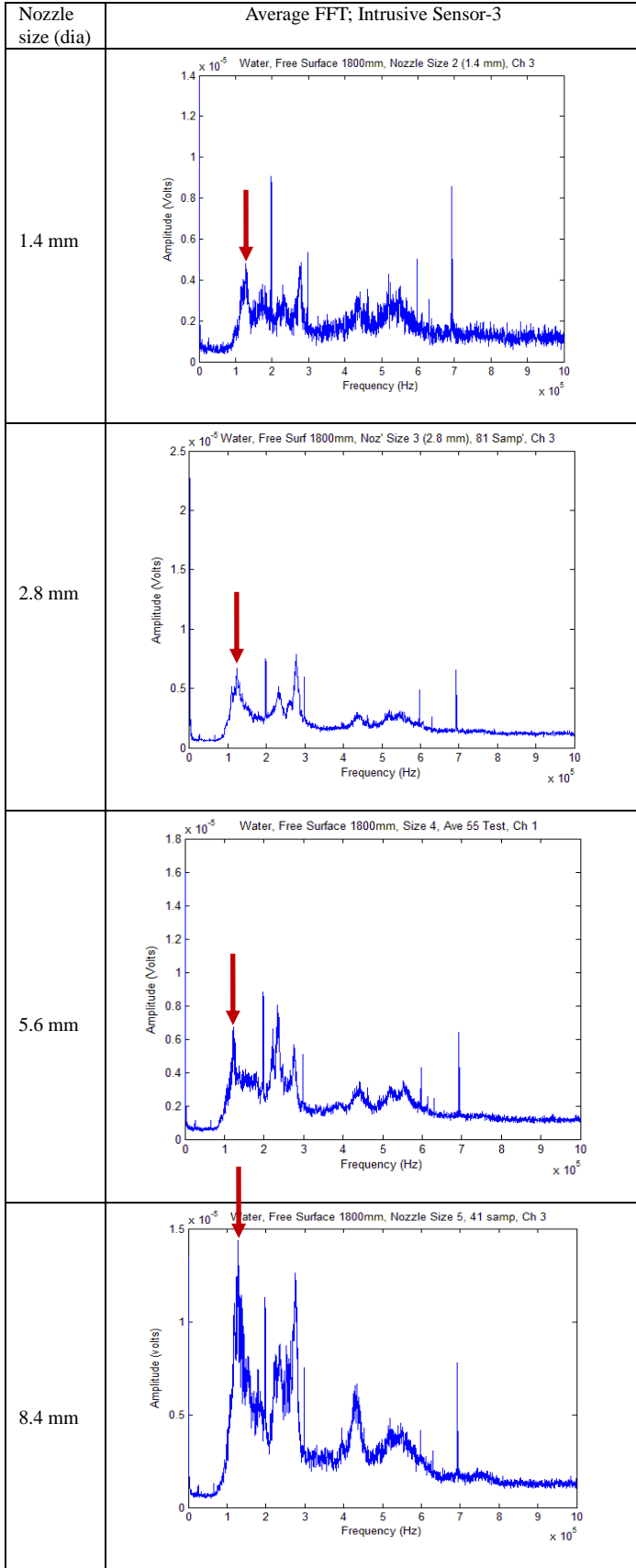


Figure 9: Average FFT from bubble burst acquired by non-intrusive Sensor-3

For bubble burst, peak amplitude increases with the increase in bubble size which mostly occurs at frequency range between 100 kHz and 300 KHz for nozzle sizes 1.4 and 2.8 mm. With increasing bubble sizes 4.8 and 5.6 mm, the peak amplitude occurs at the higher frequency range of between 400 kHz and 600 kHz.

Peak amplitude at main frequency component 120 kHz from frequency spectra (FFT plot) was chosen to differentiate bubble size. Table 1 and 2 show the peak amplitude at bubble burst at 120 kHz increases with the increase of nozzle/bubble size, for both bubble inception and burst respectively. The first two nozzle sizes 1.4 mm and 2.8 mm give only slightly difference results because the difference in bubble size generated by these two nozzles are not very different, probably because viscous and surface tension effects are relatively more important for such small nozzle diameters.

Table 1: Peak amplitude at frequency 120 kHz; Bubble inception

	Size 1.4 mm	Size 2.8 mm	Size 5.6 mm	Size 8.4 mm
Peak amp (μV): Intrusive Sensor-1	17	18	24	65
Peak amp (μV): Non-intrusive Sensor-2	15	17	18	50

Table 2: Peak amplitude of bubble burst at frequency 120 kHz at frequency spectra plot; Bubble burst

	Size 1.4 mm	Size 2.8 mm	Size 5.6 mm	Size 8.4 mm
Peak amp (μV): Intrusive Sensor-3	5	6	7	15

3.2 AE energy from bubble inception and burst

The bigger the bubble size, the higher its potential energy (E_B) released where higher sound pressure is produced when it bursts at free surface. Theoretically, the bubble energy (E_B) is proportional to its maximum volume, $E_B \propto R_{max}^3$ [24-33].

A comparison of AE energy of the bubble inception signal obtained intrusively and non-intrusively is shown in Fig 10. Empirically, the AE energy increases with the increase of bubble

size. The plot in Fig 11 indicates that the size of bubble was not equivalent with the size of nozzle internal hole-diameter. A slight increment of AE energy is shown from sizes 1.4 and 2.8 mm. Abrupt increments started from the nozzle size 5.6 indicating a big difference of bubble size generated from nozzle size 5.6 mm compared with the nozzle sizes 1.4 and 2.8 mm.

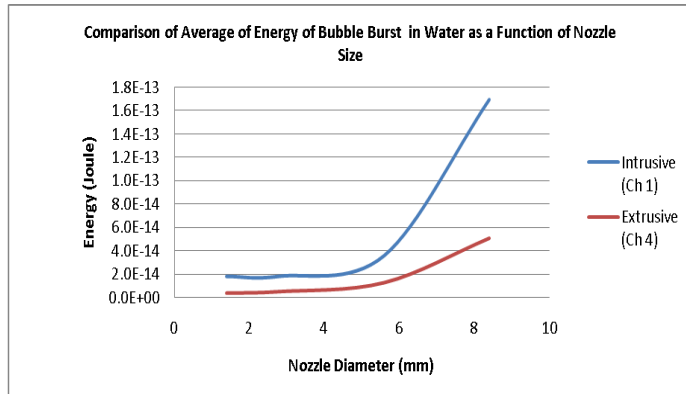


Figure 10: Plot of comparison of average of energy of bubble inception in water as a function nozzle size

AE energy of bubble burst at free surface is shown in Fig 11. Again, the nozzle sizes 1.4 and 2.8 mm show little increments of AE energy which agrees with the AE energy of bubble at inception. This confirms that the bubble size is not equivalent to the nozzle size.

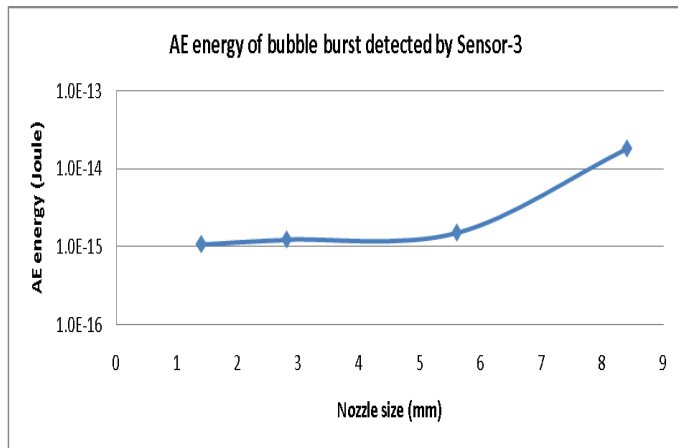


Figure 11: AE energy of bubble burst in water as a function nozzle size

4. CONCLUSION

This experiment demonstrated that AE technology is capable of capturing an AE signal from bubble activities intrusively and non-intrusively. The experimental results also demonstrated that an AE sensor was capable of detecting the AE source that comes from different media/interfaces (water and

metal). It was established that the AE amplitude and energy of bubble inception and burst increase as bubble size increases.

Through this experiment, evidence is established of the applicability of the AE technology for process monitoring on a very thick wall. It is evident that AE technology provides an effective detection and measurement of bubble size in two-phase flow systems. A correlation work of gas void fraction (GVF) from a two-phase flow in pipe also can be done with other established devices. Finally, this experiment highlights the potential for using AE to determine bubble size based on the frequency analysis of bubble activities.

ACKNOWLEDGMENTS

The authors gratefully acknowledge supports from University Kuala Lumpur, Malaysia and Cranfield University, UK.

REFERENCES

- [1] Ing, M.J., Austin, S.A., Lyons, R. (2002) "Cover Zone Properties Influencing Acoustic Emission Due to Corrosion", Cement and Concrete Research 2002.
- [2] Lyons, R., Ing, M.J., Austin, S.A., (2003) "Influence of diurnal and seasonal temperature variations on the detection of corrosion in reinforced concrete by Acoustic Emission" Corrosion Science, Volume 47, Issue 2, February 2005, Pages 413-433.
- [3] Kuwahara, T., and Yamaguchi, H., 2007. "Void fraction measurement of gas-liquid two-phase flow using magnetic fluid", Journal of Thermophysics and Heat Transfer, Vol. 21, No. 1, pp. 173.
- [4] Phelps, A.D and Leighton, T.G. "Investigations into the use of two frequency excitation to accurately determine bubble sizes" in: Blake, J.R, Boulton-Stone, J.M and Thomas, N.H. 2004. Bubble dynamics and interface phenomena, Proceedings of an IUTAM Symposium held in Birmingham, U.K., 6-9 Sept 1993, Kluwer Academic Publishers, 2004, Netherlands.
- [5] Pandit, A.B., Varley, J., Thrope, R.B., and Davidson, J.F., 1992. "Measurement of bubble size distribution: An Acoustic Technique." Chemical Engineering Science, Vol 47, No 5, p.p. 1079-1089
- [6] Minnaert, M., 1933. "On Musical Air Bubbles and the Sound of Running Water", Phil. Mag., 16, 235-248
- [7] Leighton, T.G., and Walton, A.J., 1987. "An Experimental Study of the Sound Emitted from

- Bubbles in a Liquid”, *European Journal of Physics*, 98-104.
- [8] Leighton, T.G., Fagan, K.J., Field, J.E., 1991. “Acoustic and Photographic Studies of Injected Bubbles”, *Eur. J. Phys.* 12, 77-85.
- [9] Leighton, T.G., Lingard, R.J., Walton, A.J., and Field, J.E., 1991(b) “Acoustic Bubble sizing by combining of subharmonic emissions with imaging frequency.” *Ultrasonics*, Vol. 29, p.p 319-323
- [10] Leighton, T.G., Lingard, R.J., Walton, A.J., and Field, J.E., 1993. “Bubble sizing by the nonlinear scattering of two acoustic frequencies.” *Natural Physical Sources of Underwater Sound*, Kluwer Academic Publishers, Netherlands, p.p 453-466
- [11] Leighton, T.G., Phelps, A.D., Ramble, D.G., and Sharpe, D.A., 1996. “Comparison of the Abilities of Eight Acoustic Techniques to Detect and Size a Single Bubble.” *Ultrasonics* 34, p.p 661-667
- [12] Boyd, J.W.R., and Varley, J., 2004. *Acoustic Emission Measurement of Low Velocity Plunging Jets to Monitor Bubble Size*, *Chemical Engineering Journal*, 97, 11-25.
- [13] Kolaini, A.R., 1999. “Effects of salt on bubble acoustic in water”, *J. Acoust. Soc. Am.* 105 (4), pp. 2161-2186
- [14] Holler, V., Ruzicka, M., Drahos, J., Kiwi-Minsker, L., Renken, A., 2003. “Acoustic and Visual Study of Bubble Formation Processes in Bubble Column Staged With Fibrous Catalytic Layers.” *Catalysis Today*, 79-80, p.p 151-157, (2003).
- [15] Tien, T.M., Lee, C.H., and Huang, C.J., 2007. “Study of bubble size distribution for breaking wave propagates over a submerged dike”, Vol. 3, No. 4, pp. 448-451
- [16] Manasseh, R., Riboux, G., Bui, A., and Risso, F., 2007. “Sound emission on bubble coalescence: imaging, acoustic and numerical experiments”, 16th Australian Fluid Mechanics Conference, Gold Coast, Australia, 2-7 Dec 2007, pp. 167-173
- [17] Manasseh, R., Riboux, G., Risso, F., 2008. “Sound generation on bubble coalescence following detachment”, *International Journal of Multiphase Flow*, Vol. 34, pp. 938-949
- [18] Al-Maskari, “Detection of cavitation in a centrifugal pump using acoustic emission.” Thesis. School of Engineering, Cranfield University, UK. (1985).
- [19] Neill, G.D., Reuben, R.L., Sandford, P.M., 1997. “Detection of Incipient cavitation in Pumps Using Acoustic Emission”, *Journal of Process Mechanical Engineering*, ImechE, 211(4), 267-277.
- [20] Alfayez, L., and Mba, D., 2004. “Detection of incipient cavitation and the best efficiency point of a 2.2MW centrifugal pump using Acoustic Emission”, *Journal of Acoustic Emission*, Vol. 22, 77- 82.
- [21] Yen, G., and Lu., H., 2002. “Acoustic Emission Data Assisted Process Monitoring”, *ISA Transactions* 41, 273-282.
- [22] Al-lababidi, S., Addali, A., Yeung, H., Mba, D., Khan, K., 2009. “Gas void fraction measurement in two-phase gas/liquid slug flow using acoustic emission technology”, *J. Vib. and Acoustics*, ASME, vol. 131, 6, 064501,1-7.
- [23] Addali, A., “Monitoring gas void fraction in two-phase flow with acoustic emission” PhD Thesis, Cranfield University, (2010)
- [24] Rayleigh. “On the pressure developed during the collapse of a spherical cavity.” *Philosophical Magazine*, 34(199), pp. 94-98, (1917)
- [25] Sathyam, U.S, Shearing, A, and Prael, S.A. “The effects of spot size, pulse energy, and repetition rate on the microsecond ablation of gelatine under water.” *Laser-Tissue Interaction VI, Proc SPIE*, 2391, pp. 336-344, (1995).
- [26] Shangguan, H, Casperson, L.W and Prael, S.A. “Pressure impulse during microsecond laser ablation.” *Applied Optics*, Vol.36, No. 34, pp. 9034-9041, (1997).
- [27] Xu, R.Q., Chen, X., Shen, Z.H., Lu, J., and Ni, X.W. “Optical deflection technique for investigation of laser-induced oscillating bubble on metal surface.” *Japanese Journal of Applied Physics*, vol. 43, No. 8A, pp. 5595-5599, (2004)
- [28] Blake, J.R and Gibson, D.C. “Growth and collapse of a vapour cavity near a free surface.” *J. Fluid Mech*, vol. 111, pp. 123-140, (1981)
- [29] Yasuda, T., Takahashi, N., Baba, M., Tei, K., and Yamaguchi, S. “An experimental study on micro-bubble generation by laser-induced breakdown in water.” *The Review of Laser Engineering*, Supplemental Volume, pp. 1273-1275, (2008).
- [30] Robert, E., Lettry, J., Farhat, M., Monkewitz, P.A., Avellan, F. “Cavitation bubble behaviour inside a liquid jet.” *Physics of Fluid*, 19, 067106, (2007).
- [31] Obreschkow, D., Kobel, P., Dordaz, N., De-Bosset, A., Nicollier, C., and Farhat, M. “Cavitation dynamics inside liquid drops in microgravity.” *Physical review Letters*, 97, 094502, (2006).

- [32] Buogo, S. and Canneli, G.B. "Implosion of an underwater spark-generated bubble and acoustic energy evaluation using the Rayleigh model." *Acoustical Society of America*, 111(6), pp. 2594-2600, (2002).
- [33] De-Bosset, A., Obreschkow, D., Kobel, P., Dorsaz, N., Farhat, M. "Direct effects of gravity on cavitation bubble collapse." 58 *International Astronautical Congress 2007*, pp 1-5, 1AC-07-A2.4.04, (2007).

Study on measurement technique for the amount of generated acoustic cavitation -Investigation of the characteristics of broadband integrated voltage by using dissolved oxygen level and sonochemical luminescence-

Takeyoshi Uchida/NMIJ • AIST

*Shinichi Takeuchi/Toin University of Yokohama

*Tsuneo Kikuchi/NMIJ • AIST

takeyoshi.uchida@aist.go.jp

ABSTRACT

Acoustic cavitation generated by high-pressure ultrasound has been used in medical treatments and cleaning applications. However, cavitation can cause unexpected damage, for example, to normal cells in the human body, and to an object being cleaned. Therefore, both the measurement and control of cavitation are important for ensuring safety and effectiveness. Mechanical index in the medical field and sonochemical luminescence in sonochemistry are the common methods used to investigate cavitation. However, the accuracy of these approaches is limited because they do not measure the signal generated by cavitation. Therefore, a novel cavitation measurement technique with high accuracy is required.

We have investigated a technique for measuring generated cavitation which employed broadband integrated voltage (BIV) calculated from the high-frequency components of broadband noise emitted from cavitation bubbles. In this study, the characteristics of BIV were investigated by using dissolved oxygen (DO) levels, sonochemical luminescence, and OH radical concentration. The spatial distribution of cavitation generation in a water vessel was also investigated in terms of BIV and sound pressure.

BIV was measured with a hollow cylindrical cavitation sensor as proposed by Zeqiri et al. of the National Physical Laboratory. BIV was calculated by integrating the components in the frequency range of 1 to 5 MHz. A stainless steel vibrating disk with a Langevin-type transducer was used and operated at a frequency of 150 kHz. The depth of distilled water was 100 mm in a water vessel of 190 mm in length, 190 mm in width, and 120 mm in height. A standing wave acoustic field was formed in the vessel. The sensor was positioned at a height of 40 mm above the vibrating disk.

As results, BIV was found to depend on DO levels in distilled water. A positive correlation was found between BIV, sonochemical luminescence, and OH radical concentration. These results show that BIV has the potential to be used as an index of the amount of cavitation generated. Furthermore, BIV has potential use as a more accurate measurement of the spatial distribution of cavitation than sound pressure.

1. INTRODUCTION

We have been studying the measurement of acoustic cavitation generated by high-pressure ultrasound exposure[1-3]. Cavitation plays a key role in several fields. For example, the application of cavitation has been studied in medical field such as cancer therapy and gene therapy[4-6]. In addition, cavitation has been used to clean industrial parts, such as semiconductors [7-8]. In sonochemistry, there have been several studies on the active oxygen species and shock waves generated by cavitation [9-13]. However, cavitation causes damages to normal cells in the human body and to objects being cleaned. Therefore, the measurement and control of cavitation is essential to ensure safety and effectiveness. Currently, there is no accurate technique for measuring the amount of generated cavitation required for its control.

The mechanical index (MI) [14] is the conventional method of investigating cavitation in medical field, while sonochemical luminescence[9,10,13] is used in industry field. MI is calculated from sound pressure measured by hydrophone. Sonochemical luminescence is the chemical reaction between luminol anions and the active oxygen species generated by cavitation. However, these methods do not measure the signal generated by cavitation bubbles, and thus accurate measurement is difficult. Therefore, accurate measurement technique of the cavitation is required.

We have been investigating the measurement technique for the amount of generated cavitation by using broadband noise in the frequency spectra of the received signals. When cavitation bubbles are generated in water, the frequency spectra of the received signals consist of the peaks of the operating frequency, harmonics, subharmonics and broadband noise[15]. Harmonics are also generated by nonlinear propagation of ultrasound. Therefore, when harmonics are used to measure the amount of cavitation generated, signals relating to the magnitude of the cavitation bubbles and those relating to the nonlinear propagation of ultrasound must be separated. However, it is difficult to discriminate between the two signals. Broadband noise and subharmonics are generated by the collapse and pulsation of the cavitation bubbles[15,16]. In addition, it has been reported that broadband noise is generated by temporal fluctuations in the number of cavitation bubbles[15]. It has been proposed that cavitation represents high-energy bubbles

associated with sonoluminescence or sonochemical reactions. Broadband noise and subharmonics are signals that originate from cavitation bubbles.

We have been studying the measurement technique of cavitation by using broadband noise. For the practical application of this method, it is important to compare it with conventional investigation methods. In this paper, we examined the relationship between broadband noise, cavitation generation conditions and the chemical reaction resulting from cavitation. We also investigated the spatial distribution of cavitation generation in terms of broadband noise in a water vessel.

2. MEASUREMENT SYSTEM

Figure 1 shows the basic structure of the hollow cylindrical cavitation sensor used for the measurement of broadband noise. The cavitation sensor was proposed by Zeqiri and coworkers[17-19]. The sensor was three layer structure composed of a tube of acrylic resin, a closed cell sponge, and a poly(vinylidene fluoride) (PVDF) film (20 mm long, 70 mm wide). The closed cell sponge acted as an acoustic isolator, allowing reception of the ultrasound signal inside the cavitation sensor. The thickness of the closed cell sponge was about 5 mm and that of the PVDF film was about 110 μm . The inside and outside diameters of the cavitation sensor was 25 mm and 40 mm, respectively.

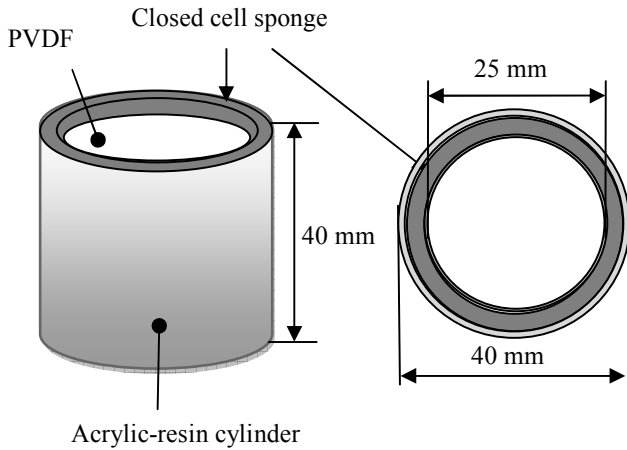


Fig. 1 Basic structure of the hollow cylindrical cavitation sensor used in the experimental system.

Figure 2 shows the configuration of the experimental system used for the generation of cavitation. A stainless steel vibrating disk (2 mm thickness, 180 mm diameter) with a bolt clamped Langevin type transducer (Honda Electronics HEC-45402) was placed on the bottom of a water vessel (190 mm long, 190 mm wide, and 120 mm high). The output signal of a function generator (Agilent 33250A) was amplified using a power amplifier (AR 75A250). The amplified signal was applied to the Langevin type transducer. A continuous sinusoidal wave was emitted at an operating frequency of 150 kHz. A standing wave acoustic field was formed in the water vessel. The depth of distilled water in the vessel was about 100 mm. The cavitation sensor was placed at the center of the vessel approximately 40

mm above the vibrating disk. The output signal of the cavitation sensor was sent to a digital oscilloscope (Sony Tektronix TDS2012B).

A needle hydrophone (Onda HNR-1000) was used to measure sound pressure in the water vessel. Sound pressure was used for a comparison of broadband noise, and was measured at antinode in standing wave acoustic field. The hydrophone would be damaged by cavitation above 60 V, thus sound pressure was measured in the applied voltage range from 0 to about 60 V. Therefore, the sound pressures above 60 V were obtained by extrapolation. As a result, BIV was investigated between 0 and about 900 kPa.

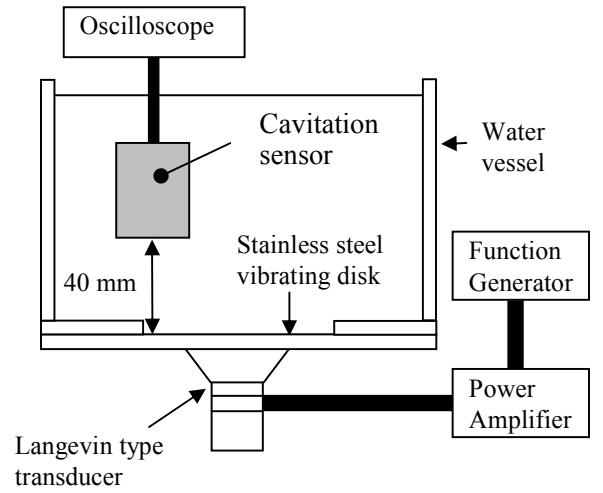


Fig. 2 Experimental system for the generation of acoustic cavitation by high pressure ultrasound exposure.

Broadband integrated voltage (BIV) was used to investigate the amount of cavitation generated. BIV was calculated by integrating the high-frequency components of broadband noise in the frequency spectra of the signals received by the cavitation sensor. Broadband noise of high-frequency components in the frequency spectra originate from the collapse and pulsation of cavitation bubbles. Therefore, BIV is a parameter that reflects the signal generated by the cavitation bubbles. BIV is defined as

$$\text{BIV} = \int_{f_1}^{f_2} V(f) df, \quad (1)$$

where $V(f)$ represents the frequency-dependent spectrum magnitudes of the signal received from the cavitation sensor. In this study, the frequency limits used in integration were taken to be $f_1 = 1 \text{ MHz}$ and $f_2 = 5 \text{ MHz}$.

3. RESULTS AND DISCUSSION

3.1 Relationship between dissolved oxygen levels and BIV

We measured BIV and dissolved oxygen (DO) levels in distilled water. The DO level governs the generation of cavitation at a given sound pressure. The DO level was

measured by a DO level meter (Iijima Electronics ID-100). DO levels of about 8.3 and 2.3 mg/L were used. A DO level of about 8.3 mg/L was the saturation state, while a DO level of about 2.3 mg/L was the degassed state.

The relationship between sound pressure and BIV is shown in Fig. 3. At DO level of 8.3 mg/L, BIV increased rapidly with increasing sound pressure above about 450 kPa. However, there was almost no variation in BIV with increasing sound pressure at a DO level of 2.3 mg/L. The amount of cavitation bubbles generated by cavitation is known to be affected by the DO level in distilled water, and cavitation is generated more easily at higher DO levels. Therefore, it was thought that the increase in BIV with sound pressure at a DO level of about 8.3 mg/L occurred because a large amount of cavitation was generated. Meanwhile, there was a small change in BIV with sound pressure at a DO level of 2.3 mg/L because the amount of cavitation generated was small.

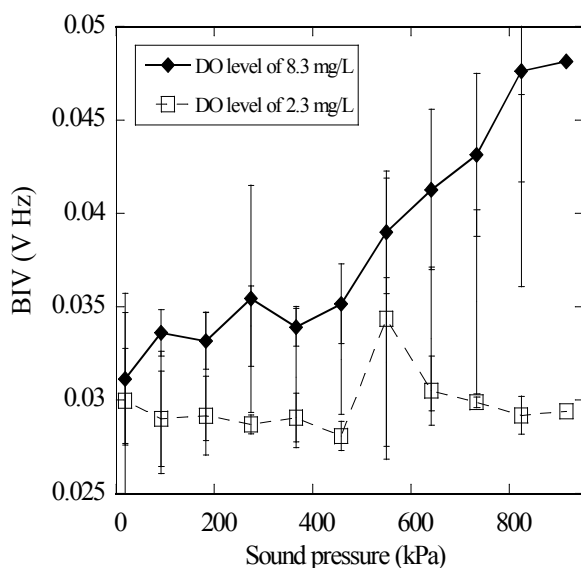


Fig. 3 Relationship between sound pressure and BIV

3.2 Investigation of BIV by sonochemical luminescence and OH radicals

BIV was investigated via sonochemical luminescence and OH radical resulting from the dissociation of water by cavitation. Distilled water at DO levels of about 5 and 8 mg/L were used. Sonochemical luminescence occurs as a chemical reaction between luminol anions and the active oxygen species generated by cavitation. Therefore, it is thought that the intensity of luminescence is proportional to the concentration of active oxygen species generated by cavitation. The intensity of luminescence was measured with a photomultiplier (Hamamatsu Photonics R585) and a photon-counting unit (Hamamatsu Photonics C9744).

The relationship between BIV and the luminescence are shown in Figs. 4 and 5. At a DO level of about 8 mg/L, the BIV and luminescence increased from sound pressures of about 450

kPa, as shown Fig. 4. Furthermore, at DO level of about 5 mg/L, both BIV and luminescence increased above sound pressures more than about 600 kPa, as shown in Fig. 5. As the results of Figs. 4 and 5, a strong correlation was found between BIV and luminescence.

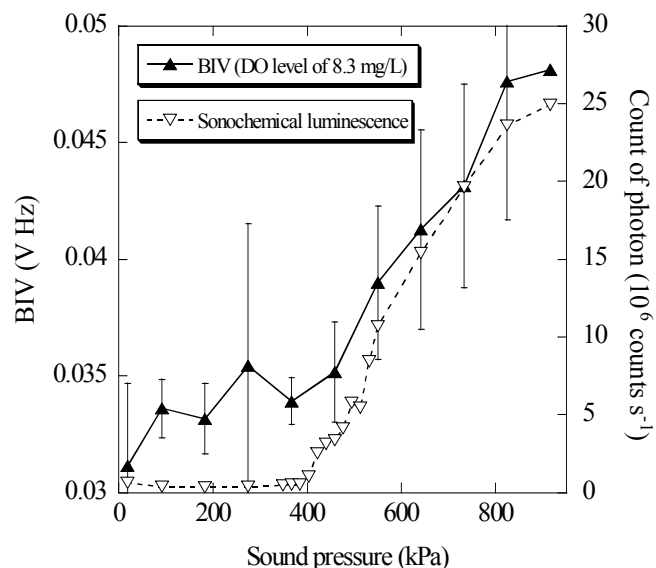


Fig. 4 Variation in BIV and sonochemical luminescence with sound pressure at DO level of about 8.3 mg/L

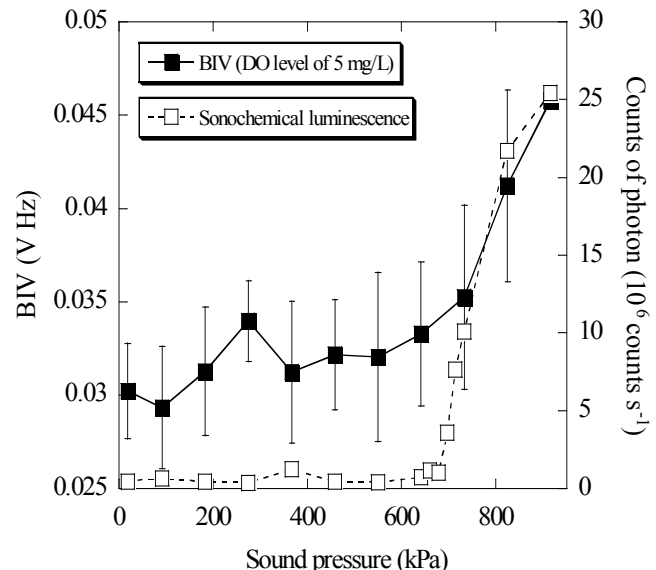


Fig. 5 Variation in BIV and sonochemical luminescence with sound pressure at DO level of about 5 mg/L

Next, BIV was investigated by measuring OH radicals generated by cavitation. Measurement method of OH radicals was detected by spin trap method with DMPO, and measured by Electron Spin Resonance (JEOL JESFA200). The cavitation

generated was measurable by the amount of DMPO-OH, which equaled the amount of OH radical generated. The DO level of the distilled water was about 8 mg/L. As a result, a correlation was found between BIV and OH radicals. These results collectively show that BIV has the potential to be used as an index of the amount of cavitation generated, as shown in Figs. 3, 4, 5 and 6.

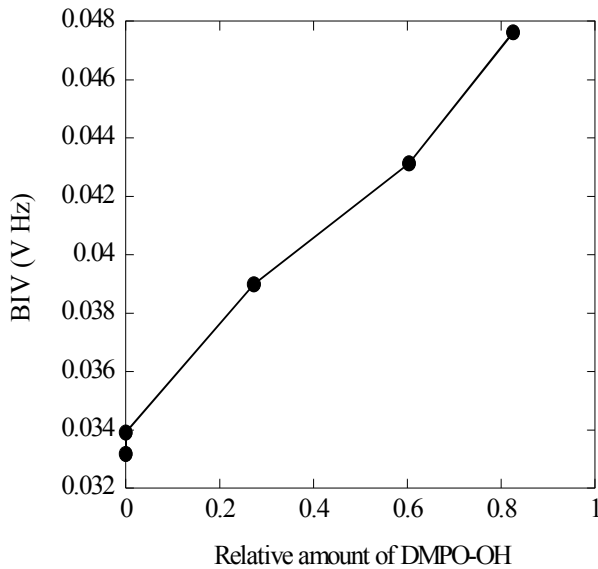


Fig. 6 Relationship between amount of DMPO-OH and BIV.

3.3 Investigation of the spatial distribution of cavitation generation in a water vessel in terms of broadband noise.

We investigated the one dimensional distribution of cavitation generated in a water vessel in terms of BIV. The spatial distribution of cavitation generation is generally investigated by sound pressure. Therefore, BIV and sound pressure were compared to establish a novel technique for measuring cavitation generation distribution with high accuracy.

In this experiment, the cavitation sensor was again positioned at a height 40 mm above the stainless steel vibrating disk. The sensor was scanned along the center line of the vibrating disk to measure the change in BIV across the vessel. Sound pressure was measured with a hydrophone under the same scanning conditions. The DO level in distilled water was at saturation state of about 8 mg/L.

The changes in BIV and sound pressure relative to position across the center line of the vibrating disk in a water vessel are shown in Fig. 7. The peak position of BIV and sound pressure was different. The peak positions of BIV were about -15 and 15 mm in the vessel. Meanwhile, peak positions of sound pressure were about 0 and 5 mm near the center of the vessel. Although sound pressure was high at the center position of the vessel, BIV was low and decreased toward the side-walls of the vessel.

The conditions in the water vessel were observed to consider in terms of the differences of the position of peaks of BIV and sound pressure. A photograph of the side surface of the vessel is shown in Fig. 8. Acoustic streaming was observed

toward the surface of the water at center of the vibrating disk. For the observation of the acoustic streaming, 0.3 g of aluminum powder and 1.5 g of dodecyl sodium sulfate were added to 3000 mL of distilled water. The suspension was irradiated with a laser. Acoustic streaming was observed with a camera from the side surface of the water vessel. The photographic conditions were as follows : exposure time, 2 s; international organization for standardization film speed, 100; and aperture, f32.

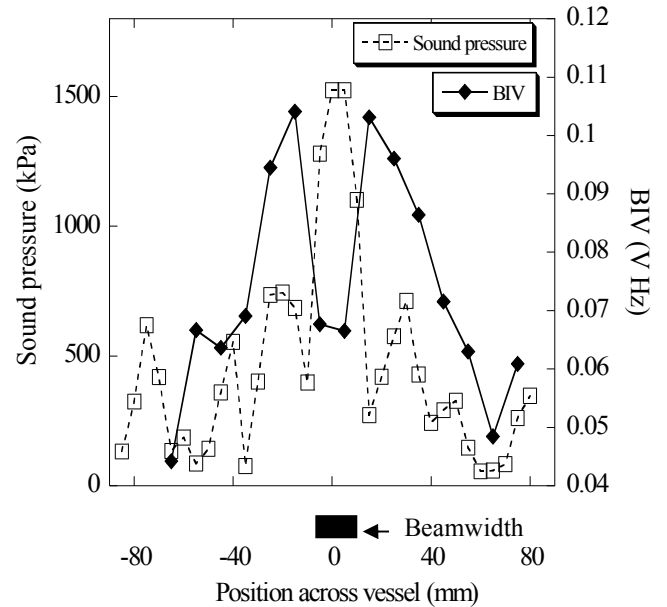


Fig. 7 Change in BIV and sound pressure in horizontal direction of water vessel

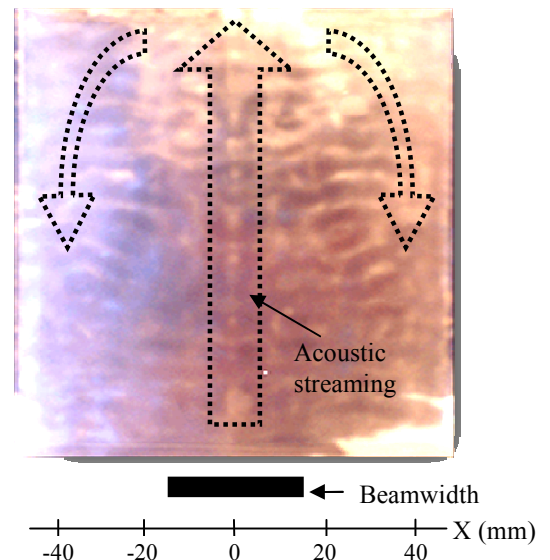


Fig. 8 Photograph of acoustic cavitation generated at the center position of the water vessel.

The peaks of BIV and sound pressure were different, as shown in Fig. 7. Acoustic streaming toward the surface of the water was generated at the center position of the water vessel, as shown in Fig. 8. Cavitation bubbles generated by high pressure ultrasound in the center region flowed toward the surface of the water via the acoustic streaming. The transfer of cavitation bubbles was thought to be a possible cause of the difference in the peak positions of BIV and sound pressure. Cavitation bubbles were not trapped at the center position of the vibrating disk because of acoustic streaming. Therefore, the signals according to the magnitude of the collapse and pulsation of the cavitation bubbles were small. Hence, although the sound pressure was high, BIV was low at the positions of about 0 mm and 5 mm. In addition, flowing cavitation bubbles were trapped at the positions of -15 and 15 mm. BIV was high at the same position. Sonochemical luminescence was confirmed the existence of the trapped cavitation bubbles. The luminescence could not be observed in the central region at heights lower than about 60 mm from the vibrating disk in a water vessel because cavitation bubbles could not be trapped due to acoustic streaming toward the surface of the water. Therefore, BIV was small, as shown in Fig. 7. Furthermore, BIV was high in the region where the luminescence was emitted. The photograph of sonochemical luminescence is shown in Fig. 9. These results show that, compared with sound pressure, BIV had the potential to be a more accurate measurement of the spatial distribution of cavitation generation.

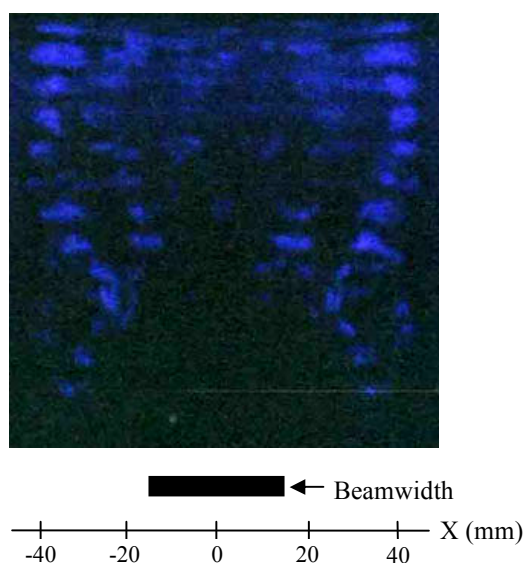


Fig. 9 Photograph of sonochemical luminescence in the water vessel.

4. CONCLUSIONS

We have investigated the measurement technique for the amount of generated acoustic cavitation using BIV, which is the signal that shows the magnitude of the collapse and pulsation of cavitation bubbles. BIV was calculated from high frequency components in the megahertz range of the output voltage from a cavitation sensor. The relationship between BIV and DO levels

in distilled water that is cavitation condition was investigated. Next, BIV was investigated by sonochemical luminescence and the OH radicals resulting from cavitation. Finally, we compared BIV and sound pressure to investigate the spatial distribution of the cavitation generation in a water vessel.

The results show that BIV depended on the DO level in distilled water. A strong correlation was found between BIV, sonochemical luminescence and OH radicals generated by cavitation. From these results, BIV has potential to be used as an index of the amount of generated cavitation. Also, the peak positions of BIV and sound pressure in the water vessel were difficult. Although sound pressure showed a peak at the center position, BIV was low. Because the cavitation bubbles were not trapped at the center position due to acoustic streaming toward the surface of the water. Thus, BIV is a more assured tool for measuring the spatial distribution of cavitation generation.

In the future, we will undertake a more detail investigation of the measurement technique for the amount of generated cavitation using BIV. The 25 mm inner diameter of the cavitation sensor in this paper was larger than the 10 mm wavelength of the operating frequency of 150 kHz. Furthermore, the overlap of the measurement region was 15 mm for a scanning interval of 10 mm. Therefore, the spatial resolution of the cavitation sensor was low. Consequently, a detailed investigations by optimizing the size of the cavitation sensor will be performed. In addition, BIV will be compared with subharmonics. We plan to use BIV to investigate the performance of ultrasound devices using acoustic cavitation.

ACKNOWLEDGMENTS

This work was supported by a Grant-in Aid for Scientific Research B (No. 21300195).

REFERENCES

- [1] T. Uchida, H. Sato, S. Takeuchi, and T. Kikuchi: *Acoust. Sci. & Tech.* **31** (2010) 199.
- [2] T. Uchida, H. Sato, S. Takeuchi, and T. Kikuchi: *Jpn. J. Appl. Phys.* **49** (2010) 07HE03.
- [3] T. Uchida, S. Takeuchi, and T. Kikuchi: *Proceeding of Symposium on Ultrasonic Electronics*, **31** (2010) 367.
- [4] A. Watanabe, R. Otake, T. Nozaki, A. Morii, R. Ogawa, S. Fujimoto, S. Nakamura, H. Fuse, and T. Kondo: *Cancer Lett.* **265** (2008) 107.
- [5] A. Watanabe, K. Kawai, T. Sato, H. Nishimura, N. Kawashima, and S. Takeuchi: *Jpn. J. Appl. Phys.* **43** (2004) 3245.
- [6] M. A. Hassan, L. B. Feril Jr., K. Suzuki, N. Kudo, K. Tachibana, T. Kondo: *Ultrason. Sonochem.* **16** (2009) 372.
- [7] S. Okano, K. Kawada, M. Nakamori, T. Nitta, and T. Ohmi: *Proc. ISSM'07*, **1** (2007) E9.
- [8] B. Fraser, S. Rafie, M. Eissa, and S. Joshi: *Solid State Technol.* **7** (2000) 105.
- [9] T. Uchida, T. Kikuchi, S. Isa, N. Kawashima, and S. Takeuchi: *Jpn. J. Appl. Phys.* **47** (2008) 4115.
- [10] T. Uchida, T. Kikuchi, T. Aoki, N. Kawashima, and S. Takeuchi: *Jpn. J. Appl. Phys.* **48** (2009) 07GH03.
- [11] K. Yasuda, K. Matsuura, Y. Asakura, and S. Koda: *Jpn. J. Appl. Phys.* **48** (2009) 07GH04.

- [12] T. Kozuka, K. Yasui, S. Hatanaka, T. Tuziuti, J. Lee, and A. Towata: Jpn. J. Appl. Phys. **49** (2010) 07HE14.
- [13] S. Hatanaka, S. Hayashi, and P. Choi: Jpn. J. Appl. Phys. **49** (2010) 07HE14
- [14] IEC62359 First edition (2005)
- [15] K. Yasui, T. Tuziuti, J. Lee, T. Kozuka, A. Towata, and Y. Lida: Ultrason. Sonochem. **17** (2010) 460.
- [16] J. Frohly, S. Labouret, C. Bruneel, I. Looten-Baquet, and R. Torguet: J. Acoust. Soc. Am. **108** (2000) 2012.
- [17] B. Zeqiri, P. N. Gelat, M. Hodnett, and N. D. Lee: IEEE Trans. Ultrason. Ferroelectr. Freq. Control, **50** (2003) 1342.
- [18] B. Zeqiri, P. N. Gelat, M. Hodnett, and N. D. Lee: IEEE Trans. Ultrason. Ferroelectr. Freq. Control, **50** (2003) 1351.
- [19] M. Hodnett, and B. Zeqiri: IEEE Trans. Ultrason. Ferroelectr. Freq. Control, **55** (2008) 1809.

Time Resolved X-Ray Densitometry System for Cavitating Flows

Simo Mäkiharju*
University of Michigan, Ann Arbor

Steven L. Ceccio
University of Michigan, Ann Arbor

Corresponding author: *smakihar@umich.edu

ABSTRACT

Cavitating flows are encountered in many industrial and naval applications [1, 2]. To gain insight into the flow physics and aid in the development of physical models, knowledge of the spatial and temporal evolution of void fraction is often required. The measurement of local void fraction is challenging, especially in cavitating flows where any intrusive probe would likely perturb the flow considerably. In the present work, an X-ray densitometry system is described which is capable of measuring the void fraction in a cavitation tunnel through 20 cm of water, for up to a 225 cm² area at frame rates of up to 4000 fps. We present the experimental setup of the densitometry system, the governing equations, results from system validation tests and from a test case where non-condensable gas was used to create a partial cavity behind a backward facing step. The system will subsequently be utilized to study a cavitating flow in the same flow geometry.

NOMENCLATURE

BFS	Backward facing step	
n	material designator (air, water, mix, <i>etc.</i>)	
N	total number of materials	
a	air	
g	glass/acrylic	
m	mixture	
w	water	
II	Image Intensifier	
Q_{det}	Detection efficiency	[-]
t	thickness of domain in beam path	[m]
U	free stream velocity at the BFS	[ms ⁻¹]
V	Photon energy	[eV]
x	Streamwise coordinate	[m]
y	Coordinate normal to the test surface	[m]
z	Spanwise coordinate	[m]
α	Void fraction	[-]
δ	Boundary layer thickness	[m]
θ	Momentum thickness	[m]
ρ	Density	[kg m ⁻³]
I_0	Original intensity/number of photons	[-]
I	Transmitted intensity/number of photons	[-]
μ_n/ρ_n	Mass attenuation coefficient of material n	[m ² kg ⁻¹]
x_n	Mass thickness of material n	[kg m ⁻²]

1. INTRODUCTION

To measure the void fraction in a cavitating or multiphase flow in a nonintrusive manner, electrical resistance and impedance techniques have often been used quite successfully [3-6]. However, these techniques are based on a soft-field, where the result is dependent of the flow topology and depending on the flow considered *a priori* knowledge of the topology may be required to obtain a solution. Radiation densitometry has the benefit of being a hard-field measurement, meaning the beam path is not dependent of the object being measured. Gamma-radiation based techniques have been used by themselves and also to validate electrical impedance measurements [7,8], but it is difficult for most research laboratories to gain access to a high quality radiation source such as a high energy gamma source or a synchrotron. The next best option is using X-ray. X-ray tubes such as those used in the medical field are readily available, and multiple researchers have used X-ray imaging to investigate both cavitation [9-12] and bubbling fluidized beds [13]. Some groups have also developed custom systems based on electron beam scanning [14].

In the present experimental setup, we wish to image gas-liquid flows through a test section that is ~20 cm thick, which is thicker than most previously reported cavitation studies. Moreover, we wish to make full-field, time resolved measurements on the order of kilohertz frame rates, since this would be required to resolve the time-evolution of sheet cavitation. To meet these requirements with resources available, it was decided to construct a system utilizing a regular image intensifier with fast decaying phosphor and a source capable of high radiation output, albeit with a total exposure limited to only few second at a time.

2. PHYSICAL PRINCIPLES

When a beam of high-energy photons, *e.g.* X-rays, is directed toward a domain, a fraction of the photons will pass through the domain without scattering or absorption, and the fraction of the beam that passes through is related to the mass attenuation coefficients of the materials present along the path of the beam. Hence, for a domain with N distinct materials

$$\frac{I}{I_0} = e^{-\sum_{n=1}^N \mu_n / \rho_n x_n} = \prod_{n=1}^N e^{-x_n \mu_n / \rho_n}$$

where I_0 is the original intensity of the photon beam, I is the intensity of the photons transmitted, μ_n/ρ_n is the mass attenuation coefficient and x_n is the mass thickness over the beam path traversed in material n . The attenuation coefficient is dependent on photon energy and for any material in the domain is related to the material density and its atomic properties [15]. A measure of the change in intensity can be readily converted into a measure of the average density of the known material along the beam-path. In the case of gas-liquid flows, this yields a quantitative measure of the void fraction. Similar time-averaging single-beam systems have been in use in the multiphase flow community for over a decade [9, 13].

With only water (or air) in the test section shown in fig. 4a the beam passes through air, a , acrylic window, g , water, w , etc.

$$\frac{I_w}{I_0} = e^{-x_a \mu_a / \rho_a} e^{-x_g \mu_g / \rho_g} e^{-x_w \mu_w / \rho_w} e^{-x_g \mu_g / \rho_g} \dots$$

With unknown mixture in the test section, but everything else remaining unchanged

$$\frac{I_m}{I_0} = e^{-x_a \mu_a / \rho_a} e^{-x_g \mu_g / \rho_g} e^{-x_m \mu_m / \rho_m} e^{-x_g \mu_g / \rho_g} \dots$$

Dividing the former with the latter equation, noting that total beam path lengths remain constant and simplifying yields

$$\frac{I_w}{I_m} = e^{t(\mu_m - \mu_w)}$$

For the ratio of photons of a given energy passing through the same test section when it is full of water or contains a mixture. Repeating the procedure for a case where there is only air, or only water in the test section and noting that the attenuation coefficient for a two phase mixture is given by

$$\mu_m = \alpha \mu_a + (1 - \alpha) \mu_w$$

Then the equation relating the beam intensities at a single given photon energy level to void fraction can be written as

$$\alpha = \ln\left(\frac{I_m}{I_w}\right) / \ln\left(\frac{I_a}{I_w}\right)$$

This expression has been used by numerous researchers [10, 12]. However, when using a polychromatic source and non energy resolving detector, it should be noted that the value actually measured by the detector is the light intensity at each pixel of the camera, which is related to intensity I by

$$E = \int_0^{V_{max}} I(V) Q_{det}(V) V dV$$

where V is the photon energy, $I(V)$ is related to number of photons hitting a given area of the imager screen and $Q_{det}(V)$ is the II's detection efficiency. Since the attenuation and detection efficiency (the efficiency at which X-ray photons are transformed into photoelectrons and then into photons in the

visible range) also depends on the energy of the X-ray photons, V , I/I_0 and E/E_0 are not equivalent. The implications of this will be discussed in the context of beam spectrum selection *via* beam hardening.

Beam hardening modifies the shape of the spectrum of an X-ray beam as it passes through a domain. The lower energy photons in the spectrum are preferentially attenuated compared to the higher energy photons, leading to an increase in the average photon energy of the beam. Figure 1 shows the mass attenuation coefficient of water as a function of photon energy, and it is clear that lower energy photons are more highly attenuated than higher energy photons. To mitigate impact of beam hardening on the measurement when using a polychromatic X-ray spectrum and non energy resolving detector, the beam can be *pre-hardened* by using a filter, such as a slab of highly attenuating material (e.g. aluminium or steel). This shapes the spectrum as shown in Figure 2.

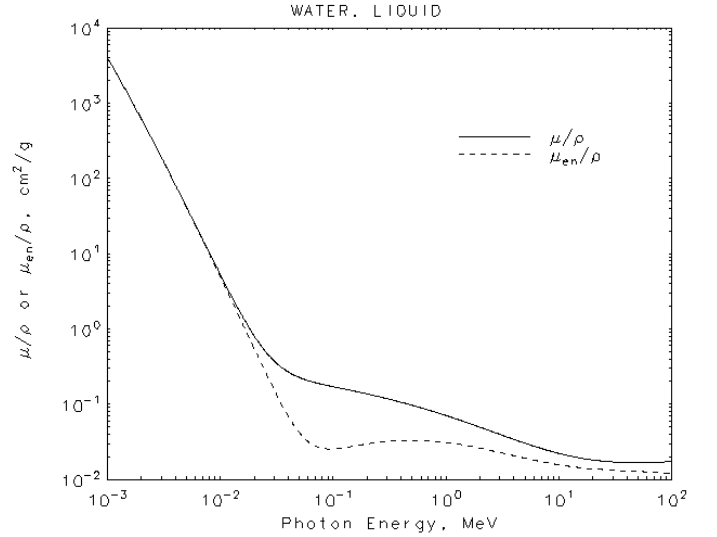


Figure 1. Mass attenuation coefficient of water as a function of photon energy plotted on a log-log scale. Figure by NIST [15].

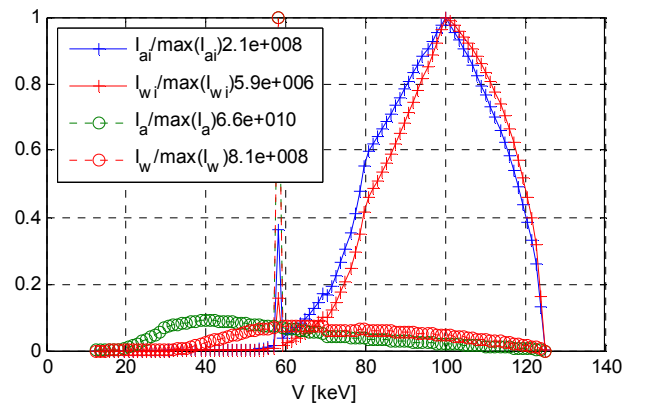


Figure 2: The photon energy spectra can be “shaped” by filtering with a highly attenuating material. Green - original spectra, Blue - spectra filtered/hardened with a 0.6mm thick steel plate. Red – spectra after passing through the test section.

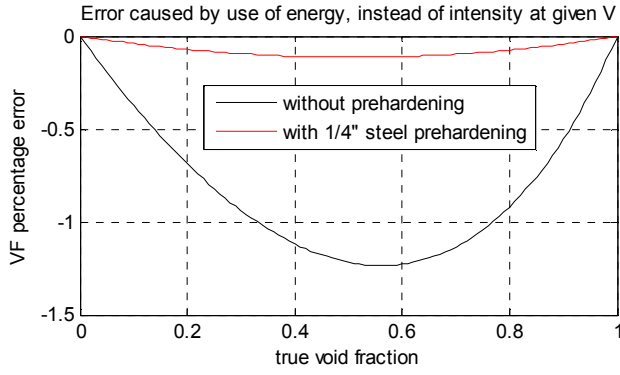


Figure 3. Illustration of the reduction of error when the void fraction is computed using the ratio of the energy from a polychromatic beam with or without pre-hardening

Alles and Mudde [16] discuss the effects of beam hardening and use of “effective attenuation coefficients” to deal with these effects. However, as shown in Figure 3 for the cases discussed in this paper, the maximum bias error for the calculated void fraction can be reduced to less than 0.5%.

3. TEST FACILITY AND EQUIPMENT

The X-ray system was built around an existing cavitation tunnel at the University of Michigan. A new test section, that is 86.4 cm long with a $(21.0 \text{ cm})^2$ cross-section and 2.9 cm chamfer in the corners, was constructed for these experiments. The test section windows are 15.2 cm by 86.4 cm providing good optical access, and the transparent windows can be as thin as 1 cm, to reduce the baseline X-ray attenuation. The flow in the test section can achieve speeds in excess of 18 m/s, and the pressure can be varied from that below vapor pressure to over 200 kPa.

The X-ray densitometry setup is shown in Figure 4. A 150 kV rotating anode tube designed for radiography, cine-radiography and angiography (Varian G-1092 insert in Varian B-160H housing) was chosen to provide the necessary photon energy and flux to achieve time resolved measurements. The source can be operated at up to 800 mA (at 81 kV) or 150 kV (at 433 mA), when supplied by selected 65kW high frequency ($>100 \text{ kHz}$) generator with a high-speed starter. It is important to provide a flux of photons at sufficiently high energy levels such that a notable fraction of the photons pass through the domain. But, the transmitted photon flux must also be sensitive to small changes in the domain's attenuation (e.g. variation in the void fraction). Finally, the photon energy levels also needed to be suitable to be used with commercial image intensifiers.

The imager subsystem is made up by the combination of a high-speed camera (Vision Research v9.0) coupled with a high efficiency high-resolution image intensifier (II). A tri-field ($12''/9''/6''$) image intensifier was chosen to enable image magnification without changing the physical setup of the experiment. It has a resolution of 48/54/62 line pair per cm, conversion factor of $320 \text{ cdm}^2/\text{mRs}^{-1}$ and 65% DQE (detection quantum efficiency) at 59 keV. An image intensifier was chosen rather than an array of detectors in order to have an economical system that is still capable of rapidly acquiring information about the attenuation through multiple beam-paths.

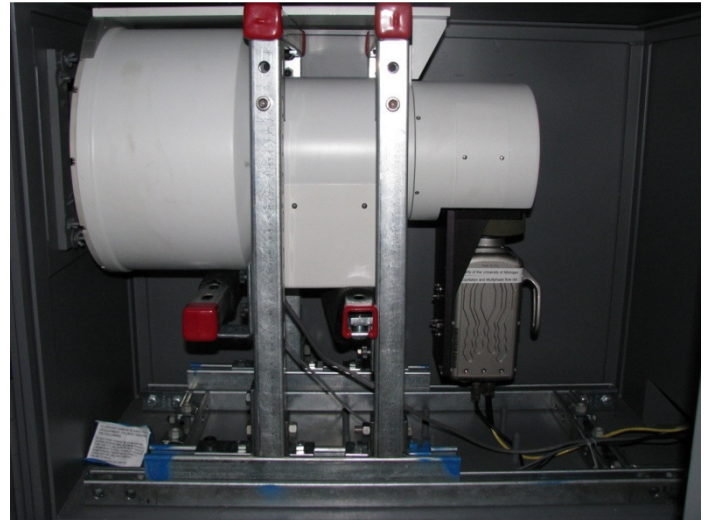
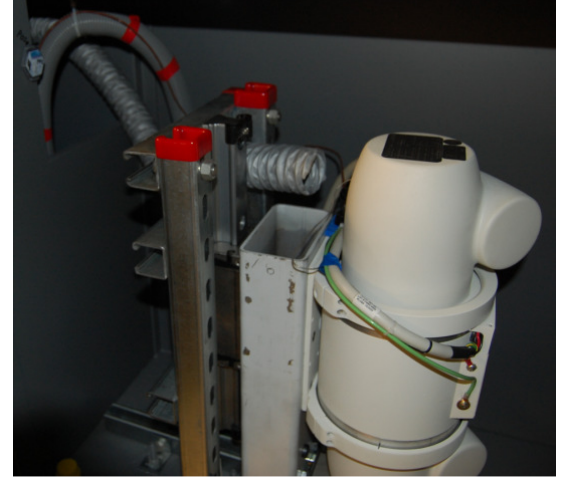
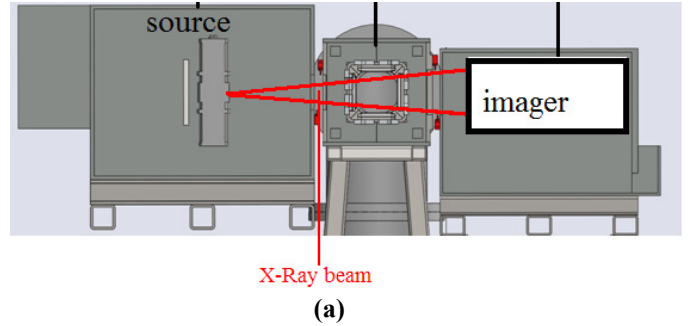


Figure 4. Sketch of the X-ray densitometry system showing the source enclosure on the right, test section in the middle and imager enclosure on the left (a). An image of the X-ray source is shown in (b), and the image intensifier is shown in (c), with the high-speed optical camera also visible. Both are housed in the custom lead enclosure designed for easy access to the test section.

The incoming X-ray photons enter the enclosure with the II through a viewport, interact with the input phosphor to produce electrons which are subsequently accelerated and hit a second output phosphor. The output phosphor produces photons in the visible wavelengths detectable by an optical high-speed camera. The light collected at each of the camera's 1.92 million pixels (or a subassembly of neighboring pixels) gives a measure of attenuation through one unique beam path.

Improvement, for this test, of the beam's energy spectrum was achieved through hardening the beam. A 0.6 mm thick steel filter was used to decrease the difference of the lightest and darkest regions by a factor of 1.98. Without the increased attenuation of the lower energy photons everywhere, the difference in those passing through the low void fraction region compared to those that were mostly absorbed by the 20 cm of water caused the imager to be saturated at the brightest region though the darkest region would have almost no signal.

4. X-RAY IMAGE DISTORTION AND RESOLUTION

The image intensifier introduces a "pincushion" distortion, and also the optics in front of the camera can additionally distort the captured image. To correct for this distortion, a calibration image is needed and the procedure is quite similar to that used in Particle Imaging Velocimetry, except the calibration grid is placed on the imager and the markers must have different attenuation than the surrounding material.

Figure 5 shows an aluminum calibration grid that was placed on the II-screen and used to correct for the II's pincushion distortion. The rods and other features of the model are used to find the central beam path of the X-ray cone produced by the source.

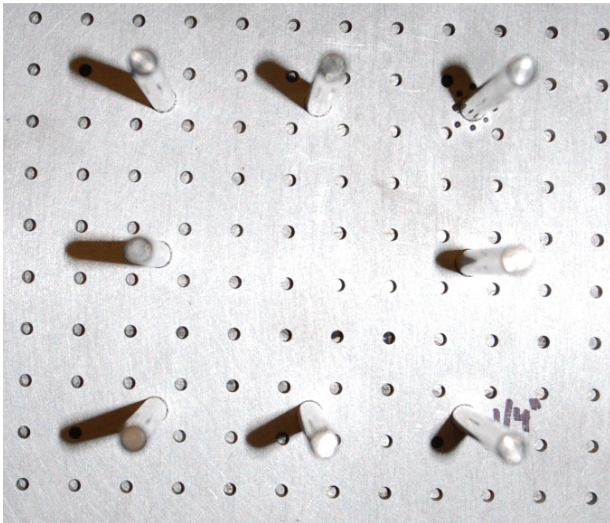


Figure 5. A calibration plate was made with 3.3mm holes regularly spaced 12.7 mm apart. 15 cm long parallel rods were additionally used, as their projections could be used to determine the relative location of the source with respect to the imager.

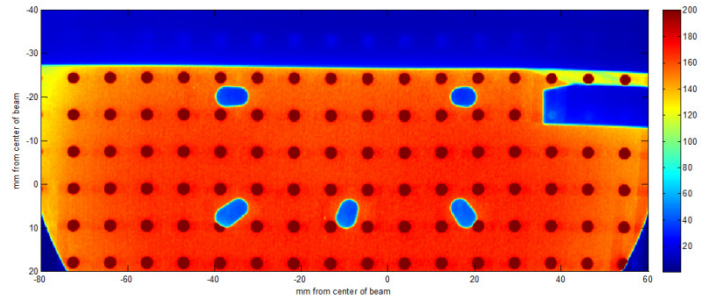


Figure 6. Calibration image after feature recognition algorithm is applied and the image dewarped. Small amount of distortion remains at the extreme right edge because the model obscured the markers, but this area is not of interest.

Using the reference image of the calibration grid for each II magnification settings, an algorithm was used to determine the marker locations and correct for the image distortion. Many researchers have proposed various dewarping algorithms to correct for the distortion caused by image intensifiers. Cerveri *et al.* [17] for example discuss local unwarping polynomials and radial basis function neural networks. We are currently using DaVis 7.2 (Lavision Inc.) calibration functions with 3rd order polynomials to dewarp the image.

A standard X-ray resolution test tool with 16 to 50 lines/inch (0.63 to 1.97 lines/mm) was used to quantify the system resolution. Besides the camera and phosphor resolution, the image is blurred due to the finite size of the source's focal spot, causing a penumbra [18]. The source could be operated with a 0.6 mm or 1.2 mm focal spot, with the smaller yielding better image sharpness, but limiting the power that could be used without damaging the source. Figure 7 is an image of the resolution test tool, illustrating that in just the basic system configuration we can resolve up to ~2 lines/mm.

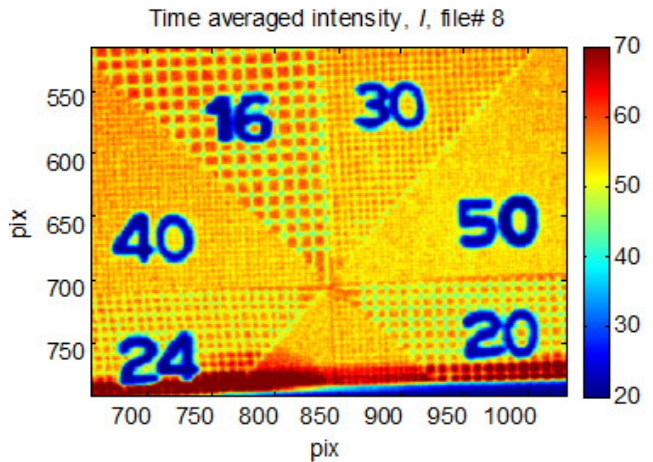


Figure 7. X-ray image of a standard-resolution test tool in the flow domain. The numbers in the image give the grid spacing in units of lines per inch.

5. UNCERTAINTY IN VOID FRACTION

The error in the measurement of light intensity at a given pixel due to random variation of the source strength and due to finite bit depth of the detector (camera) could contribute significantly to the uncertainty of the calculated void fraction. To obtain a reasonable estimate for the accuracy of the void fraction measurement let us assume the value at each pixel of the 8-bit camera is correct within $\pm\Delta I$ (or that the random variation of the source or contribution from scatter cause $\pm\Delta I$ error). The overall error can be estimated from [19]

$$E_{arms} = \sqrt{\left(\Delta I_m \frac{\partial \alpha}{\partial I_m}\right)^2 + \left(\Delta I_a \frac{\partial \alpha}{\partial I_a}\right)^2 + \left(\Delta I_w \frac{\partial \alpha}{\partial I_w}\right)^2}$$

Where ΔI is the uncertainty in the intensity. Using the relationship between attenuation and void fraction, eqn. 1, yields

$$E_{arms} = \frac{\Delta I_m}{I_a I_m I_w \ln^2 \frac{I_a}{I_w}} \times \sqrt{I_a^2 (I_m^2 + I_w^2) \ln^2 \frac{I_a}{I_w} - 2 I_a^2 I_m^2 \ln \frac{I_a}{I_w} \ln \frac{I_m}{I_w} + I_m^2 (I_a^2 + I_w^2) \ln^2 \frac{I_m}{I_w}}$$

Now the error envelope, from these sources, can be added onto the void fraction data. It can be seen that the uncertainty increases as the void fraction nears the low end of the calibration range. However, a separate calibration can be performed for multiple ranges to alleviate this.

Six containers with parallel walls spaced 1.6 mm to 101.6 mm apart were constructed for use as void-fraction calibration phantoms that could be filled and emptied with water without moving them. The combined thickness of water could be varied from 0 to 191.3 mm. The cumulative uncertainty of the water path thickness through the six calibration volumes was estimated to be 1-2 mm leading to a 0.5-1.0% uncertainty in the reference void fraction.

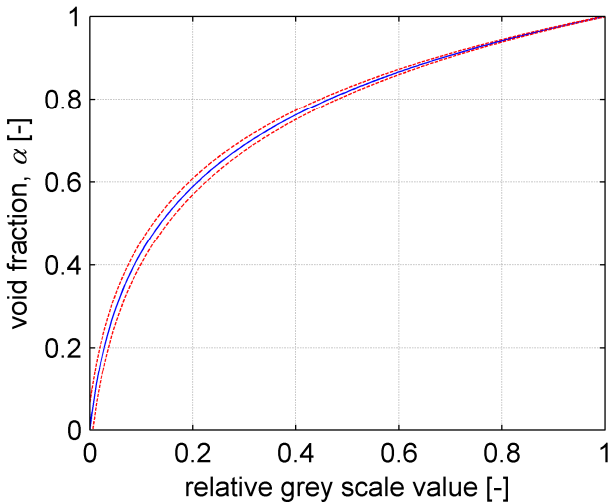


Figure 8: Assuming $\Delta I = \pm 1$, $I_w = 6$ and $I_a = 240$

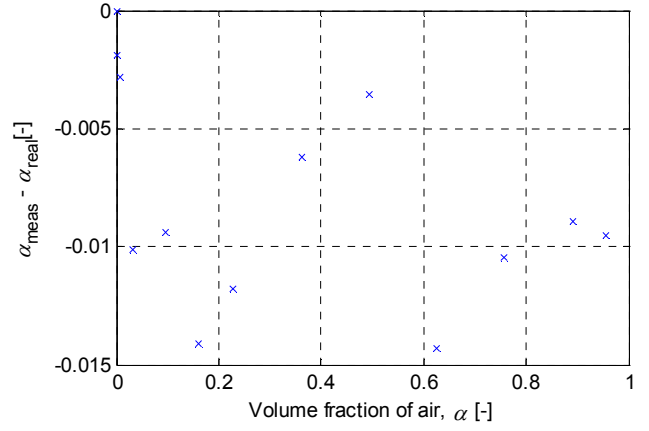


Figure 9. Results of void fraction calculated using eqn. 1 vs. the known void fraction. Approximately 200 individual frames were averaged for each void fraction, and a 60,000 pixel area averaged to get the void fraction for comparison.

The scatter about -0.74% in figure 9 could potentially be attributed to varying error in the thickness of the six reference volumes, and random variation of the source strength. A smoothly varying error could have been expected from the beam hardening and varying effect of dynamic range as a function of the void fraction. These results suggest that the X-ray system can be calibrated to determine the path-averaged volume fraction in the domain within a few percent void-fraction over a range of void fraction from 0% to 100%. The precision in void fraction can be improved if the desired measurement range is reduced and calibration in that range performed.

6. CORRECTION FOR NON-PARALLEL BEAM PATHS

The image is additionally "distorted" because of the X-rays are not parallel for all x and y , due to the conical source beam fanning out at finite angles, as shown in Figure 10. This can be corrected for if the flow is assumed to be perfectly two dimensional. However, when the area of interest is small and the beam properly positioned, the correction needed for beam divergence is relatively minor, as the beam paths would be nearly parallel. For the case considered in the next section, the dimensions of the area of interest extend ± 0.6 mm vertically and ± 5 cm horizontally from the center of the beam, and the source is 80 cm from the tunnel. Therefore, the largest angle of the beam is ~ 1.8 degrees. We are currently working on a deconvolution algorithm for regions of the domain where the beam divergence is significant.

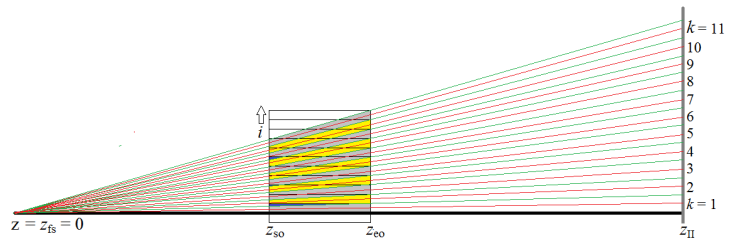


Figure 10. Illustration of the beam paths in the z,y -plane passing through a two-dimensional domain.

7. EXAMPLE MEASUREMENT

We will illustrate the void fraction measurement using a well-controlled flow: a partial air cavity formed behind a backward facing step. The model used was a 91 cm long flat plate with a $H_{BFS}=12.7$ mm tall backward facing step 35 cm from the leading edge, and a span of 209.6 mm. The boundary layer upstream of the cavity separation was tripped at the leading edge of the 2:1 ellipse. A gate was used to form a free surface upstream of the model to allow for long period of air injection. The test speed was $U = 1.8$ m/s, and boundary layer just upstream of the cavity separation has thickness of $\delta = 5.7$ mm and the momentum thickness $\theta = 0.7$ mm. Pressure in the test section was kept nominally at 1 atm. Figure 11 shows a schematic of the test model. Figure 12 shows two images of the air cavity. The first (Figure 12a) is from the side, and the second (Figure 12b) is from an oblique viewing angle from below.

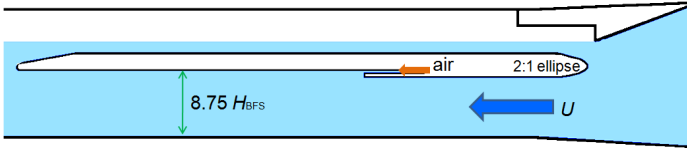


Figure 11. Schematic of the model in the test section. A free surface forming gate was located immediately upstream of the model.

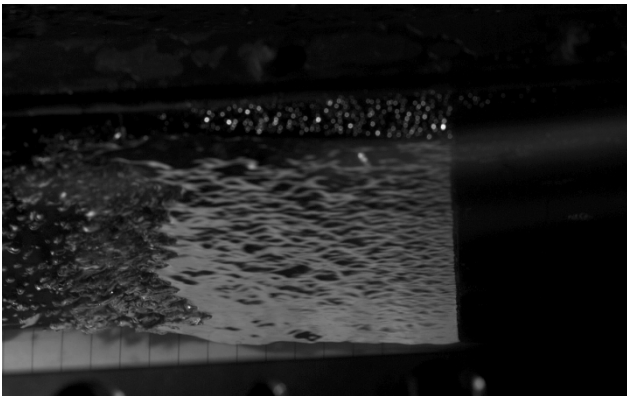
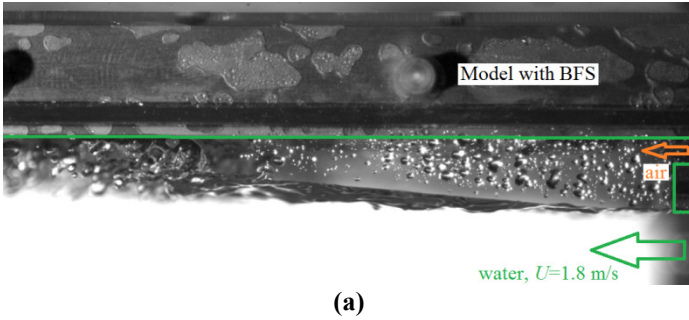


Figure 12. Cavity viewed from the side (a) and from below at an oblique angle (b).

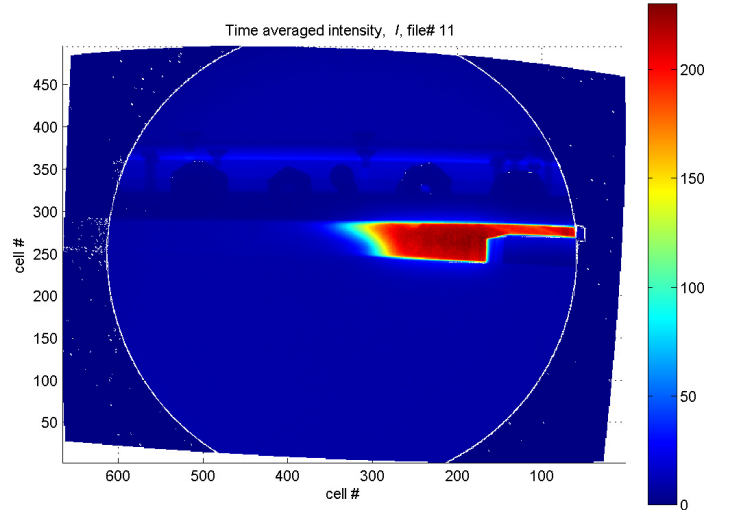


Figure 13. Time averaged light intensity field from a movie recorded at 4000 fps.

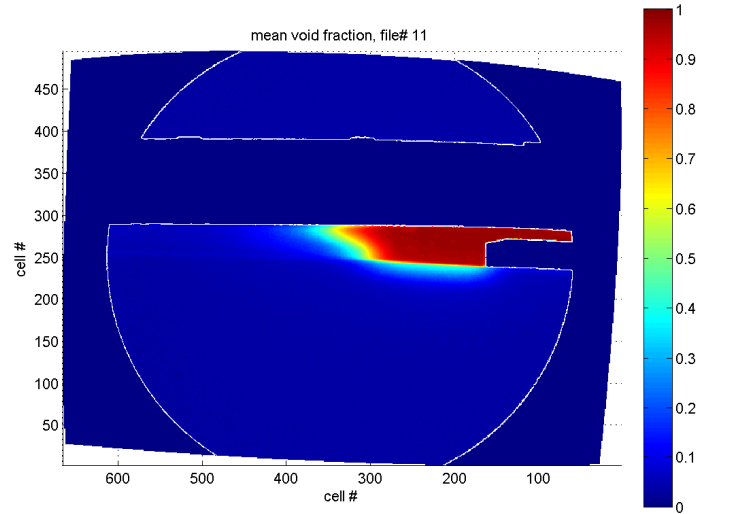


Figure 14. Time averaged void fraction calculated from the data presented in image 13, and from the reference images taken with void fractions zero and one.

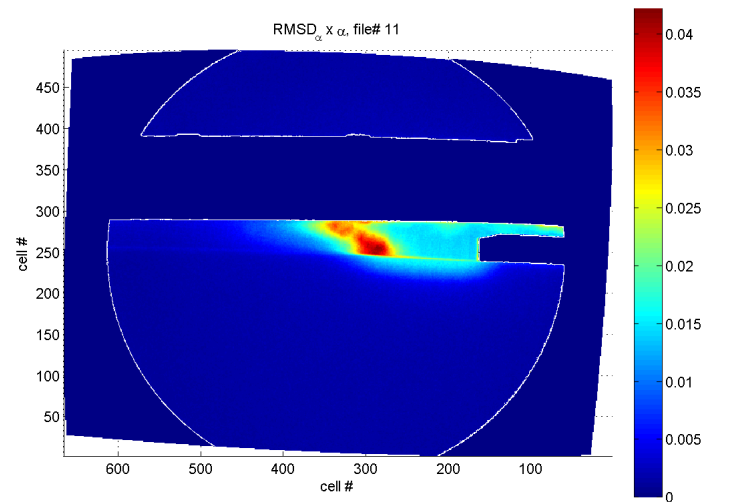


Figure 15. The root mean square deviation of the void fraction weighted by the mean void fraction to highlight the area of large fluctuation with significant void fractions.

Figures 13, 14, and 15 present the dewarped X-ray images of the air cavity. Figure 13 presents the 8-bit grey-scale of the measured intensity, and Figure 14 presents the final void fraction data. Figure 15 shows the RMS fluctuations in instantaneous void fraction weighted by the void fraction, which highlight the cavity closure as the region of large fluctuations. These data illustrate some of the capability of the current system. The temporal and spatial resolution of the system is sufficient to study cavitating flows, and the presence of re-entrant jets [20] and frequency of cloud shedding will be investigated next.

CONCLUSIONS

An X-ray densitometry system capable of spatially and temporally resolved void fraction measurements has been developed. The present system can determine the time-evolution of the volume fraction that is averaged across nominally two-dimensional flows. The measured void fraction was validated against known reference object, and the uncertainty of the time averaged void fraction is within 1.5%. We are currently developing improved dewarping and deconvolution schemes. In upcoming experiments, void fraction measurements for bubbly flows will be validated against those from dual fiber optical probes and video imaging in a further effort of comparative validation.

ACKNOWLEDGMENTS

The research was sponsored by the Office of Naval Research under grant N00014-08-1-0215 Dr. L. P. Purtell, program manager.

REFERENCES

- [1] Brennen, C.E. *Cavitation and Bubble Dynamics* Oxford University Press, 1995.
- [2] Terentiev, A.G., Kirchner I.N. and Uhlman, J.S., *The hydrodynamics of Cavitating Flows* Backbone Publishing Company, 2011.
- [3] Ceccio, S.L. and George D. L. "A Review of Electrical Impedance Techniques for the Measurement of Multiphase Flows" *Journal of Fluids Engineering*, **118**(2), 391-399, 1996.
- [4] R. Van Der Welle, "Void fraction, bubble velocity and bubble size in two-phase flow", *Int. J. of Multiphase Flow*, **11**(3), 317-345, 1985.
- [5] Holder, D. *Electrical impedance tomography: methods, history, and applications* IOP publishing, 2005.
- [6] York, T.J. "Status of electrical tomography in industrial applications", *Electron. Imaging* **10**, 608, 2001.
- [7] Ceccio, S. L., "Quantitative Measurements in Multiphase Flows Using Gamma Densitometry Tomography and Electrical Impedance Tomography," *Keynote at Proc. 6th International Conference on Multiphase Flow- ICMF 2007*, Leipzig, 2007.
- [8] Tortora, P. R., Ceccio, S. L., O'Hern, T. J., Torczynski, J. R., and Trujillo, S. M. "Quantitative Measurement of Solids Distribution in Gas-Solid Riser Flows Using Electrical Impedance Tomography and Gamma Densitometry Tomography," *Int. J. of Multiphase Flow*, **32**(8), 972-995, 2006.
- [9] Stutz, B., and Legoupil, S., "X-ray measurements within unsteady cavitation" *Experiments in Fluids*, **35**, 130-138, 2003.
- [10] Coutier-Delgosha, O., Stutz, B., Vabre, A., and Legoupil, S., "Analysis of cavitating flow structure by experimental and numerical investigations" *J. of Fluid Mechanics*, **578**, 171 -222, 2007.
- [11] Hassan, W., Legoupil, S., Chambellan, D., and Barre, S., "Dynamic Localization of Vapor Fraction in Turbo pump Inducers by X-ray Tomography", *IEEE Transactions on Nuclear Science*, **55**(1), 656-661, 2008.
- [12] Aeschlimann, V., Barre, S., and Legoupil, S., "X-ray attenuation measurements in a cavitating mixing layer for instantaneous two-dimensional void ratio determination", *Phys. Fluids*, **23**, 055101, 2011
- [13] Hubers, J.L., Striegel, A.C., Heindel, T.J., Gray, J.N., Jensen, T.C., "X-ray computed tomography in large bubble columns", *Chem. Eng. Science*, **60**, 6124-6133, 2005.
- [14] Bieberle, M., Barthel, F., Menz, H.-J., Mayer, H.-J. and Hampel, U., "Ultrafast three-dimensional X-ray computed tomography", *Appl. Phys. Lett.* **98**, 034101, 2011.
- [15] Hubbell, J.H. and Seltzer, S.M., "Tables of X-ray Mass Attenuation Coefficients and Mass Energy-Absorption Coefficients from 1 keV to 20 MeV for Elements Z = 1 to 92 and 48 Additional Substances of Dosimetric Interest" NIST Standard Reference Database, NISTIR 5632, 1995.
- [16] Alles, J. and Mudde, R.F., "Beam hardening: Analytical considerations of the effective attenuation coefficient of X-ray tomography" *Med. Phys.*, **34**(7), 2882, 2007.
- [17] Cerveri, P., Forlani, C., Borghese, N.A., and Ferrigno G., "Distortion correction for X-ray intensifiers: Local unwarpong polynomials and RBF neural networks", *Am. Assoc. Phys. Med.*, **29**(8), 1759, 2002
- [18] Seibert, J.A. "X-ray Imaging Physics for Nuclear Medicine Technologists. Part 2: X-ray Interactions and Image Formation", *J. Nucl. Med. Technol.*, **33**(1), 3-18, 2005
- [19] Doebelin, E. *Measurement Systems* McGraw-Hill, 5th ed., 2003.
- [20] Callenaere, M., Franc, J.-P., Michel, J.-M. and Riondet, M., "The cavitation instability induced by the development of a re-entrant jet." *J. of Fluid Mechanics*, **444**, 223-256, 2001.

Collapse of spark-generated cavitation bubble near a solid wall

*Miloš Muller, Faculty of Mechanical Engineering,
Technical University of Liberec
Studentská 2, 461 17 Liberec, Czech Republic

Patrik Zima, Department of Thermodynamics,
Institute of Thermomechanics, v. v. i., Academy of
Sciences of the Czech Republic
Dolejšková 1402/5, 182 00 Praha, Czech
Republic

*milos.muller@tul.cz

ABSTRACT

The article presents experimental results of the optical and acoustical study of cavitation bubble collapse close to a solid boundary in water. The bubble was generated by discharge of low-voltage capacitor into a couple of wires closing a simple circuit. Three different distances from the solid wall were studied. The bubble radius was studied using time-resolved photography and by PVDF hydrophone submerged in the glass bath representing the solid wall. The illumination was provided by high-power led diode. The synchronization of the system was provided by pulse generator connected to an oscilloscope. The impact power of the bubble to the wall was estimated from the time-resolved photography of the bubble jet and from the hydrophone signal. The hydrophone calibration was performed by a pendulum test to estimate the impact energy.

NOMENCLATURE

Impact force - F_i
Gravity acceleration - g
Elevation of the pendulum before impact - h_1
Elevation of the pendulum after impact - h_2
Initial position of the bubble - h_0
Mass of the pendulum - m
Pressure of the liquid in far field - p_∞
Vapor pressure of the liquid - p_v
Vertical bubble radius - R_v
Horizontal bubble radius - R_h
Maximum bubble radius - R_{max}
Velocity before impact - v_1
Velocity after impact - v_2
Initial bubble radius to initial bubble position ration - γ_0
Bubble collapse time - τ_c
Impact time - τ
Density of the liquid - ρ_l

1. INTRODUCTION

Understanding the collapse of a single cavitation bubble is essential to a number of fields including medical, marine or pump industries. Several techniques are commonly used for laboratory production of a single bubble. These include laser induction [1-2], spark generation [3-6] and acoustic generation [7]. The investigation of laser-induced bubbles and the

accompanying shock waves was invoked by the massive utilization of lasers in medical applications [2]. The spark-generated bubbles are often used to study underwater explosions [3]. Typically, they are produced by high voltage, however, one can use low voltage [6] providing that the electrodes are in direct contact. The authors' intention is to study bubbles for hydrodynamic applications, namely collapse of hydrodynamic cavitation bubble at different distances from the wall including the zero distance from the wall. For this purpose, an experimental setup utilizing generation of bubbles in a heated channel is being developed. Such method is not new, see for example [8], however, it requires another source to initialize the bubble collapse. Therefore, for the purpose of this early study, a proven setup with spark-generated bubbles will be used.

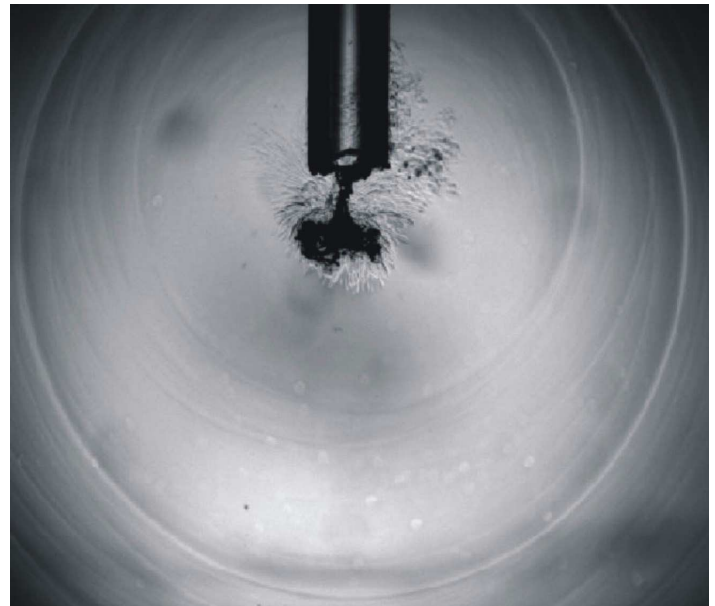


Figure 1. Laser induced bubble collapsing close to the optical fiber

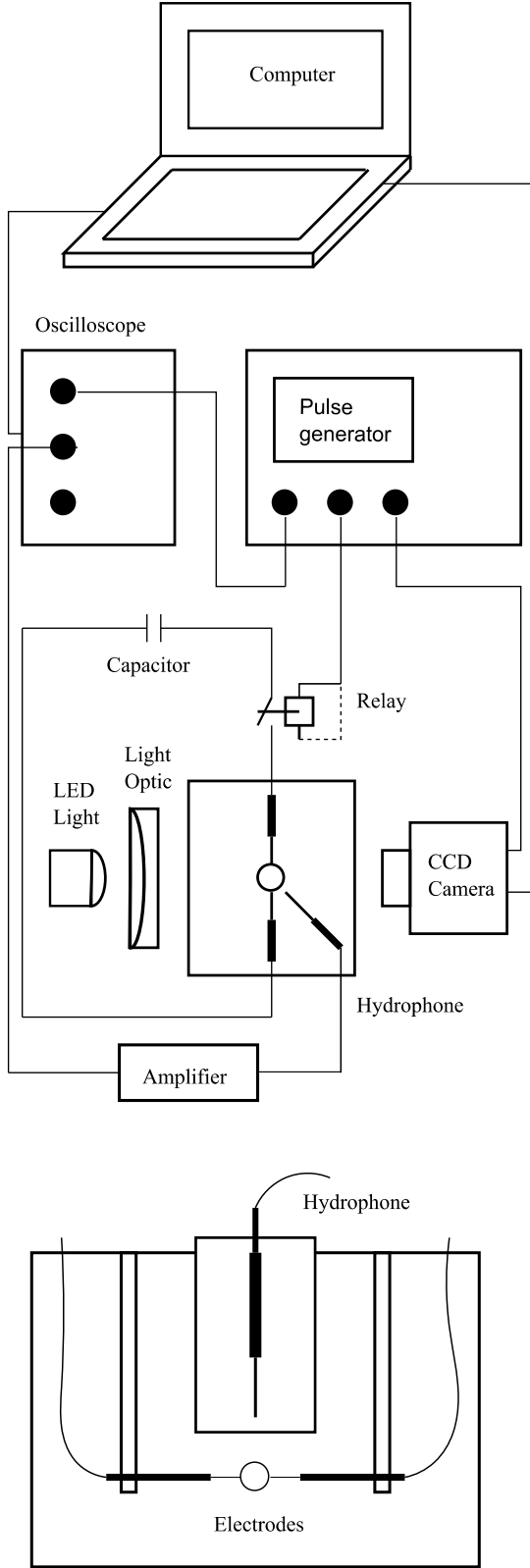


Figure 2. Experimental setup

It is known from the theory [9-10] that the bubble oscillations are strongly influenced by the presence of the wall. The bubble is attracted to the wall during the collapse causing damage to the wall material. The damage is caused by several

well-known effects: rapid re-entrant liquid micro jet (Figure 1), strong shock wave, the so-called splashing effect or combined action of these and other (for example electrochemical) effects.

We are focused on the impact force of the bubble re-entrant jet. This quantity can be calculated from the jet velocity and diameter using the time-resolved photography. The shock wave pressure load can be measured using a sensitive hydrophone placed close to the collapsing bubble.

2. EXPERIMENTAL SETUP

Figure 2 shows the experimental setup for investigation of a single spark-generated cavitation bubble. The bubble is created between two copper electrodes placed in a glass bath filled with tap water. The electrodes are in direct contact to enable the use of low voltage. The spark is produced by two parallel capacitors (60V, 4700 μ F), which are discharged through a relay. The temporal evolution of the bubble radius is recorded by the high-speed Redlake Motion Pro CCD camera with 10000 fps for all experiments. The illumination of the experiment is provided by the power led diode. To record the pressure response during the bubble collapse a PVDF hydrophone (RP acoustic type-s) connected to an preamplifier is used. The signals are digitalized using the oscilloscopic card with the sampling frequency 10 Mhz. The hydrophone with the sensitivity is 2.9 mV/bar can be used for frequencies up to 100 kHz. To avoid any damage the hydrophone is placed in a movable glass bath, which also represents the solid wall. The system is synchronized by the signal generator.

The calibration of the hydrophone is provided using the pendulum. The schematic illustration of the calibration test is shown in Figure 3.

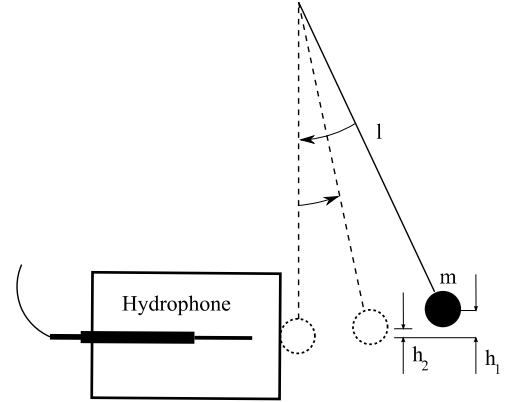


Figure 3. Hydrophone calibration

The impact force of the pendulum can be estimated from the following equation

$$F_i = \frac{m}{\tau} (v_1 - v_2) \quad (1)$$

where m is the mass of the sphere τ is impact duration time and v_1 and v_2 are the velocities just before and just after impact, which can be calculated from starting angle and angle after the impact as

$$v_{1,2} = \sqrt{2gh_{1,2}} \quad (2)$$

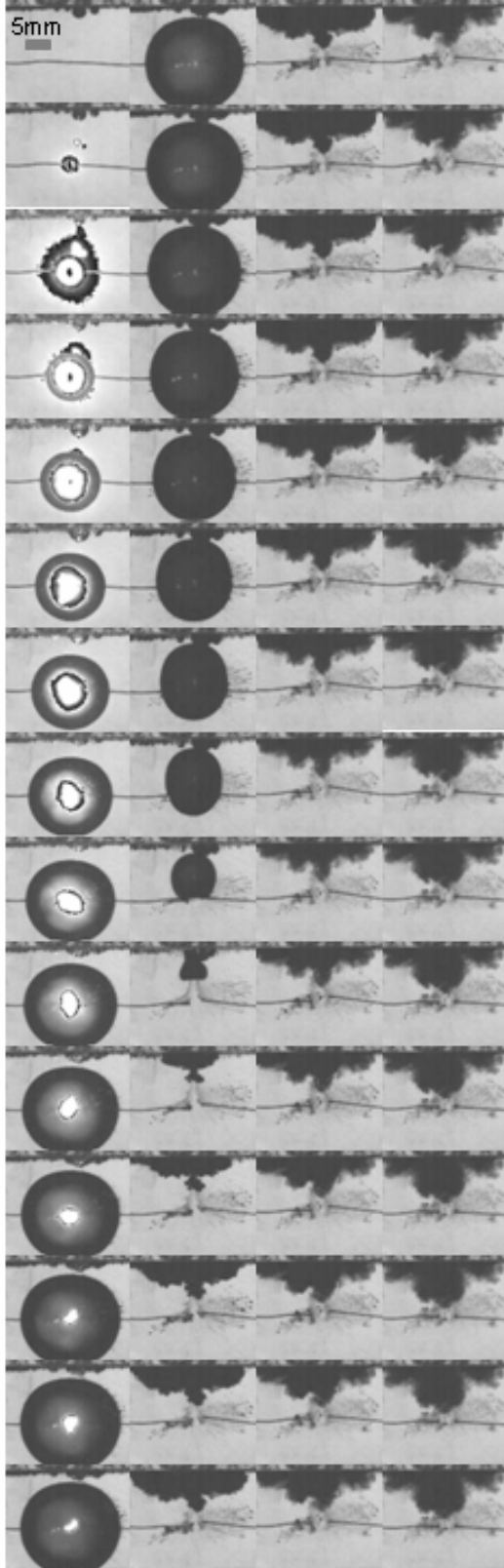


Figure 4. Cavitation bubble collapsing close to a solid boundary. The exposure is 5 μ s, the time delay between frames is 100 μ s. The first frame starts at 41 μ s, $\gamma_0=1.0$

The parameters were estimated from the-time resolved photography as $h_1=7.1$ mm, $h_2=6$ mm and the impact time was

set according to the hydrophone signal to 70 milliseconds. The corresponding force was calculated as 12,7 N corresponding to the peak voltage 45 mV. It is necessary to mention that the hydrophone signal does not correspond directly to the wall response as the hydrophone is not connected to the wall.

3. RESULTS

Figure 4, Figure 6 and Figure 7 show a typical history of the bubble collapse close to a solid boundary from our experiment. The corresponding hydrophone signal is shown in Figure 5. The bubble expansion starts at time 4.1 milliseconds, which corresponds to the relay delay time. The burst on the third figure is caused by the camera overexposure. After the plasma creation the bubble starts to grow. The first radius asymmetry is visible after the bubble starts to collapse. The first collapse produces a strong impact against the solid wall, which is visible in the hydrophone signal in Figure 5. The second collapse is followed, however, it is only visible from the hydrophone signal. Note that the signal in Figure 5 is smoothed and the full signal is shown in Figure 8, where the peaks due to the collision with the bubble wall are visible. The comparison of the bubble collapses for different values of parameter γ_0 are given in Figure 9. The parameter is defined as

$$\gamma_0 = \frac{h_0}{R_{max}}, \quad (3)$$

where h_0 is the initial position of the bubble from the solid surface and R_{max} is the maximum bubble radius.

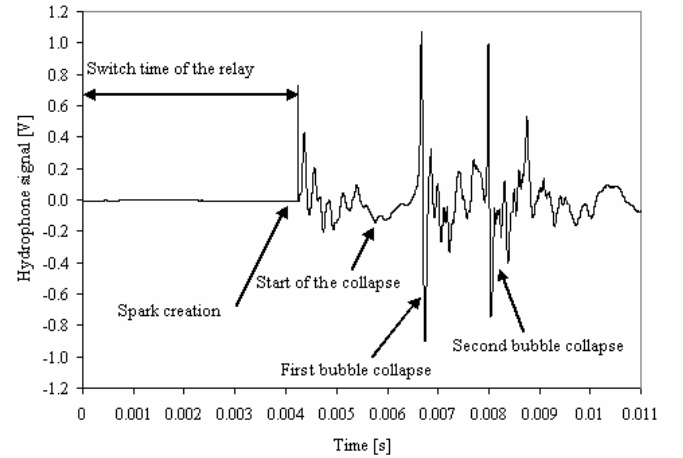


Figure 5. Hydrophone signal of bubble collapse (with 10 kHz low-pass filter applied).

Figure 5 allows us to observe the different times required for the bubble growth and the bubble collapse. It is possible to calculate the bubble collapse time from relation [9]

$$\tau_c = 0.915 \sqrt{\frac{\rho_l}{p_\infty - p_v}} R_{max}, \quad (4)$$

where ρ_l is density of the liquid p_∞ is the pressure in the far field in the liquid, p_v is the vapour pressure of the liquid and R_{max} is

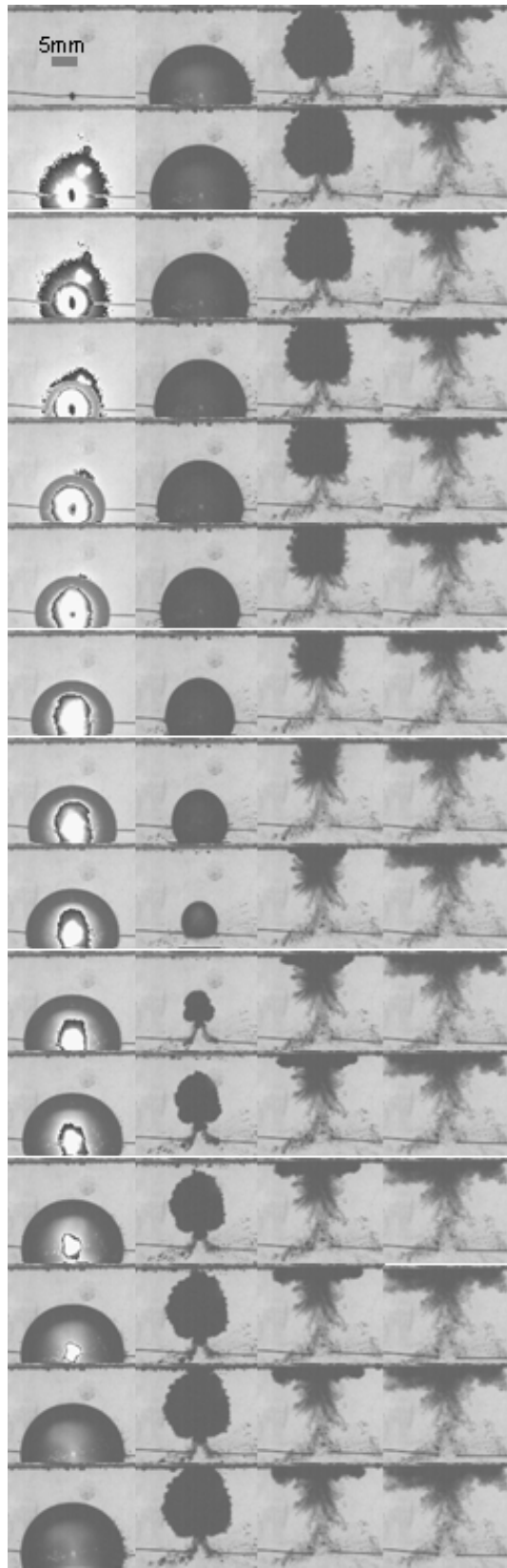


Figure 6. Cavitation bubble collapsing close to a solid boundary.
The exposure is $5\ \mu\text{s}$, the time delay between frames is $100\ \mu\text{s}$.
The first frame starts at $41\ \mu\text{s}$, $\gamma_0=0.64$.

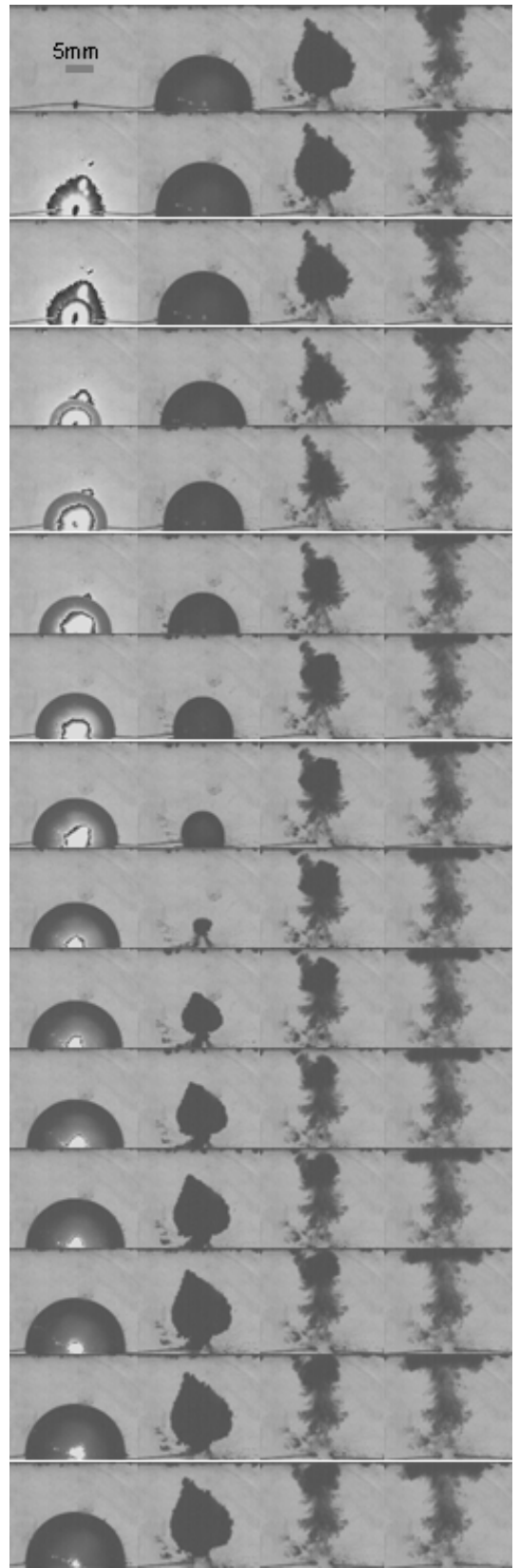


Figure 7. Cavitation bubble collapsing close to a solid boundary.
The exposure is $5\ \mu\text{s}$, the time delay between frames is $100\ \mu\text{s}$.
The first frame starts at $41\ \mu\text{s}$, $\gamma_0=0.52$.

the maximum bubble radius. The other parameters were set to $\rho_l = 998 \text{ kg/m}^3$, $p_\infty = 1 \text{ bar}$, and $p_v = 2339 \text{ Pa}$. The corresponding collapse time and the maximum bubble radii are given in Table 1. The table shows that the vertical bubble radius is slightly influenced by the wall. The curves of the bubble radius are not symmetric, which is most likely caused by the plasma expansion, i.e. by the duration of the electric pulse.

Bubble position		Collapse time [s]	Maximum bubble radius [m]
$\gamma_0=1.0$	horizontal	0.00088	0.00950
	vertical	0.00083	0.00900
$\gamma_0=0.64$	horizontal	0.00091	0.00980
	vertical	0.00091	0.00980
$\gamma_0=0.52$	horizontal	0.00087	0.00940
	vertical	0.00094	0.01020

Table 1. Maximum bubble radius vs. collapse time

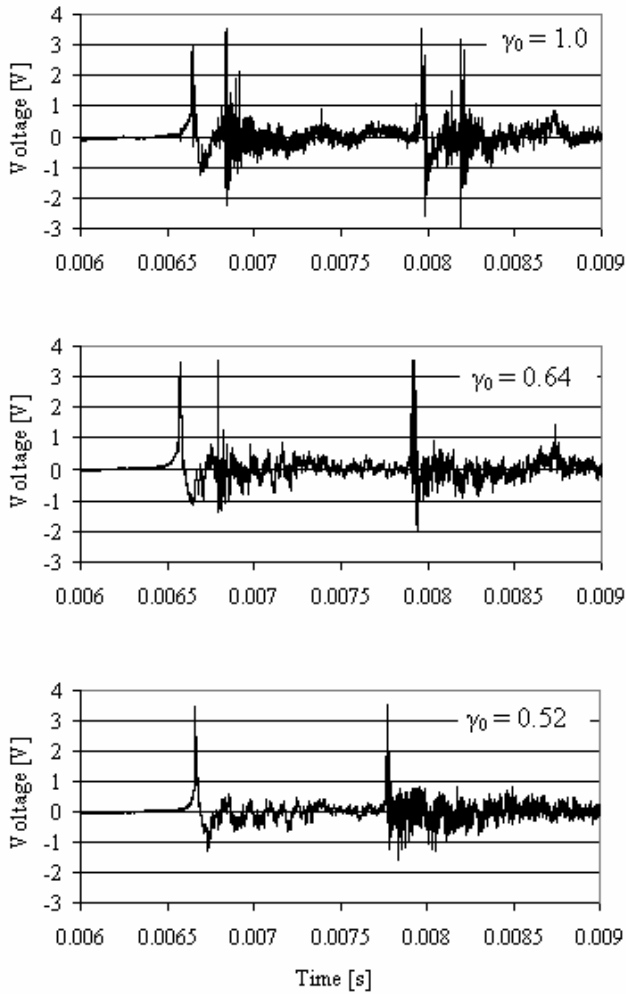


Figure 8. Hydrophone signals for different values of γ_0 .

It is also visible that the bubble far from the wall is collapsed faster. The interaction with the bubble wall is demonstrated in

the hydrophone signal by the secondary peak after each collapse. The first peak likely corresponds to the shock wave produced during the collapse. This is most significant for $\gamma_0 = 1.0$ where the bubble is in close contact with the wall. For $\gamma_0 = 0.64$ only one peak corresponding to the jet-to-wall interaction is visible. No interaction with the bubble wall is evident for $\gamma_0 = 0.54$. From the hydrophone signal we can roughly estimate the force of the micro-jet acting on the wall. For the peak voltage 3.5 V we can calculate, based on the calibration data, the force 988 N. However, the real force is likely to be higher than the estimated one as the hydrophone is placed far in a separated chamber. One can expect that estimating the force from the average voltage would lead to lower estimated values.

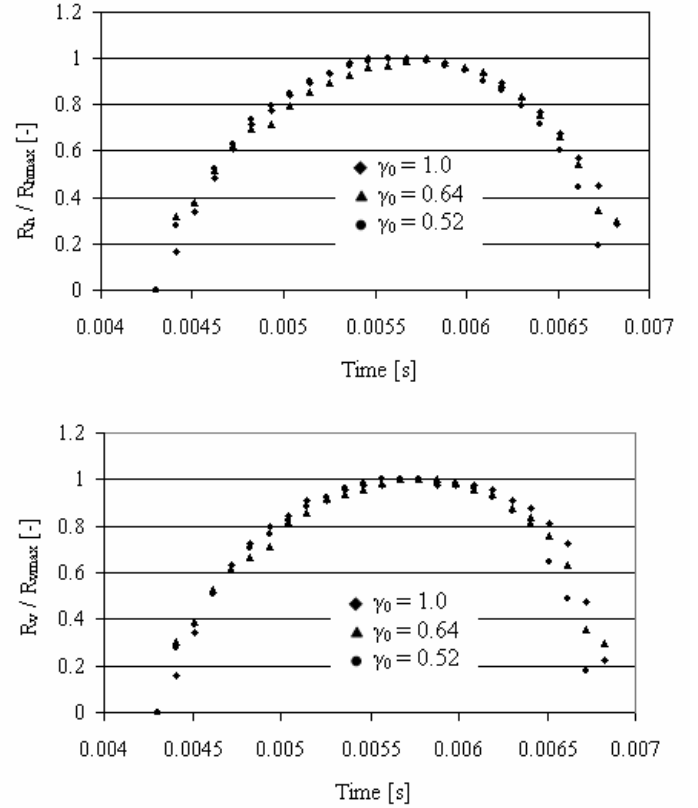


Figure 9. Time evaluation of vertical and horizontal bubble radius.

CONCLUSION

The spark-generated cavitation bubble collapse was investigated optically and acoustically. The interaction of the two methods in the time domain allows us to identify the response of the individual processes involved in the collapse. The bubble generation based on the low-voltage spark seems acceptable for this stage of experiment. In the investigated range of the bubble positions, we have observed strong influence of the wall. When the bubble collapses directly on the wall the impact force by the bubble jet is considerable. In the position far from the wall the shock wave effect is dominant. The estimation of the bubble collapse force using the hydrophone separated from the wall does not take into account possible dissipation of energy into the wall structure.

ACKNOWLEDGMENTS

The authors wish to thank the Czech Science Foundation for providing financial support for grant no. 101/10/1428 and the Ministry of Education, Youth and Sports for providing financial support to the Technical University of Liberec under grant no. MSM 4674788501.

REFERENCES

- [1] Lauterborn, W. and Bolle, H., 1975, "Experimental investigations of cavitation-bubble collapse in the neighborhood of a solid boundary," *J. Fluid Mech.*, 72, 391-399.
- [2] Vogel, A., Lauterborn, W., Timm, R., 1989, "Optical and acoustic investigations of the dynamics of laser-produced cavitation bubbles near a solid boundary," *J Fluid Mech.*, 206, 299-338.
- [3] Chahine, G. L., G.S. Frederick, C. J. Lambrecht, G. S. Harris, and H. U. Mair., 1995, "Spark-Generated Bubbles as Laboratory-Scale Models of Underwater Explosions and their Use for Validation of Simulation Tools," in Proceedings of the 66th Shock and Vibrations Symposium, November, 1995. Biloxi, MS.
- [4] Buogo, S., Plocek, J., Vokurka, K., 2009, "Efficiency of Energy Conversion in Underwater Spark Discharges and Associated Bubble Oscillations: Experimental Results," *Acta Acustica united with Acustica*, 95, 46-59.
- [5] Wang, Y. C., Chen, Y. W., 2007, 'Application of piezoelectric PVDF film to the measurement of impulsive forces generated by cavitation bubble collapse near a solid boundary,' *Exp. Thermal Fluid Sci.*, 322, 403-414.
- [6] Lew, K. S. F., Klaseboer E., Khoo, B. C., 2007, "A collapsing bubble-induced micropump: an experimental study," *Sensors Actuat. A*, 133, 161-172.
- [7] Lauterborn, W., Kurz, T., Geisler, R., Schanz, D., Lindau, O., 2007, "Acoustic cavitation, bubble dynamics and sonoluminescence," *Ultrasonics Sonochemistry*, 14, 484-491
- [8] Helden, W., Geld, C., Boot, P., 1995, "Forces on bubbles growing and detaching in flow along a vertical wall," *Int. J. Heat Mass Transfer*, 38, 2075-2088.
- [9] Brennen, C. E., *Cavitation and Bubble Dynamics*, 1995, Oxford University Press, New York, NY
- [10] Franc, J. P. and Michel J. M., 2004, *Fundamentals of Cavitation*, Kluwer Academic Publisher

Mercury cavitation and its mitigation technique for high power pulse spallation neutron sources

Masatoshi Futakawa*/Japan Atomic Energy Agency

Takashi Naoe/Japan Atomic Energy Agency

Hiroyuki Kogawa/Japan Atomic Energy Agency

Takashi Wakui/Japan Atomic Energy Agency

Katsuhiro Haga/Japan Atomic Energy Agency

* futakawa.masatoshi@jaea.go.jp

ABSTRACT

Innovative researches using neutrons will be performed at MLF (Materials & Life science experimental Facility) in J-PARC (Japan Proton Accelerator Research Complex), in which a mercury target system is installed as a MW-class pulse spallation neutron source. In order to produce neutrons by the spallation reaction, proton beams are injected into a mercury target. At the moment when the intense proton beam hits the target, pressure waves are generated in the mercury because of the abrupt heat deposition. The pressure waves interact with the target vessel leading to negative pressures that may cause cavitation along the vessel wall. Localized impacts by micro-jets and/or shock waves that are caused by cavitation bubble collapse impose pitting damage on the vessel wall. The pitting damage that degrades the structural integrity of target vessels is a crucial issue for the high power mercury targets. Therefore, the mitigation techniques for the pitting damages and cavitation are needed to realize the MW-class pulsed spallation neutron sources.

So far, several techniques have been investigated from the viewpoints of improvement of the vessel materials and suppression of the pressure waves. In the paper, the R&D status on the cavitation mitigation technique for the high power spallation neutron source will be introduced.

1. INTRODUCTION

Neutrons are used for the innovative research that will bring about breakthrough in scientific and engineering research fields, i.e. fuel cell, hydrogen embrittlement, protein structure, medicine, etc. Mercury is available as target materials to produce neutrons by spallation reaction that is occurred by the bombardment in mercury with high-energy protons. The pulsed spallation neutron sources are being operated at the J-PARC in Japan [1] and SNS in US [2], which are standing on the way to increase the power up to MW-class. However, the higher the power, the severer the mercury cavitation problems become. In fact, in the SNS, many penetrating pits due to cavitation were found at the inner wall in the first target vessel that was replaced in 2009.

At the moment that the protons bombard in the mercury, thermal shock is generated in the mercury and the pressure waves are induced [3,4]. On the process of the pressure wave propagation aggressive cavitation generates in the mercury, which imposes damage on the solid wall of the target vessel [5-7]. Therefore, the cavitation phenomenon gets to be a crucial issue to increase the power in the mercury target for the pulsed spallation neutron sources. Through theoretical and experimental investigations, we could understand the relationship between pressure wave conditions, mercury cavitation aggressiveness and damage growth behaviours on some solid materials [8].

As for the damage mitigation, two approaches are applied: protection of the vessel wall and suppression of the pressure waves. The protection methods are mainly divided into two kinds: hardening vessel-wall and gas layer protections. The hardening protections are coatings and/or surface improvements: Kolestrising®, nitriding, etc [9,10]. The gas-layer protection is to form a gas curtain along the interface between the vessel wall and the mercury.

On the other hand, an optimization of beam profile to decrease in the peak heat density in the mercury and a microbubbles injection that can soften mercury are effective from the viewpoint of pressure wave suppression. The bubbling condition suitable for the pressure reduction was theoretically predicted: the diameter of bubbles is less than 100 μm and the void fraction larger than 10^{-3} [11,12]. Indeed it was not easy to make microbubbles in mercury because of its high surface tension, high density, low wettability, etc. Therefore, an innovative microbubbler, a so-called swirl bubbler, was developed to inject microbubbles into flowing mercury. We experimentally confirmed the effectiveness to reduce the cavitation damage by microbubbles [13,14].

In this paper R&D status on mitigation technique for cavitation in the mercury target for the spallation neutron sources will be described.

2. PRESSURE WAVES IN MERCURY TARGET

Mercury, which has high atomic number and is liquid at room temperature, has the benefits for pulse spallation neutron sources because of the high neutron yielding efficiency and

usage as a coolant. In the MLF, the mercury target system consists of a target vessel and a mercury circulator, which are installed on the target trolley. Figure 1 shows the target vessel for the spallation neutron source at the MLF. The target vessel is filled with the mercury circulating at ca.1m/s as flowing along by the beam window. The spallation reaction is induced when accelerated protons (1 MW, 3 GeV, 25 Hz, and 1 μ s pulse duration) are bombarded in mercury and approximately a half of the power is dissipated for rapidly heating in the mercury [15,16]. As a result, thermal shock occurs and generates the pressure waves in the mercury. Temperature rising ΔT in the mercury is given by

$$\Delta T = \frac{\Delta Q}{\rho c_v} \quad (1)$$

where T is temperature, Q is heat density, c_v is specific heat capacity, ρ is density of mercury.

Pressure rising ΔP is given by

$$\Delta P = \beta_p K_T \Delta T \quad (2)$$

where P is pressure, β_p is thermal expansion, K_T is bulk modulus.

Nuclear heat distributions ΔQ in the mercury target is very dependent on the proton beam profiles and the maximum peak pressure attributes to a peak heat deposition of beam profile. In order to investigate the pressure propagation and the dependency of pressure waves on the beam profiles, FEM analyses were carried out using an explicit code LS-DYNA. The cut-off pressure model is applied to mercury to simulate the mercury failure due to cavitation [16,17]. In the cut-off pressure model, a relationship between volumetric strain and pressure is linear elastic when pressure larger than a certain value (the cut-off pressure), but the mercury has no stiffness when the pressure is less than it. We used the cut-off pressure of -0.15 MPa, whose suitability was confirmed experimentally. The boundary condition along the interface between solid wall and liquid mercury was tied.

Figure 2 shows the pressure time response in liquid mercury along the center axis in the proton beam injection

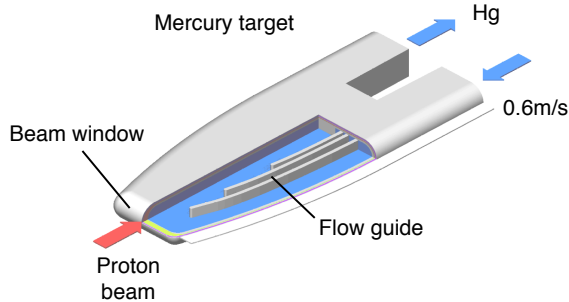
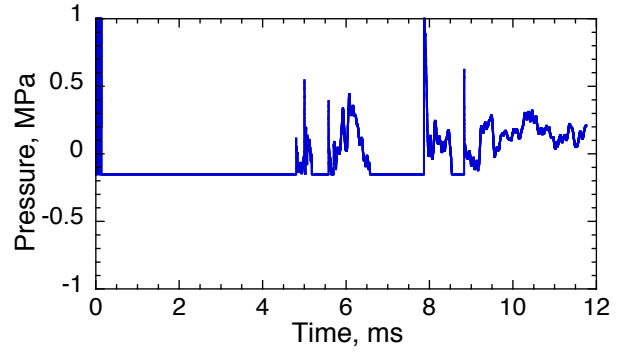
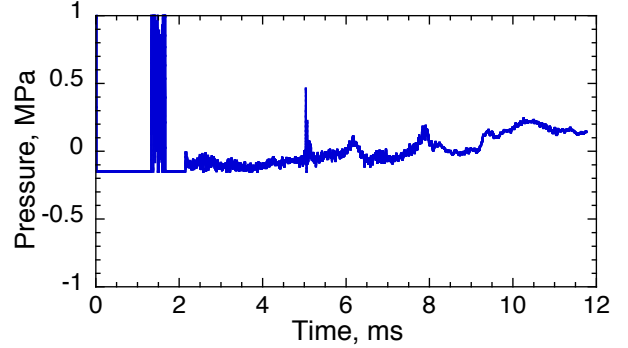


Figure 1 Mercury target at J-PARC. The drawing illustrates the inner wall of target vessel: i.e. the vessel consists of multi-wall structure to protect from the mercury leakage into the outside of vessel.



(a) Pressure waves nearby the beam window



(b) Pressure waves at the maximum heat deposited area

Figure 2 Time-responses of pressure waves in mercury target

direction in the target vessel under 1 MW power at J-PARC. Nearby the window, the longest period of negative pressure is 5 ms approximately, and after 8 ms the pressure increases gradually as shown in Fig.2 (a). At the maximum heat deposited area, the negative pressure imposing time is shorter than that nearby the beam window as shown in Fig.2(b). The negative pressure with a relatively long period is induced by the interaction between the solid wall and the liquid mercury.

The damage is dependent on the cavitation bubble growth and collapse behaviors, i.e. cavitation intensity, which are affected by the pressure wave time-response. The cavitation inception is not dependent on the compressive pressure itself, and needs a certain negative pressure to grow the cavitation bubbles. In the macroscopic view, it can be said that the liquid failed at the pressure lower than a critical tensile pressure to induce the cavitation bubbles, i.e. so-called the Blake threshold, which is equivalent to the cut-off pressure used in the pressure wave propagation analysis in the target [17]. The period of negative pressure, therefore, seems to be one of crucial factors related with the cavitation intensity. The relationship between bubble growth behavior and pressure waves was investigated by using Rayleigh-Plesset equation [13]. The negative pressure period in the mercury target vessel is several ms order that seems mostly attribute to the cavitation damage (Later we will discuss in detailed).

3. CAVITATION DAMAGE BY PRESSURE WAVES

The cavitation damage formation due to pressure waves was systematically investigated under mechanically pressurized mercury [18]. The electric-Magnetic Impact Testing Machine, MIMTM was developed for the purposes [8]. The impulsive pressure was imposed repeatedly on mercury through a diaphragm. The pressure was controlled precisely by the input electric power. The repeated frequency of pulses, f , was 25 Hz constant. The negative pressure period associated with the input power was approximately 2 ms in maximum, which is an equivalent order as the numerically estimated period in the mercury target, as shown in Fig.3. The negative pressure periods are ca. 1 ms at 560 W in MIMTM. Figure 4 shows the damaged surface at type 316 stainless steel that is used for the target vessel after 10^3 and 10^6 impact cycles under 560 W of the input electric power, respectively. The damage at 10^3 is categorized into the damage in an incubation period without mass-loss, dominated by mezosopic localized plastic deformation, so-called pits. The pits covered on all of surface at 10^6 cycles and the mass-loss occurred with cracking on the surface. The so-called steady state involving mass-loss started at 10^6 cycles. It notes that the mass-loss commenced after the fractions of the damaged surface to the observed surface becomes 1: i.e. the fractions are 0.5 at 10^3 impact cycles and 1 at 10^6 , which were estimated from the surface observation shown in Fig.4.

The erosion estimation in the steady state for various cavitations and materials was proposed by Futakawa and Soyama [8,18,19], based on experimental results, as shown in Fig.5. The cavitation conditions are a water jet, a vibraphone in water and mercury and the MIMTM in mercury. Here, the number of pulses was transformed to the imposing time T by using $T=Nx(I/f)$ to compare with the water jet erosion. As a result, it was found that the accumulated damage in the steady state was predicted by using the following equation:

$$MDE = C_1 T^B \text{ or } = C_1 N^B, \quad (3)$$

where MDE is the mean depth of erosion that evaluated by the mass-loss, T or N is the imposing time or the number of pulses, C_1 is a constant depending on loading condition, i.e. impulsive pressure response, etc., which is associated with the incubation period. Interestingly, it was recognized from Fig.5 using normalized values for MED and T or N that B is 1.3 independently of materials and cavitation conditions. Therefore, if the incubation period is known, the cavitation damage is predicted by using Eq.(3). The incubation period is dependent on the cavitation intensity.

The cavitation intensity is affected by the cavitation bubble growth and collapse behavior. The cavitation inception and its bubble growth are very dependent on the negative pressure period and intensity. The cavitation bubble growth behavior was predicted by using Rayleigh-Plesset equation as following:

$$R\ddot{R} + \frac{3}{2}\dot{R}^2 = \frac{1}{\rho} \left[\left(P_0 + \frac{2\sigma}{R_0} - P_v \right) \left(\frac{R_0}{R} \right)^{3\gamma} + P_v - \frac{2\sigma}{R} - \frac{4\eta\dot{R}}{R} - P(t) \right] \quad (4)$$

where R is bubble radius, P is pressure, ρ is Density, η is viscosity, σ is surface tension, P_v is vapor pressure, R_0 is initial radius (here, $R_0 = 1\mu m$). $P(t)$ was given by the measured pressure

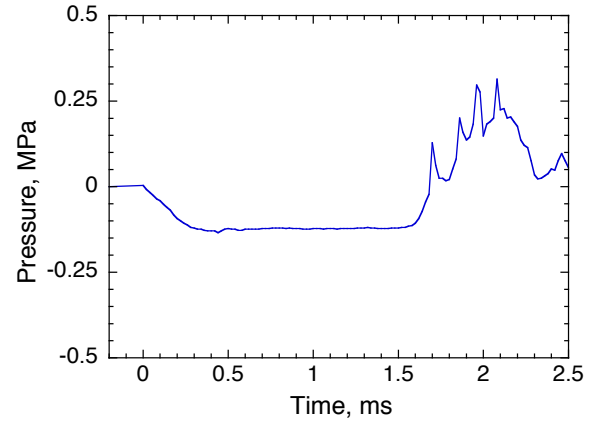


Figure 3 Time response of pressure at MIMTM experiment at 560 W input power

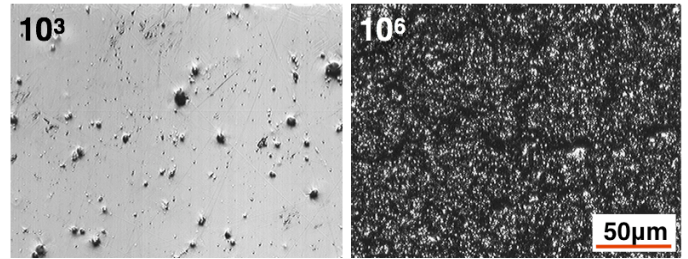


Figure 4 Mercury cavitation damage at 10^3 and 10^6 impact in MIMTM experiment, taken by laser microscope. The black area is occupied by erosion.

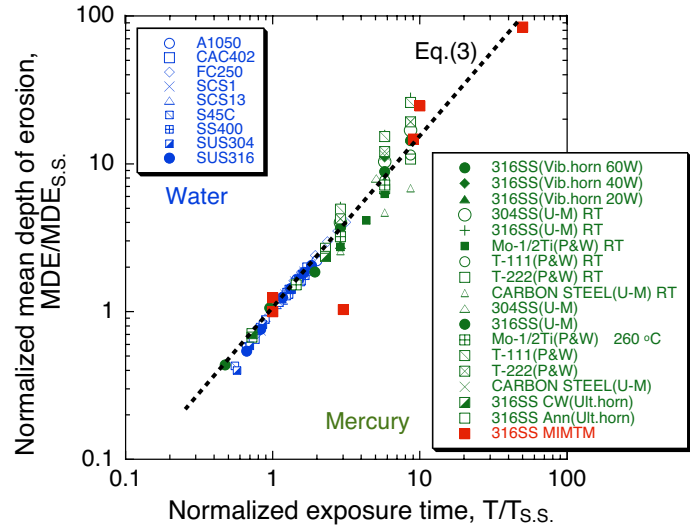


Figure 5 Mass loss behavior in the steady states for various cavitation. The line is given by Eq.(3).

in the MIMTM. The cavitation bubble growth behavior for the pressure responses measured for each power was calculated as shown in Fig.6. The bubble radius is growing during the negative pressure imposing period. Even after the positive

pressure imposing, the bubble continues growing by inertia and suddenly collapses. Figure 7 shows the relationship between R_{max}/R_0 and the incubation period that was experimentally obtained [8]. It is recognized from Fig.7 that the incubation period, T_i or N_i , is predicted by using

$$T_i = C_2 (R_{max}/R_0)^3 \text{ or } N_i = C_2 (R_{max}/R_0)^3 \quad (5)$$

$$\sim I_c$$

where C_2 is material constant. The cavitation intensity I_c is likely to be correlated with $(R_{max}/R_0)^3$, as well. This trend is quite understandable because the cavitation collapsing pressure is related to the third power of bubble radius [20].

The lifetime of the target vessel that is dominated by the cavitation damage on the beam window is evaluated by using these relationships given by Eqs. (3) and (5). We will discuss in more detailed in Section 5.

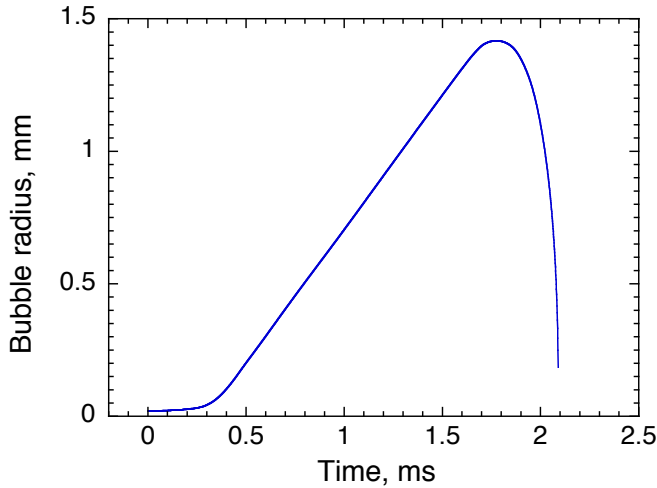


Figure 6 Cavitation bubble growth predicted by Rayleigh-Plesset with measured pressure responses at 560 W in the MIMTM.

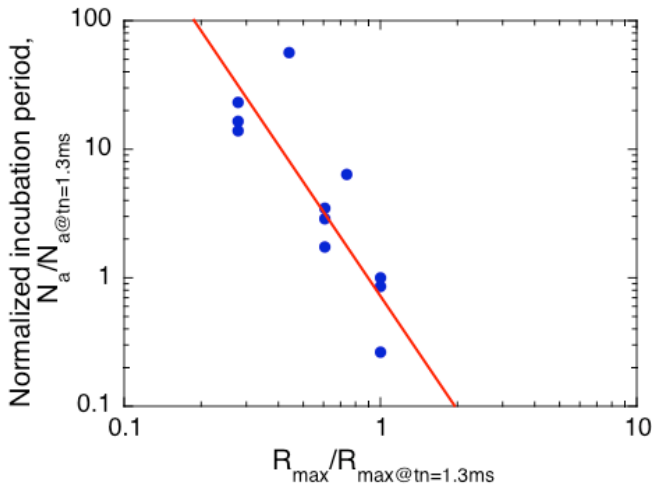


Figure 7 Relationship between incubation period and cavitation bubble radius. The line is given by $N=CR^3$

4. MITIGATION TECHNIQUES

4-1 Hardening material surface

We have investigated the damage mitigation methods from the viewpoint of two approaches: i.e. material and mercury sides. In the case of the material side, more than 20 kinds of surface improvements: coating, implantation, etc. were examined experimentally. As results, we developed an innovative surface treatment consisting of plasma carburizing and nitriding PNC, and the thickness of the improved surface was determined by the stress distribution along the interface between the substrate and the surface layer through impact analyses [10, 21].

It was deduced that the incubation period, an acceptable number of pulses without distinguished pitting damages might be extended by the treatment from 10^6 pulses to 10^7 pulses as shown in Fig.8 in the case of 560 W pulses in the MIMTM. This treatment was applied to the beam window of the first target vessel in the J-PARC.

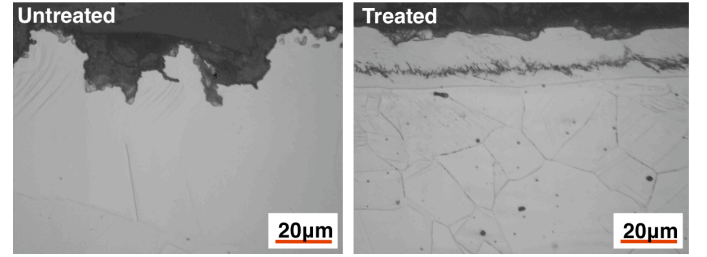


Figure 8 Effect of surface treatment on cavitation damage after 10^6 impacts at 560 W in the MIMTM.

4-2 Softening mercury

As the approach from mercury side, we are trying to inject microbubbles into the mercury to reduce the pressure waves and suppress the cavitation bubble growth [12,13]. The initial compressive pressure wave is reduced by absorption of the thermal expansion of mercury due to the contraction of microbubbles. The effect is expected at the heat deposited area and at the onset of pressure wave propagation. During the wave propagation, the microbubbles can reduce the amplitude of the compressive pressure waves through attenuation of the pressure waves due to the thermal dissipation of kinetic energy and the dispersion. The cavitation inception is not dependent on the

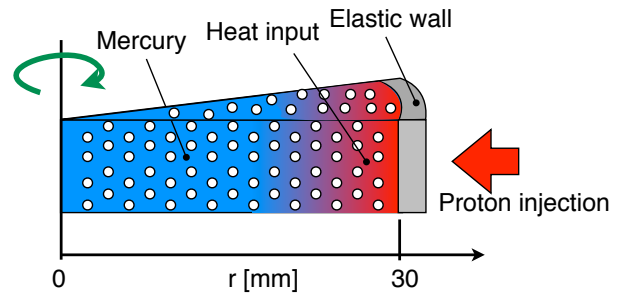


Figure 9 One dimensional axisymmetric propagation model in the PAC-MT

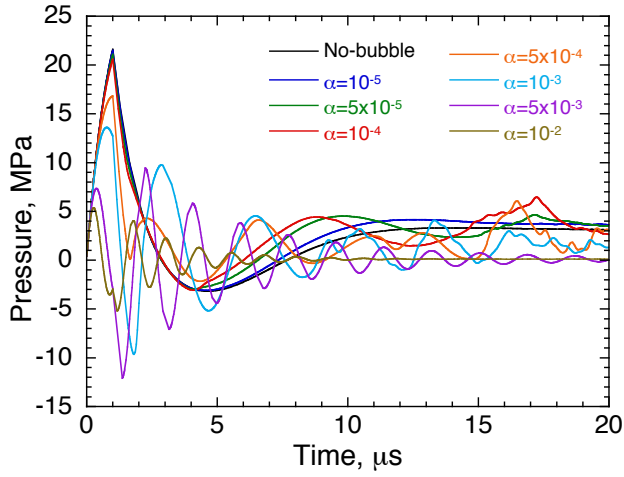
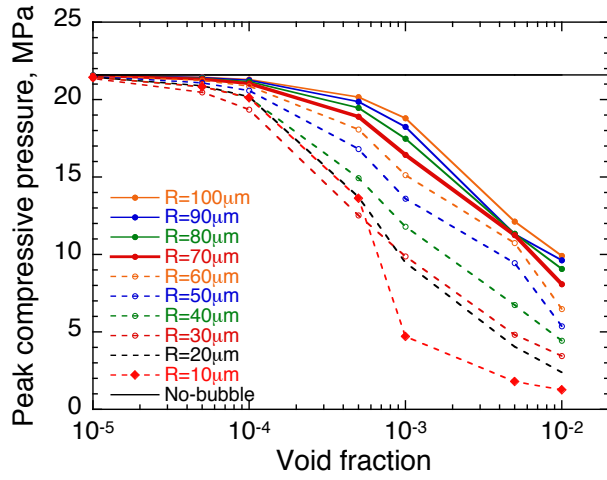
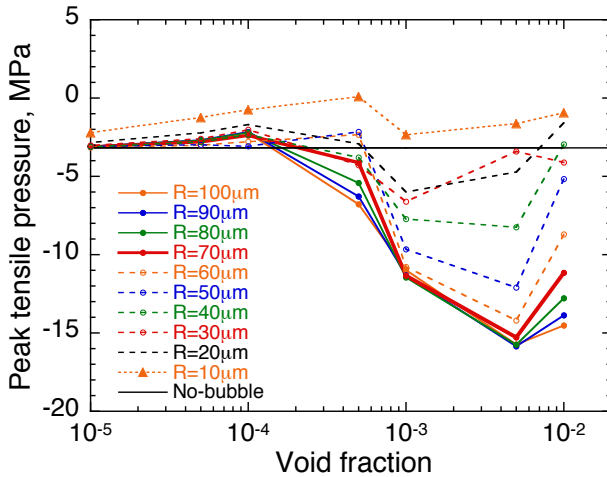


Figure 10 Time response of pressure waves in bubbly liquid mercury.



(a) Compressive pressure



(b) Negative pressure

Figure 11 Relationship between the void fraction and the peak values of compressive and negative pressures for each bubble size.

compressive pressure itself, and needs a certain negative pressure to grow the cavitation bubbles, i.e. so-called the Blake threshold. As assuming that the cavitation intensity is associated to the bubble size, the negative pressure period is essential to predict the damage. It is deduced numerically that the magnitude and period of the negative pressures resulting from the interaction between the intensive compressive pressure and the vessel wall and the inertia effect followed by the propagation of intensive compressive pressure waves are dependent on the beam power. On the other hand, the secondarily-induced negative pressure itself is likely to be mitigated by the attenuation due to microbubbles.

Okita et al developed the numerical simulation code PAC-MT to evaluate the microbubble condition to mitigate the pressure waves [12]. The model is one dimensional axisymmetric propagation model with elastic wall and heated area nearby the wall, which simulated the beam window of the target vessel, as illustrated in Fig.9. The pressure propagates from the heated area nearby the wall to the center through the gas liquid bubbly mixture. The energy conservation equation, the equation of state for liquid phase and the compressibility of liquid are considered. The heat transfer between the gas inside interface is considered to clarify the thermal damping effect for the bubble oscillation during the pressure propagation through the bubbly liquid. The gas inside bubbles is assumed to be noncondensable. The mass transfer through the gas-liquid interface such as evaporation, condensation and solution is not taken account. The stiffness and density of the elastic wall are equivalent to the beam window of 2.5 mm in thickness. The detailed model description is seen in ref. [12,22]. Here, the maximum heat density in Gaussian distribution is 12 J/cc, which was estimated by spallation neutron reaction for the mercury target at the J-PARC. The pulse duration was assumed as 1 μ s. The injected bubble size was assumed to be 50 μ m in radius since the bubbling element that we developed newly for the mercury target [23] can generate the bubbles and the void fraction is controlled by the gas flow rate through the element into flowing mercury. Figure 10 shows the time responses of the pressure waves. The mitigating effect is likely to be dependent on the void fraction.

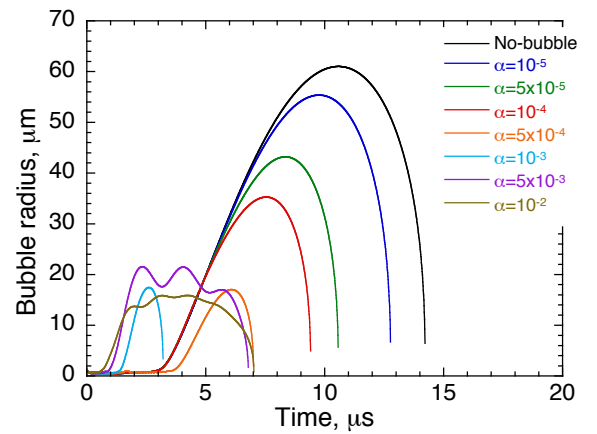


Figure 12 Cavitation bubble growth behaviour.

Figure 11 shows the relationship between the void fraction and the peak values of compressive and negative pressures. The peak pressures decrease clearly in the range more than 10^{-4} of void fraction. Then, it can be said that the mercury gets to be softened by microbubbles of $50\text{ }\mu\text{m}$ in radius with more than 10^{-4} of void fraction to absorb the thermal shock due

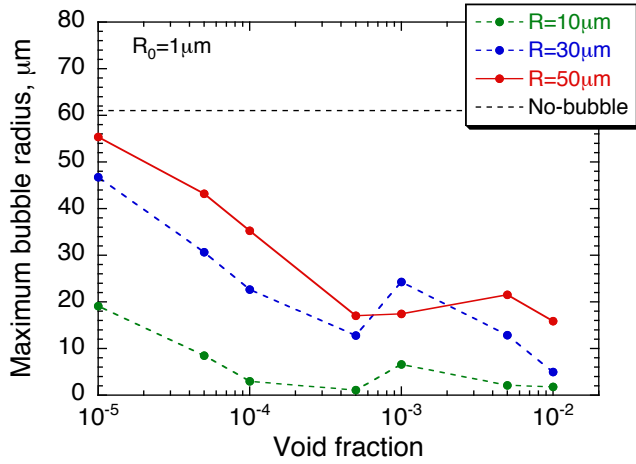


Figure 13 Relationship between the maximum radius of cavitation bubbles and the void fractions.

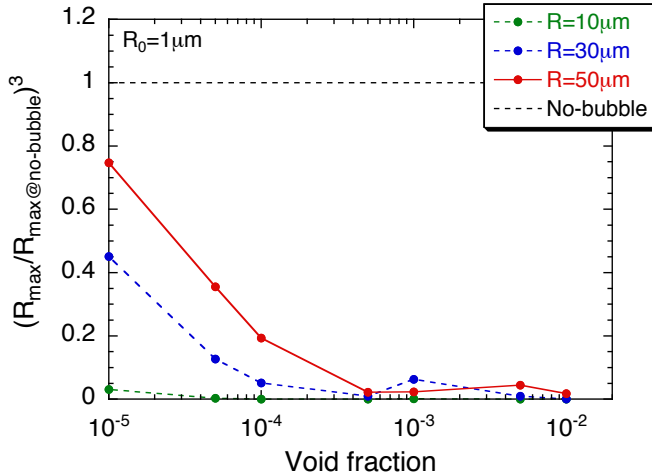


Figure 14 Relationship between cavitation intensity ($\sim R^3$), injected microbubble size and void fraction.

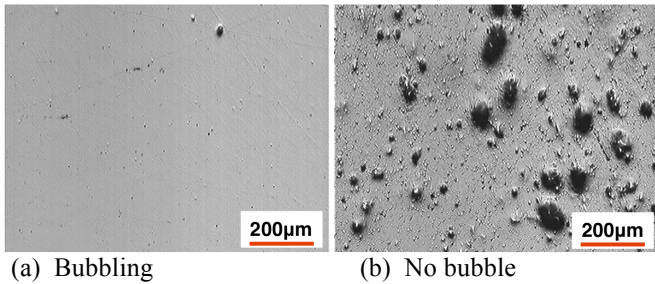


Figure 15 Effect of microbubbles on cavitation damage after 10^4 impacts at 560 W in the MIMTM.

to the proton bombarding. On the contrary, the amplitude of negative pressure increased beyond 10^{-4} of void fraction.

As mentioned in the previous section, the cavitation intensity is likely to be related with the cavitation bubble size, which is affected by negative pressure period rather than the peak value. Therefore, the effect of microbubble injection on the cavitation bubble growth was investigated by using Rayleigh-Plesset Eq.(4), where $P(t)$ is the pressure time response shown in Fig. 10.

Figure 12 shows the cavitation bubble growth behaviors, which clearly depend on the void fraction. The bubbles grow up to the maximum radius at a few μs after the peak negative pressure, i.e. the time delay is recognized. The size is not associated to the magnitude the negative pressure and the period seems a more critical factor to decide the cavitation bubble size. The time delay between the negative pressure response and the cavitation bubble growth is dependent on the initial bubble size and a pressure-changing rate. Figure 13 shows the relationship between the maximum radius of cavitation bubbles and the void fractions. The cavitation bubble size decreases gradually in the range more than 10^{-5} , and in the case more than 10^{-3} it is hardly dependent on the void fraction. Figure 14 shows the relationship between cavitation intensity ($\sim R^3$), injected microbubble size and void fraction. It is expectable that the intensity is reduced sufficiently by the injected microbubbles even at the void fraction of 10^{-5} .

Figure 15 shows the damage surface given in the MIMTM damage tests under mercury flowing condition without and with microbubbles [13]. At the same time, the pressure responses were measured. It was confirmed that the damage was tremendously reduced by the microbubbles injected into the flowing mercury, and the peak value of compressive pressure was hardly varied by the microbubbles, on the other hand the negative pressure response was slightly changed. The measured time response of the pressure waves was used in Rayleigh-Plesset Eq.(4) to calculate the cavitation bubble growth. It was confirmed that the small change of negative pressure gives a great effect on the cavitation growth to reduce damage [13].

5. LIFETIME ESTIMATION OF MERCURY TARGET

The lifetime in the target design was estimated from the viewpoint of radiation damage, i.e. the accumulated dose to lose the ductility in the structural materials of the target. After finding it, however, the cavitation damage gets to be a crucial factor to decide the lifetime rather than the radiation damage.

Let's consider how we can estimate the lifetime of target in which the pressure waves is imposed repeatedly to induce the cavitation, see Fig. 16. The pressure wave propagation is predicted by the numerical simulation taking account of the proton beam profile. The Rayleigh-Plesset equation is applicable to predict the cavitation bubble growth behavior. The cavitation erosion is divided into two states: incubation and steady states, in which the erosions are predictable respectively by using Eqs. (3) and (5), as shown in Fig17. The onset of the steady state, i.e. the end of incubation state, is dependent on the cavitation intensity associated with the

negative pressure period, which is a significant factor of cavitation bubble inception and growth. As shown in Fig.7, the cavitation intensity is related to R^3 . R is estimated by the Rayleigh-Plesset equation using the time response of the mercury in the target vessel.

The lifetime is decided by the leakage of mercury leak or fatigue failure at the beam window due to cavitation erosion. In fact, the mercury target had already been replaced in 2010 in the SNS. Many pits due to cavitation erosion were found in the inner wall in the vessel and perfectly penetrated pits at the beam window were found [24]. As following to Fig.16, we could estimate the lifetime up to the pit penetration and obtain a suitable prediction.

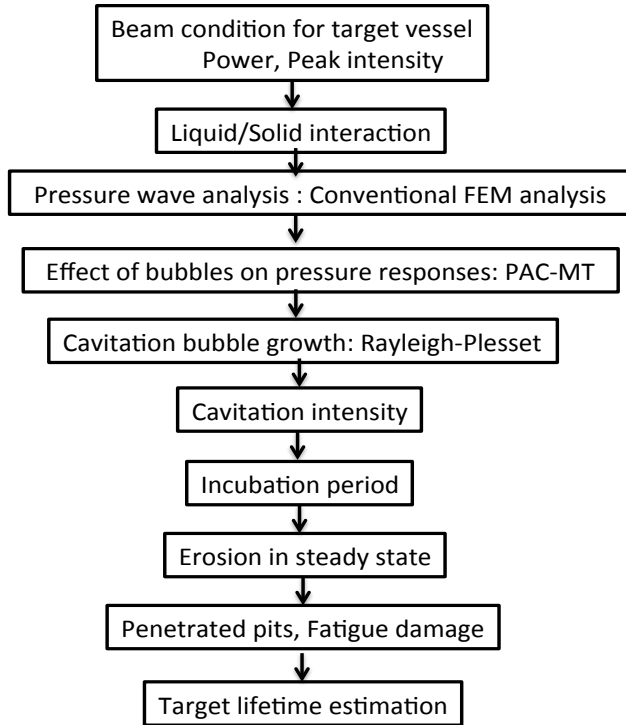


Figure 16 Flow of target lifetime estimation

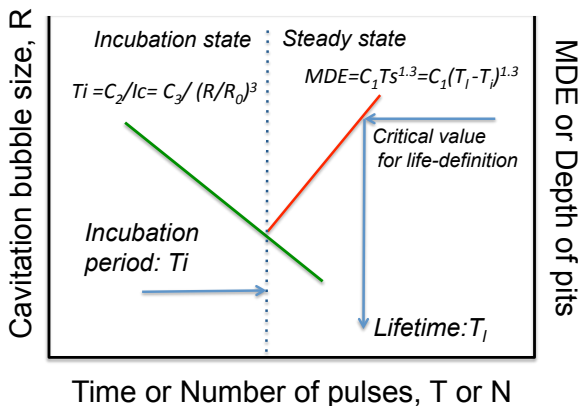


Figure 17 Prediction of cavitation erosion consisting of incubation and steady states

6. SUMMARY

Mercury cavitation gets to be a crucial issue to increase the power up to MW-class in the mercury target for pulsed spallation neutron sources. The cavitation is caused by the negative pressure that is induced by the pressure waves propagating through mercury to the interface between mercury liquid and solid wall. R&D was carried out to mitigate the cavitation damage by two ways: i.e. hardening solid wall surface and softening mercury. As for the hardening, PCN (plasma carburizing and nitriding) was developed. Microbubbles is expected to soften mercury to reduce the pressure waves.

The prediction of cavitation damage was carried out based on experimental data obtained in the MIMTM mercury cavitation test, numerical simulation to estimate the pressure wave propagation in the mercury vessel, and the bubble growth analysis using Rayleigh-Plesset equation. The microbubbles are expected to be useful for mitigating the cavitation intensity and damage.

ACKNOWLEDGMENTS

This work was partly supported by the Japan Society for the Promotion of Science through a Grant-in-Aid for Scientific Research (No. 20360090 and No. 23360088)

REFERENCES

REFERENCES

- [1] <http://j-parc.jp/MatLife/en/>
- [2] <http://sns.gov/facilities/SNS/>
- [3] Skala, K. and Bauer, G. S., ICANS XIII, 559-576 (1995).
- [4] Futakawa, M., Kikuchi, K., Conrad, H., and Stechemesser H., Pressure and stress waves in a spallation neutron source mercury target generated by high-power proton pulses, Nucl. Instrum. Methods Phys. Res., Sect. A, 439, 1-7 (2000).
- [5] Futakawa, M., Kogawa, H. and Hino, R., Measurement of dynamic response of liquid metal subjected to uniaxial strain wave, J. Phys. IV France 10, Pr9-237-242 (2000).
- [6] Futakawa, M., Kogawa, H., Hino, R., Date, H. and Takeishi, H., Erosion damage on solid boundaries in contact with liquid metals by impulsive pressure injection, Int J. Imp. Eng. 28, 123-135 (2003).
- [7] Haines, J. R., Farrell, K., Hunn, J. D., Lousteau, D. C., Mansur, L. K., McManamy, T. J., Pawel, S. J., and Riemer, B. W., Summary of Mercury Target Pitting Issue, SNS-101060100-TR0004(2002).
- [8] Futakawa, M., Naoe, T., Kogawa, H., Tsai C., and Ikeda, Y., Pitting damage formation up to over 10 million cycles - off-line test by MIMTM-, J. Nucl. Sci. Technol., 40, 895-904 (2003).
- [9] Mansur, L.K., Materials research and development for the spallation neutron source mercury target, Jour. Nucl. Mater. 318, 14-25 (2003).
- [10] Naoe, T., Futakawa, M., Shoubu, T., Wakui, T., Kogawa, H., Takeuchi, H. and Kawai, M., Mitigation technologies for damage induced by pressure waves in high-power

- mercury spallation neutron sources (I) -Material surface improvement-, J. Nucl. Sci. Technol., 45, 698-703 (2008).
- [11] Soltner, H., Gas bubble admixture for pressure pulse mitigation in high-power liquid-mercury spallation targets, ISSN 1433-559X, ESS03-152-T (2003).
 - [12] Okita, K., Matsumoto, Y. and Takagi, S., Propagation of pressure waves, caused by a thermal shock, in liquid metals containing gas bubbles, Proc. FEDSM2005-77397 (2005).
 - [13] Futakawa, M., Kogawa, H., Hasegawa, S., Naoe, T., Ida, M., Haga, K., Wakui, T., Tanaka, N., Matsumoto, Y., and Ikeda, Y., Mitigation technologies for damage induced by pressure waves in high-power mercury spallation neutron sources (II) –Bubbling effect to reduce pressure waves, J. Nucl. Sci. Technol., 45, 1041-1048 (2008).
 - [14] Futakawa, M., Kogawa, H., Hasegawa, S., Ikeda, Y., Riemer, B., Wendel, M., Hains, J., Bauer, G., Naoe, T., Okita, K., Fujiwara, A., Matsumoto, Y. and Tanaka, N., Cavitation damage prediction for spallation target vessels by assessment of acoustic vibration, J. Nucl. Mater., 377, 182-188 (2008).
 - [15] Ni, L., Bauer G.S., Spitzer H., Effect of pulsed power input into a liquid metal target, Nucl. Instrum. Methods Phys. Res., Sect. A, 425, 57-64 (1999).
 - [16] Kogawa, H., Ishikura, S., Sato, H., Harada, M., Takatama, S., Futakawa, M., Haga, K., Hino, R., Meigo, S., Maekawa, F., Ikeda, Y., Effect of proton beam profile on stress in JSNS target vessel, J. Nucl. Mater., 343, 178-183 (2005).
 - [17] Kogawa, H., Hasegawa, S., Futakawa, M., Riemer, B., Wendel, M., Haines, J., Numerical study on pressure wave propagation in mercury loop, J. Nucl. Mater., 377, 195-200 (2008).
 - [18] Futakawa, M., Naoe, T., Tsai, C.C., Kogawa, H., Ishikura, S., Ikeda, Y., Soyama, H. and Date, H., Pitting damage by pressure waves in a mercury target, Jour. Nucl. Mater., 343, 70-80 (2005).
 - [19] Soyama, H. and Futakawa, M., Estimation of incubation time of cavitation erosion for various cavitating conditions, Tribology letters, 17, 27-30 (2004).
 - [20] e.g. Brennen, C.E., Cavitation and bubble dynamics, Oxford Univ. Press. 1995.
 - [21] Futakawa, M., Naoe, T., Kogawa, H., Date, H., Ikeda, Y., Micro-impact damage caused by mercury bubble collapse, JSME Int. J. A, 48, 234-239 (2005).
 - [22] Okita, K., Fujiwara, A., Takagi, S., Matsumoto, Y., Futakawa, M., CAV2006, Wageningen, The Netherlands, September 2006.
 - [23] Kogawa, H., Haga, K., Naoe, T., Kinoshita, H., Ida M. and Futakawa, M., Development of bubble injection technique in JSNS mercury target, ICANS-XIX(2010), March, Grindelwald, Switzerland.
 - [24] Mcclintock, D., Riemer, B., Ferguson, P., Characterization of mechanical properties and cavitation-induced erosion of the first operational Spallation Neutron Source target module, 10th IWSMT, Oct. Beijing, China, 2010.